TURBULENT MIXING IN A TIDAL CHANNEL

by

©Daiyan Huang

B.Sc., M.Sc., Ocean University of Qingdao, 1986, 1989

A Thesis Submitted in Partial Fulfillment of the

Requirements for the Degree of

MASTER OF SCIENCE

in the

SCHOOL OF EARTH AND OCEAN SCIENCES

We accept this thesis as conforming

to the required standard

[redacted]

Dr. R. Lueck, Supervisor (School of Earth and Ocean Sciences)

[redacted]

Dr. C. Garrett, Departmental Member (School of Earth and Ocean Sciences)

[redacted]

Dr. W. Crawford, Departmental Member (Institute of Ocean Sciences)

[redacted]

Dr. N. Djilali, External Examiner (Mechanical Engineering)

Abstract

During a joint collaborative experiment between September 19 and 30, 1994, a novel microstructure instrument (TAMI), which was attached to the channel bottom on a mooring line and measured changes in horizontal flows, successfully measured microstructure, fine-structure and current at 15 m above the bottom in Cordova Channel. The channel is a minor passage connecting the Pacific Ocean and the Strait of Georgia. The other main instruments involved in the experiment were an acoustic Doppler current profiler (ADCP), an acoustic scintillation system, CTD profiler and a meteorology station.

The flow of the channel was mainly tidal. The tidal components explained slightly more than 91% of the variance of the measured current, and the residual current which represented 2-D horizontal eddies and accounted for about 10% of tidal variance. The water became warmer and fresher during the experiment. With TAMI, the salinity record showed modulation by the tide while the temperature record did not exhibit a clear tidal signal. The water was fairly well mixed during strong ebbing, more stratified during the floods and became unstable occasionally near the turning of the tide. The effect of wind stress at 15 m depth was much weaker than that from the local bottom stress.

The spectra of the velocity and temperature fluctuations, in water, all had a -5/3 slope in the inertial-subrange regardless of the level of stratification in the channel. Thus, the finding that the slope of velocity and temperature spectra are affected by stratification in Gargett *et al.* (1984) and Gargett (1985) is not universal and may be more due to the physics of decaying turbulence than to stratification itself. The two universal functions (F_{22} and F_{33}) were statistically identical in the inertial-subrange and even no evident influence of stratification on vertical spectrum.

The turbulence at 15m above the bottom of the channel was very intense and the dissipation ranged from 10^{-8} to 10^{-4} W kg^{-1}. The pattern of dissipation and tidal current repeated every lunar day. The dissipation was not proportional to U^3 or U^3_{max} – the maximum speed of each ebb/flood. Thus, the turbulence was not generated by the local bottom stress but may have been produced by the eddies which were likely shed from Cordova Spit and the north end of James Island.

The averaged dissipation obtained with TAMI was equal to the estimate obtained with the acoustic scintillation system within a factor of less than 1.6. The production of turbulent kinetic energy (TKE) obtained with the ADCP was balanced within a factor of 2 by dissipation. The decay time for the eddy KE was estimated to be a little longer than one hour. Three different methods of comparing the mean tidal KE against the time integrated dissipation indicated that 53, 77 and 84% of tidal KE was dissipated locally.

Eddy diffusivity of density scaled with $A_v = \kappa z\sqrt{C_D}U$, a formula for A_v in a logarithmic boundary layer, is close to unity even though most of the observations were taken above the logarithmic layer. The scaled eddy diffusivity of density decreased with increasing Richardson number approximately as $\propto Ri^{-0.7}$. For $Ri < 1/4$, most of the scaled eddy diffusity have values of order 1. The eddy diffusivity for density did not have a clear tidal signal.

The temperature spectral level ($\zeta = B\chi$, where χ was the rate of dissipation of temperature fluctuation variance and B is a "universal" constant) was related to the mean temperature gradient by $|\frac{\partial T}{\partial z}|/20 \leq 3 \times 10^{-4}\zeta \leq 20|\frac{\partial T}{\partial z}|$. Eighty-one percent of estimates of the eddy diffusivities for heat (K_T) and for density were within a one decade range of equality over a 3.5 decade span in value. K_T and A_v (the eddy viscosity) were equal with seventy-four percent of the data within one decade of equality. This thesis provides some guidance and constraints for the modelling of mixing in coastal tidal channels.

Examiners:

[redacted]

Dr. R. Lueck, Supervisor (School of Earth and Ocean Sciences)

[redacted]

Dr. C. Garrett, Departmental Member (School of Earth and Ocean Sciences)

[redacted]

Dr. W. Crawford, Departmental Member (Institute of Ocean Sciences)

[redacted]

Dr. N. Djilali, External Examiner (Mechanical Engineering)

Table of Contents

List of Tables

List of Figures

Acknowledgments

First of all, I would like to thank my supervisor, Dr. Rolf G. Lueck. Without his advice and support it would have been impossible to complete this thesis. I am grateful for the many hours he has spent with me discussing the data and their analysis. His patience is appreciated. In addition, I would like to thank all of the other committee members – Drs. Bill Crawford, Neil Djilali and Chris Garrett for their support.

From the Turbulence Lab, I would like to thank my colleagues – Mr. Don Newman for looking after the electronics of TAMI, Mr. John Box for his work on mechanical aspect and Mr. Youyu Lu for his work on the vertical shear and the production of TKE obtained with the ADCP, and many discussions with me on our observations. Youyu and I spent ten days in a trailer on Cordova Spit monitoring the the ADCP.

Thanks must also be given to my friends, Dr. Frank Peters and Mrs Alice Peters. They spent a lot of time in proof-reading the draft version of this thesis. They are two of the kindest Canadians I have ever met. They have also spent a lot of time in helping many people who are newcomer to Canada.

From the Chinese community in Victoria, I would also like to thank many Chinese fellow students in the University of Victoria, particularly in our department, for their help.

I will never forget the support from my father and mother given selflessly and unconditionally. The help from the other relatives, particularly my father-in-law, uncle and brothers, are appreciated.

Finally, I would like to thank my wife for her love and support during these years. Without her, I would have never finished this thesis.

Chapter 1

Introduction

Conditions in the coastal ocean differ significantly from those in the open ocean. Most notably, water depths are shallower and currents are stronger in the coastal environment compared to the open ocean. Turbulence is usually quite intense in the coastal environment because of bottom friction on the tidal circulation. The mixing induced by friction further intensifies the "fjord" circulation which is driven by buoyancy input from rivers (Pond and Pickard 1990). This mixing driven by the tidal circulation promotes biological productivity by diffusing nutrient-rich deep water towards the near-surface euphotic zone. Turbulence also induces friction throughout the water column which, in turn, determines the strength of the circulation. The effective or "eddy viscosity" of turbulence is a key parameter required for the modelling of coastal circulation. The most intense turbulence and mixing occurs in tidal channels where the contractions of depth and width accelerate the flow.

Cordova Channel is a tidal channel along the coast of British Columbia, which forms a minor side passage connecting the Strait of Georgia with the Pacific Ocean. The channel has a strong tidal current of order 1 ms^{-1} and is relatively shallow ($\sim$30 m depth).

This thesis presents the results of observations of turbulence in Cordova Channel. A collaborative experiment was conducted in Cordova Channel during September 16 - 30, 1994 and involved the measurements of physical and biological parameters. The two main purposes of the experiment were (1) to describe the characteristics and temporal evolution of turbulent mixing in a tidal channel and (2) to use a variety

of new techniques for the measurements of turbulence. These new techniques include using Tethered Automonous Microstructure Instrument (TAMI) and an Acoustic Doppler Current Profiler (ADCP) which measures velocity and Reynolds stress, of Lueck's group, and an acoustic scintillation system, operated by Dr. Farmer's group at the Institute of Ocean Sciences (IOS), which measures the cross-channel average of along-channel flow and turbulence. The other instruments that were deployed are, (1) a neutrally-buoyant, high-drag float, used by Dr. D'Asaro at the Applied Physics Lab (APL) of the University of Washington for Lagrangian measurement, and (2) an acoustic daylight receiver array, used by Dr. Deane at the Marine Physics Lab (MPL) of the Scripps Institute of Oceanography for measuring the parameters of acoustic fluctuation induced by waves traveling through turbulence, (3) two tide gauges operated by Canadian Hydrographic Service, (4) a CTD profiler used by IOS for the measurement of temperature, salinity and density, and (5) meteorological instruments used by IOS for the measurements of wind velocity, air temperature and barometric pressure.

Chapter 2 describes the basic theories used in my studies. Chapter 3 gives a brief description of TAMI - a moored instrument that carries a number of sensors including (1) four shear probes and two fast thermistors for measuring the turbulent fluctuations of horizontal velocity and temperature, (2) three accelerometers for detecting the motion of the instrument, (3) three pairs of Sea-Bird thermometers and conductivity cells for the measurements of temperature, salinity, density and their vertical gradients, (4) two rotors and one compass for measuring the current, and (5) a pressure gauge for measuring the depth of the instrument.

Chapter 4 provides a description of the observations and calculations of non-turbulent parameters including the mean flow, temperature, salinity, density, the Brunt-Väisälä frequency and the Richardson number. The measured current is separated into a purely tidal current and a residual current which is considered to be the

eddy velocity. CTD records from both TAMI and CTD profiles are used to examine the stratification of the water. Events of shear instability, using the data reported from TAMI and the ADCP, are examined .

In chapter 5, some typical time series of shear and acceleration are examined to show that the turbulence data were free from the contamination by body motion at scales from $O(0.1\text{m})$ to $O(10\text{m})$.

Chapter 6 investigates the existence of the inertial-subrange in both velocity and temperature spectra, and the local isotropy of velocity spectra and the effect of stratification on these spectra. The slopes of averaged spectra of velocity and temperature in the inertial-subrange are calculated and the range of the inertial-subrange are examined.

Chapter 7 describes the tidal evolution of the turbulence at 15m above the bottom. The relationship between the dissipation and tidal current is investigated to examine if the turbulence was generated by local bottom stress. The relationship between dissipation and 2-D horizontal eddy KE is examined.

In Chapter 8, the dissipation estimated with TAMI is compared against that obtained with the acoustic scintillation system, and then against the the production of TKE estimated with the data taken by the ADCP to examine the local balance of TKE. The decay time scale for the eddies is estimated. Three different methods of comparing the mean tidal KE against the time integrated dissipation are used to estimate the percentage of the mean tidal KE dissipated locally during a quarter of a lunar day. The relationship between the eddy diffusivity and the Richardson number is examined. The temperature spectral level is estimated and the relationship between the temperature spectral level and the mean vertical temperature gradient is examined. Finally, the eddy diffusivity for heat (K_T) is estimated. The relationship between K_T and K_v (the eddy diffusivity for density) as well as the eddy viscosity (A_v) is examined.

Details of data processing are discussed in Appendixes. Appendix A includes (1) the correction of the current speed record observed with TAMI for bearing friction due to gelatinous material in the water, and (2) the correction of salinity for the accurate calculation of the buoyancy frequency squared. Appendix B includes (1) the wavenumber correction of the measured spectra after Ninnis (1984), and (2) the interpolation of calibration data to obtain the sensitivity of the shear probes at 11.5°C which is needed for the calculation of the rate of dissipation of TKE. Appendix C provides the description of the inertial-subrange technique used to estimate the rate of dissipation of a velocity spectrum.

Chapter 2

Theory

2.1 Turbulence dynamics

Turbulence is commonly found in most fluid flows in nature and engineering applications. When the Reynolds number of a laminar flow becomes large, the flow becomes unstable and turbulent. The Navier-Stokes equation that describes the flow of an incompressible fluid in a non-rotating system is

$$\frac{\partial \widetilde{u}_i}{\partial t} + \widetilde{u}_j \frac{\partial \widetilde{u}_i}{\partial x_j} + \frac{1}{\rho}\frac{\partial \pi}{\partial x_i} = g_i + \frac{\partial}{\partial x_j}\left(\nu \frac{\partial \widetilde{u}_i}{\partial x_j}\right) \tag{2.1}$$

where $x_j = (x_1, x_2, x_3) = (x, y, z)$, ρ is density, $\widetilde{u}_i$ is velocity, π is pressure, $g_i = (0, 0, -g)$ is gravity, and ν is viscosity. According to the Reynolds decomposition, the variables in the Navier-Stokes equation can be decomposed into mean and fluctuating (turbulent) parts

$$\widetilde{u}_i = U_i + u_i, \pi = \Pi + \pi', \rho = \rho_o + \rho' \tag{2.2}$$

where $\overline{u_i} = 0$, $\overline{\pi'} = 0$ and $\overline{\rho'} = 0$, and the overbar denotes an ensemble average. For an incompressible fluid, substituting (2.2) into (2.1) and taking an ensemble average produces an equation for the mean flow momentum (the Reynolds equation)

$$\frac{\partial U_i}{\partial t} + U_j \frac{\partial U_i}{\partial x_j} = g_i - \frac{1}{\rho_o}\frac{\partial \Pi}{\partial x_i} + \frac{\partial}{\partial x_j}\left(\nu \frac{\partial U_i}{\partial x_j} - \overline{u_i u_j}\right) \tag{2.3}$$

and an equation for an ensemble average of the fluctuating momentum

$$\frac{\partial u_i}{\partial t} + U_j \frac{\partial u_i}{\partial x_j} + u_j \frac{\partial U_i}{\partial x_j} - \frac{\partial \overline{u_i u_j}}{\partial x_j} + u_j \frac{\partial u_i}{\partial x_j} + \frac{1}{\rho_o}\frac{\partial \pi'}{\partial x_i} - \frac{\rho'}{\rho_o} g_i = \nu \nabla^2 u_i. \tag{2.4}$$

For details see Tennekes and Lumley (1972), Hinze (1975), Monin and Yaglom (1971, 1975) .

By multiplying (2.4) with $u_i/2$ and averaging, the equation for the conservation of turbulent kinetic energy is obtained,

$$\frac{\partial q}{\partial t}+U_j\frac{\partial q}{\partial x_j} = -\Big[\frac{1}{\rho_o}\frac{\partial \overline{u_i\pi'}}{\partial x_i}+\frac{\partial}{\partial x_j}\Big(\frac{1}{2}\overline{u_i^2u_j}-2\nu\overline{u_ie_{ij}}\Big)\Big]-\overline{u_iu_j}\frac{\partial U_i}{\partial x_j}-\frac{g}{\rho_o}\overline{\rho' w}-2\nu\overline{e_{ij}e_{ij}}, \quad (2.5)$$

where $q = \overline{u_i^2}/2$ is the turbulent kinetic energy (TKE) density and e_{ij} is the rate of strain

$$e_{ij} = \frac{1}{2}\Big(\frac{\partial u_i}{\partial x_j}+\frac{\partial u_j}{\partial x_i}\Big). \quad (2.6)$$

The rate of dissipation of TKE is $\epsilon = 2\nu\overline{e_{ij}e_{ij}}$.

In a statistical steady state, the first term on the left hand side of (2.5) vanishes. For stationary and homogeneous turbulence, under the assumption of a local balance of TKE (Osborn 1980), the second term on the left hand side and the first term of the right hand side of (2.5), which represent the redistribution of energy, can be neglected. Thus, only three terms are left, namely, a production term, $P = -\overline{u_iu_j}\frac{\partial U_i}{\partial x_j}$, a buoyancy flux term, $B = \frac{g}{\rho_o}\overline{\rho' w}$, and a dissipation term, ϵ. Thus, a local balance of TKE as discussed by Osborn (1980) is

$$P = \epsilon + B. \quad (2.7)$$

There are a number of instruments for measuring ϵ but it is very difficult to measure P and B. The term of B is usually parametrized with P to form a flux Richardson number, $R_f = B/P$ (Osborn 1980). Hence equation (2.7) can be written as

$$P = R_fP + \epsilon. \quad (2.8)$$

The value of R_f must be less than 1 for a steady state (Osborn 1980) and there are many good arguments (Stewart 1959) that its value is considerably less than 1 for stationary turbulence in a shear flow. Therefore, B can be expressed in the terms of ϵ, R_f, and a mixing efficiency, Γ, as

$$B = \frac{R_f}{1-R_f}\epsilon = \Gamma\epsilon. \quad (2.9)$$

Using a vertical eddy diffusivity for density, K_v, the buoyancy flux can be parameterized as

$$-\overline{\rho' w} = K_v \frac{\partial \rho_o}{\partial z}, \tag{2.10}$$

where $\frac{\partial \rho_o}{\partial z}$ is the vertical gradient of mean density. From the definition of the Brunt-Väisälä (or buoyancy) frequency is given by,

$$N^2 = -\frac{g}{\rho_o}\frac{\partial \rho_o}{\partial z}, \tag{2.11}$$

the eddy diffusivity for density, K_v, can be expressed as

$$K_v \leq \frac{\Gamma \epsilon}{N^2}, \tag{2.12}$$

where Γ is equal to 0.2 according to Osborn (1980) and this value is mostly used for oceanic measurements. However, Γ varies in a range of 0.04 - 0.4 estimated from oceanic measurements, laboratory experiments and numerical simulations as summarized by Peters (1995).

From equation (2.6), the rate of dissipation can be estimated, using $\epsilon = 2\nu\overline{e_{ij}e_{ij}}$. Equation (2.6) is expanded as

$$\epsilon = \nu \overline{\frac{\partial u_i}{\partial x_j}\left(\frac{\partial u_i}{\partial x_j} + \frac{\partial u_j}{\partial x_i}\right)}. \tag{2.13}$$

[For details see Hinze 1975, Monin and Yaglom 1975.] In isotropic turbulence, one has

$$\overline{\left(\frac{\partial u_1}{\partial x_1}\right)^2} = \overline{\left(\frac{\partial u_2}{\partial x_2}\right)^2} = \overline{\left(\frac{\partial u_3}{\partial x_3}\right)^2}, \tag{2.14}$$

$$\overline{\left(\frac{\partial u_1}{\partial x_2}\right)^2} = \overline{\left(\frac{\partial u_1}{\partial x_3}\right)^2} = \overline{\left(\frac{\partial u_2}{\partial x_1}\right)^2} = ..., \tag{2.15}$$

$$\overline{\frac{\partial u_1}{\partial x_2}\frac{\partial u_2}{\partial x_1}} = \overline{\frac{\partial u_1}{\partial x_3}\frac{\partial u_3}{\partial x_1}} = \overline{\frac{\partial u_2}{\partial x_3}\frac{\partial u_3}{\partial x_2}}, \tag{2.16}$$

and

$$2\overline{\left(\frac{\partial u_1}{\partial x_1}\right)^2} = \overline{\left(\frac{\partial u_2}{\partial x_1}\right)^2} = \overline{\frac{\partial u_1}{\partial x_3}\frac{\partial u_3}{\partial x_1}}.$$

Thus, the rate of dissipation of TKE, using any shear term, is

$$\epsilon = \frac{15}{2}\nu\overline{(\frac{\partial u_2}{\partial x_1})^2}. \tag{2.17}$$

A cross-stream turbulent velocity shear is usually measured in the ocean with a shear probe (Osborn and Crawford 1980; Gregg 1987). [Here "cross-stream" denotes a direction perpendicular to the direction of travel of the sensor. The direction in which the sensor travels is the stream-wise direction but this direction is not necessarily the direction of the ambient mean flow.] For example, $\frac{\partial u_{1,2}}{\partial x_3}$ is measured with a vertical free fall vehicle (Lueck *et al.* 1983; Gregg and Sanford 1988; Dewey *et al.* 1987), and $\frac{\partial u_{2,3}}{\partial x_1}$ with an instrument travelling in horizontal (Osborn and Lueck 1985a, 1985b; Lueck 1987) which is the same for TAMI (Lueck *et al.* 1996).

2.2 Turbulence kinematics

The correlation function and the spectrum of turbulent velocity fluctuation are commonly used to describe turbulence. The energy spectrum is defined as the Fourier transform of the autocorrelation, $R_{ij} = \overline{u_i(\mathbf{x},t)u_j(\mathbf{x}+\mathbf{r},t)}$, where $\mathbf{x}$ denotes the position, t is the time and $\mathbf{r}$ is the vector connecting the points i and j. The integration of the three-dimensional kinetic energy spectrum density, $E(k)$, in the wavenumber domain, is equal to the turbulent kinetic energy,

$$\int_0^\infty E(k)dk = \frac{1}{2}(\overline{u_1^2} + \overline{u_2^2} + \overline{u_3^2}), \tag{2.18}$$

where u_1, u_2, u_3 are the velocity fluctuation components and k is the wavenumber magnitude. Turbulent velocity is usually measured in the time domain which provides only a frequency spectrum density. If the speed, U, of a sensor is rapid enough, so that one can assume that the turbulent field is "frozen", the time domain (frequency domain) can be converted into the space domain (wavenumber domain) using the Taylor hypothesis (Tennekes and Lumley 1972; Kundu 1990). For example, $x = t \times U$, $k = f/U$ and $E(k) = E(f) \times U$.

In general, three velocity fluctuation components can be measured in the laboratory (Itsweire *et al.* 1986) and in atmospheric experiments (Fairall *et al.* 1990). However, it is quite difficult to measure the stream-wise velocity component in oceanic experiments, so two cross-stream velocity components are usually measured using a pair of shear probes (airfoils) (Osborn and Crawford 1980; Gregg 1987). Like the three-dimensional energy spectrum of (2.18), the one-dimensional energy spectra, $\phi_{11}(k_1)$, $\phi_{22}(k_1)$ and $\phi_{33}(k_1)$ are related to velocity components as

$$\int_0^\infty \phi_{11}(k_1)dk_1 = \overline{u_1^2}, \tag{2.19}$$

$$\int_0^\infty \phi_{22}(k_1)dk_1 = \overline{u_2^2}, \tag{2.20}$$

$$\int_0^\infty \phi_{33}(k_1)dk_1 = \overline{u_3^2}. \tag{2.21}$$

In isotropic turbulence, one has $\overline{u_1^2} = \overline{u_2^2} = \overline{u_3^2}$. The relationship between the one-dimensional energy spectra and the three-dimensional energy spectrum (Hinze 1975; Monin and Yaglom, 1975) is given by

$$E(k_1) = -k_1 \frac{\partial}{\partial k_1}\Big\{\frac{1}{2}\phi_{11}(k_1) + \phi_{jj}(k_1)\Big\}, \tag{2.22}$$

where $j = 2, 3$ and no summation is implied. The relationship between ϕ_{11} and ϕ_{jj} is

$$\phi_{jj}(k_1) = \frac{1}{2}\Big\{\phi_{11}(k_1) - k_1 \frac{\partial \phi_{11}(k_1)}{\partial k_1}\Big\}. \tag{2.23}$$

Simplifying the energy spectrum equation, one obtains

$$E(k_1) = \frac{k_1^2}{2}\frac{\partial^2 \phi_{11}(k_1)}{\partial k_1^2} - \frac{k_1}{2}\frac{\partial \phi_{11}(k_1)}{\partial k_1}. \tag{2.24}$$

The rate of the dissipation of turbulent kinetics energy, ϵ, can be estimated by

$$\epsilon = 2\nu \int_0^\infty E(k_1)dk_1 = 15\nu \int_0^\infty k_1^2 \phi_{11}(k_1)dk_1 = \frac{15}{2}\nu \int_0^\infty k_1^2 \phi_{jj}(k_1)dk_1. \tag{2.25}$$

Turbulent energy is cascaded from large-scale eddies which contain most of the energy down to small eddies where it is dissipated. According to Kolmogoroff's first

hypothesis of local isotropy (Kolmogoroff 1941), the turbulent kinetic energy spectrum is independent of the large-scale eddies where the energy resides when the Reynolds number is sufficiently large. However, the spectrum depends on molecular viscosity, ν, wavenumber, k, and dissipation rate, ϵ. Further in steady and stationary turbulence, the rate of transfer of energy from the energy-containing scales to the small scale must be equal to the energy dissipation rate at the dissipative scales. Using dimensional analysis, the energy spectrum is obtained as

$$E(k) = (\epsilon\nu^5)^{1/4} F(k/k_s), \tag{2.26}$$

where k_s is the Kolmogoroff wavenumber,

$$k_s = (\frac{\epsilon}{\nu^3})^{1/4} \tag{2.27}$$

and $F(k/k_s)$ is a universal function. Hence, the one-dimensional spectra become

$$\phi_{11}(k_1) = (\epsilon\nu^5)^{1/4} F_{11}(k_1/k_s), \tag{2.28}$$

$$\phi_{jj}(k_1) = (\epsilon\nu^5)^{1/4} F_{jj}(k_1/k_s), \tag{2.29}$$

where $F_{11}(k/k_s)$ and $F_{jj}(k/k_s)$ are universal functions, and local isotropy gives

$$F_{22}(k/k_s) = F_{33}(k/k_s) \tag{2.30}$$

According to Kolmogoroff's second hypothesis, with a very large Reynolds number, there exists a range between the energy-containing scales and the dissipative scales in which molecular viscosity ν is unimportant. This range is called the inertial subrange. The energy spectrum in the inertial-subrange can be simplified to

$$E(k) = A\epsilon^{2/3} k^{-5/3}, \tag{2.31}$$

where $A = 1.5$ is a universal constant for the three-dimensional spectrum. From equations (2.28) and (2.29) with the relationship of $F_{jj} = \frac{3}{4} F_{11}$, one can obtain the one-dimensional spectra as

$$\phi_{11}(k) = K\epsilon^{2/3} k^{-5/3}, \tag{2.32}$$

$$\phi_{jj}(k) = \frac{4}{3} K \epsilon^{2/3} k^{-5/3}, \tag{2.33}$$

where $K = 0.50$ is Kolmogoroff constant for the one-dimensional spectrum (Monin and Yaglom 1975; Grant *et al.* 1962; Edson *et al.* 1990).

2.3 Temperature fluctuation spectrum

For a scalar, for example, temperature, the variance of its fluctuation θ' is defined as

$$\overline{\theta'^2} = \int_0^\infty \Psi(k')dk' = \int_0^\infty \psi(k)dk, \tag{2.34}$$

where $\Psi(k')$ is the three-dimensional temperature fluctuation spectrum and $\psi(k)$ is the one-dimensional spectrum. In isotropic turbulence, the three-dimensional spectrum is related to the one-dimensional spectrum by

$$\Psi(k) = -k \frac{\partial \psi(k)}{\partial k}. \tag{2.35}$$

The rate of dissipation of temperature variance, χ, is obtained as

$$\chi = 6\kappa_T \int_0^\infty k^2 \psi(k)dk, \tag{2.36}$$

where κ_T is the thermal diffusivity. Within the inertial subrange of the velocity spectrum, there exists an inertial subrange for the temperature spectrum for $k \ll k_s$, called the inertial-convection subrange. The one-dimensional temperature spectrum in the inertial-convection subrange is

$$\psi(k) = B\epsilon^{-\frac{1}{3}} \chi k^{-\frac{5}{3}}, \tag{2.37}$$

where $B = 0.5$ is another universal constant (Obouku 1949; Corrsin 1959) estimated from many experiments (Gargett 1985). However, the constant B is quite scattered, ranging from 0.35 (Gibson and Schwaz 1963) to 1.15 (Gibson, Stegen and Williams 1970) as summarized by Gargett (1985).

Using the buoyancy Reynolds number, R_B, Gargett (1985) classified her temperature spectra measured in Knight Inlet, B.C. into two classes, A and B. The buoyancy

Reynolds number (Dillon and Caldwell 1980) is defined as $R_B = \left(\frac{\epsilon}{\nu N^2}\right)^{4/3}$ and a term, I, is used

$$I = R_B^{3/4} = \frac{k_s}{k_b}, \tag{2.38}$$

where $k_b = (N^3/\epsilon)^{\frac{1}{2}}$ is a buoyancy-wavenumber. Those temperature spectra in class A ($I \sim 3000$), taken in an isotropic velocity field, had, however, a -2/3 rather than a -5/3 slope in the inertial-convection subrange. Those temperature spectra in class B ($I \sim 50$ - 100), taken in an anisotropic velocity field did have a -5/3 slope in the inertial-convection subrange.

The influence of intermittency on both ϵ and χ in the inertial-subrange of the scalar spectrum for the condition of Prandtl number, $Pr \gg 1$, has been investigated by Van Atta (1971, 1973). He assumes that ϵ and χ are in lognormal distributions with equal variances, then the slope of the scalar spectrum in the inertial-subrange is depend on the parameters of μ – a constant – and the correlation coefficient, $\rho(r)$, between ϵ and χ, as

$$m = -\frac{5}{3} + \frac{1}{3}\mu\left(\frac{2}{3} - \rho(r)\right) \tag{2.39}$$

where μ can be assumed to be 0.5 according to Gargett (1985).

Assuming that turbulence drives overturns against a well-defined mean local temperature gradient, and that the turbulence is steady, stationary and homogeneous as discussed in Osborn and Cox (1972), then one can simplify the temperature variance equation from

$$\frac{\partial\overline{\theta'^2}}{\partial t} + \frac{\partial}{\partial x_j}\left(U_j\overline{\theta'^2} + \overline{u_j\theta'^2} - \kappa_T\frac{\partial\overline{\theta'^2}}{\partial x_j}\right) + 2\overline{u_j\theta'}\frac{\partial T}{\partial x_j} = -2\kappa_T\overline{(\nabla\theta')^2} \tag{2.40}$$

to

$$-\overline{w\theta'}\frac{\partial T}{\partial z} = \kappa_T\overline{(\nabla\theta')^2} = 2\chi \tag{2.41}$$

with the definition of the dissipation of temperature fluctuation variance, $\kappa_T\overline{(\nabla\theta')^2} = 2\chi$. The heat flux, $\overline{w\theta'}$, can be estimated from the irreversible dissipation of temperature fluctuation variance, χ, and combining mean temperature vertical gradient.

With the concept of an eddy diffusivity, K_T, (2.41) can be expressed as

$$K_T\left(\frac{\partial T}{\partial z}\right)^2 = 2\chi. \tag{2.42}$$

Because there are inconsistent estimates of the universal constant, B, in the literature, we estimate the temperature spectral level, ζ,

$$\zeta = B\chi = \overline{\psi(k)k^{5/3}\epsilon^{1/3}} \tag{2.43}$$

where overbar denotes an average over the inertial-convection subrange, instead of χ.

2.4 Boundary layer flow

Near a sea-bed, a flow is attenuated and a boundary layer is developed. In a boundary layer, viscous effect is important and the shear is large.

The classic theory of a boundary layer is presented in Tennekes and Lumley (1972), and in Monin and Yaglom (1971). Here, I briefly describe a boundary layer in a homogeneous fluid with a steady mean flow, and a negligible pressure gradient. A logarithmic layer of velocity profile is derived to exist

$$\frac{U}{u_*} = \frac{1}{\kappa}\ln\frac{z}{z_0}. \tag{2.44}$$

where U is speed, $u_* = \sqrt{\tau_0/\rho}$, τ_0 is the bottom stress, $\kappa = 0.4$ is von Karman constant, z is the height from the bottom and z_0 is a roughness height at which $U = 0$.

According to Tennekes and Lumley (1972), the Reynolds stress is approximately equal to ρu_*^2, and the velocity gradient is $u_*/\kappa z$ within a log-layer. Therefore, the turbulent production is given by

$$P = -\overline{uw}\frac{\partial U}{\partial z} = \frac{u_*^3}{\kappa z}. \tag{2.45}$$

The fluid is generally close to homogeneous near the boundary (Antonia and Luxton 1971). For a shear flow, the buoyancy flux generally accounts for no more than 20% of the production of TKE (Osborn 1980), thus, the buoyancy flux can be neglected in equation (2.7). Combining equations (2.7) and (2.45) produces

$$\epsilon = \frac{u_*^3}{kz}, \tag{2.46}$$

The friction velocity, u_*, may be parameterized by the mean current with a drag coefficient, C_D, giving

$$u_*^2 = C_D U^2. \tag{2.47}$$

Hence, equation (2.46) can be written as

$$\epsilon = \frac{C_D^{2/3} U^3}{\kappa z}. \tag{2.48}$$

However, the Reynolds stress does not stay constant with increasing height in the log-layer due to Coriolis force and pressure gradient. Tennekes (1975) derived theoretically that the stress decreases by 30% at the upper limit of the boundary layer defined by $z = 0.03 u_*/f$, where f is Coriolis parameter. In Cordova Channel, the estimates of Reynolds stress obtained from ADCP data is not constant within the log-layer (Lu and Lueck 1996b).

In practice, the pressure gradient is not necessarily small and it can affect the flow. In our measurements, the pressure gradient was of first-order importance in the log-layer at a given height above the bottom. The records from the two tide gauges at the ends of the channel indicate a sea surface slope of up to 10^{-5}.

With the concept of mixing length (λ) which is related to the distance of vertical momentum transfer by eddies, the eddy viscosity, A_v, can be expressed as

$$A_v = u_* \lambda = \kappa z u_* \tag{2.49}$$

where $\lambda = \kappa z$ in the boundary layer. Using (2.47), (2.49) can be rewritten as

$$A_v = \kappa z \sqrt{C_D} U \tag{2.50}$$

In addition, combining the definition of the eddy viscosity, $A_v = -\overline{uw}/\left(\frac{\partial U}{\partial z}\right)$, (2.45) and (2.46), the eddy viscosity can be expressed as

$$A_v = \frac{\epsilon}{\left(\frac{\partial U}{\partial z}\right)^2}. \tag{2.51}$$

2.5 Richardson number

Shear instability is the main source of energy for generating turbulence. However, in a stratified flow, the stratification always tends to suppress shear instability and hence turbulence. A criterion for examining the likelihood of the shear instability is the Richardson number, Ri, defined as

$$Ri = \frac{N^2}{\left(\frac{\partial U}{\partial z}\right)^2}. \tag{2.52}$$

When $Ri > 1/4$, the stratification is strong enough to maintain stability of the shear, while for $Ri < 1/4$, the flow is unstable (Miles 1961, 1986).

Chapter 3

Instrumentation

The instrument (TAMI) used in our measurements is a novel microstructure instrument developed by the Ocean Turbulence Lab at the University of Victoria (Lueck *et al.* 1996). It was designed for use in the open ocean. Unlike conventional instruments which travel through water to collect data, TAMI is moored and measures fluid variations advected past it by the ambient current.

3.1 Mechanics

The instrument (Figure 3.1, 3.2) looks like a towed body (Lueck 1987). It is 5m long and has a diameter of 0.6m at mid-body. Four fins are mounted on the aft end – two vertical fins provide the torque to rotate the instrument in response to changes of direction of the ambient current and two horizontal fins stabilize the pitch. A 3.5m long mast is oriented vertically through the center of the instrument. Two pairs of Sea-Bird thermometers and conductivity cells (Table 3.1) are mounted at each end of the mast, and a third pair of Sea-Bird sensors is mounted on the middle of the body. These three pairs of sensors measure mean temperature and salinity and their vertical gradients. Two rotor current meters (McPhee 1992) are mounted on the upper and lower halves of the mast for measuring the ambient current speed.

There are two pressure cases inside the instrument body. The first one, with a length of 1.5m and a diameter of 0.2m, is mounted in the front half of the vehicle. This case houses all electronics and carries six turbulence sensors, a tri-orthogonal accelerometer (ICSensors 3140-002), a flux-gate compass (KVH C-100), and a pressure

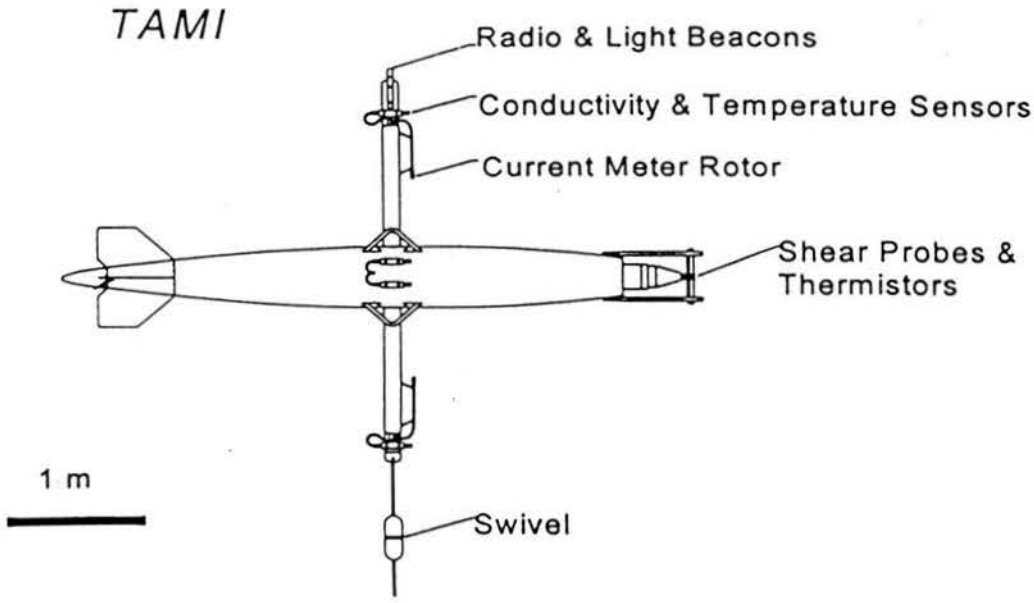

Figure 3.1: A sketch of TAMI (*T*ethered *A*utonomous *M*icrostructure *I*nstrument) which can be anchored using standard techniques and measures fluctuations of cross-stream velocity, temperature and their horizontal gradients at microscale using shear probes and thermistors. The vertical gradients of conductivity and temperature are measured with three pairs of Sea-Bird sensors. The speed of flow past the instrument is measured with two rotors on the upper and lower halves of the mast. The instrument is 5m long and has a diameter of 0.6m.

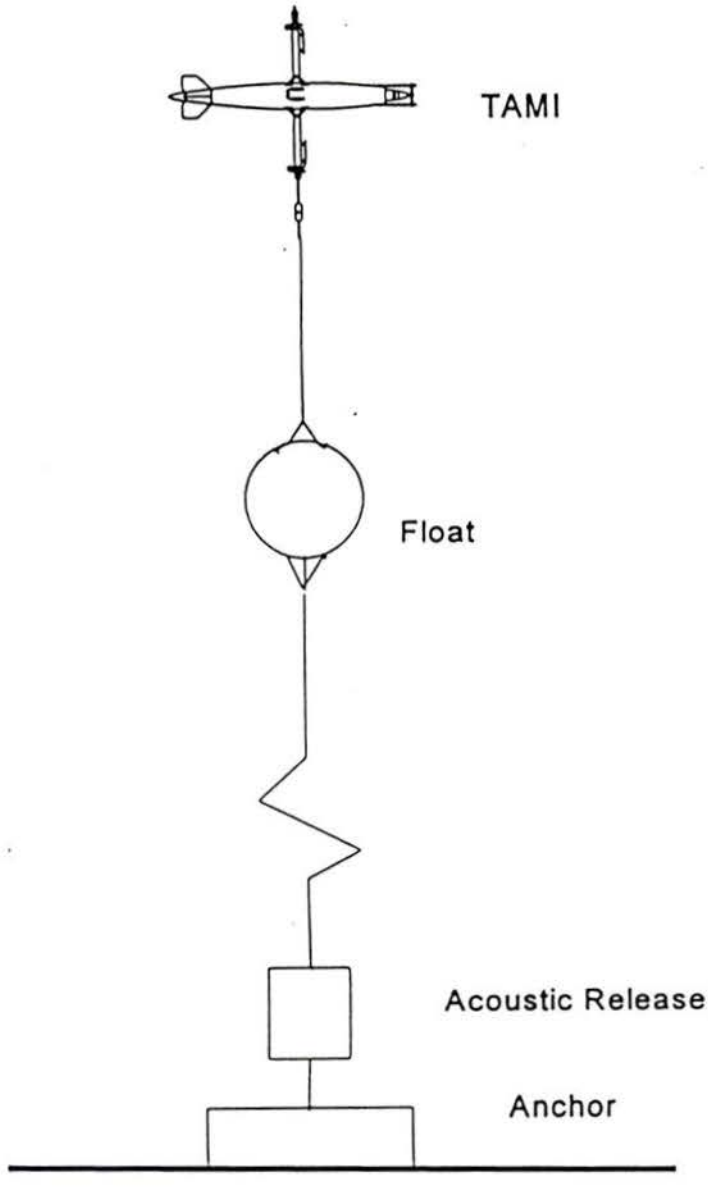

Figure 3.2: Mooring configuration of TAMI in Cordova Channel. TAMI was at 15m depth.

Sensor	Sensed signal	Sampling rate
Shear probe	$\frac{\partial v_1}{\partial x}, \frac{\partial v_2}{\partial x}$	128/s
Shear probe	v_1, v_2	16/s
Shear probe	$\frac{\partial w_1}{\partial x}, \frac{\partial w_2}{\partial x}$	128/s
Shear probe	w_1, w_2	16/s
Fast thermistor	$\frac{\partial T_1'}{\partial x}, \frac{\partial T_2'}{\partial x}$	128/s
Fast thermistor	T_1', T_2'	16/s
Acceleration	a_x, a_y, a_z	128/s
Sea-Bird C	S_1, S_2, S_3	2/s
Sea-Bird T	T_1, T_2, T_3	2/s
Current meter	U_1, U_2	1/128s
pressure	P	2/s
Compass	θ	2/128s

Table 3.1: Sensor locations and sensed signals

transducer (Keller P-10-50) (Table 3.1). The turbulence sensors – two pairs of shear probes for measuring $v, \partial v/\partial x$ and $w, \partial w/\partial x$, and one pair of FP07 fast thermistors for measuring $T, \partial T/\partial x$ – are mounted onto a conical cap on the front of the case. The accelerometers and the compass are within the cap. A guard is mounted on the front of the body to protect the turbulence sensors. The pressure sensor is mounted in the rear of the case. A second pressure case, with the identical size of the first case but without a conical cap, carries batteries and is mounted in the aft half of the vehicle.

The instrument weighs 4500 Nt in air and is 550Nt buoyant in water. However its effective (enclosed and virtual) mass is 1000kg underwater which serves to dampen high-frequency vibrations.

The instrument is connected to a cable with a swivel at the lower end of the mast. An anchor is attached to the lower end of the cable.

3.2 Electronics

The electronics of TAMI manipulate data acquisition, data processing and data storage. The operation of the electronics is as follows:

(1) At the beginning of a sampling cycle of 5 minutes, a watchdog timer wakes the system.

(2) The signals are sampled for 128 seconds.

(3) The data are processed which takes 3.5 seconds.

(4) The processed data are stored in nonvolatile memory.

(5) The system then sleeps for the rest of the 5 minute cycle.

(6) After every six hours, the processed data as well as all unprocessed data from the last sampling cycle are saved on a disk.

In a sampling cycle, the electronics operate 19 sensors to collect data at 5 different sampling rates (Table 3.1). Turbulent velocities and temperature are differentiated to produce signals which are proportional to their shears and temperature gradient. These turbulent shear and temperature gradients as well as accelerations are sampled at 128 samples per second. The acceleration measurements, including vertical, lateral and longitudinal components, are used to sense vibrations near the shear probes and to determine the roll and pitch of the instrument. The accelerometers respond to gravity, so that the longitudinal and lateral acceleration at low frequencies can be interpreted as pitch and roll. The signal at higher frequencies comes primarily from inertial vibration. Turbulent velocity and temperature for estimating the vertical flux of heat are sampled at the rate of 16 samples per second. The Sea-Bird sensors and pressure gauge are read twice per second. The rotation of the rotors is counted over 128 seconds. The compass is read at the beginning and at the end of the 128 second sampling intervals. A 12-pole Butterworth low-pass filter is employed for anti-aliasing, with one bank set to 43Hz for the turbulent shear, temperature gradient and acceleration signals, and a second bank set to 5Hz for turbulent velocity and temperature signals.

The data processing is executed by a digital signal processor (DSP – AT&T DSP-32C). Data processing greatly reduces the volume of the stored data. For example,

Collected signal	Processed signal	Type
$\frac{\partial v}{\partial x}, \frac{\partial w}{\partial x}, \frac{\partial T'}{\partial x}, a_x, a_y, a_z$	spectra	I
v, w, T'	spectra	II
w, T'	co-spectrum	III
T_{SB}, S_{SB}, P	minimum, maximum, mean, std	IV

Table 3.2: The data processed by DSP

the unprocessed data are 320 KBytes in each sampling cycle and will accumulate to 45 MBytes in 24 hours and 315 MBytes in one week. However, the data accumulate to only 2.9 KBytes in a cycle after processing with the DSP and reaches only 840KBytes in a day.

The data are divided into 4 types for processing (Table 3.2). Each signal of type I is divided into 4 segments for which spectra are calculated. These 4 spectra are averaged into a single spectrum. Finally the single spectrum is band-averaged into 21 frequency bins with uniform intervals in logarithmic space (Table 3.3).

Each of the turbulent velocities and temperature fluctuations of type II is processed into a single spectrum, then the spectrum is band-averaged into 19 frequency bins of equal spacing in log space (Table 3.3)

Statistics, including maximum, minimum, mean and standard deviation, are calculated for all signals of type I and II. These statistics are used to judge data quality.

Type III data, turbulent velocity and temperature fluctuation, are processed into a co-spectrum. Only the real part of the co-spectrum is retained and band-averaged into 19 frequency bins as are the data of type II.

Statistics of fine-structure data (type IV), including mean temperature, salinity and pressure, are computed twice. The first calculation is done using all data of a signal. The second calculation uses only those data which are within 4 standard deviations of the mean.

The instrument has been proven reliable for detecting turbulence in conditions

Bin	f [Hz]	$\triangle f$ [Hz]	Bin	f [Hz]	$\triangle f$ [Hz]
1	0.032	0.031	1	0.008	0.008
2	0.063	0.031	2	0.016	0.008
3	0.094	0.031	3	0.024	0.007
4	0.14	0.063	4	0.035	0.016
5	0.20	0.062	5	0.051	0.016
6	0.30	0.125	6	0.075	0.031
7	0.42	0.125	7	0.105	0.031
8	0.61	0.25	8	0.15	0.063
9	0.86	0.25	9	0.22	0.062
10	1.2	0.5	10	0.31	0.125
11	1.7	0.5	11	0.43	0.125
12	2.5	1	12	0.62	0.25
13	3.5	1	13	0.87	0.25
14	5.0	2	14	1.25	0.5
15	7.0	2	15	1.75	0.5
16	10	4	16	2.5	1
17	14	4	17	3.5	1
18	20	8	18	5.0	2
19	28	8	19	7.0	2
20	40	16			
21	56	16			

Table 3.3: Twenty-one and nineteen frequency bins for spectrum calculations. f is arithmetic average of starting and ending frequency at each bin. Δf is width for each bin.

similar to the open ocean (Lueck *et al.* 1996). However, the conditions in Cordova Channel are different from those in the open ocean. The first major difference is the current which has typical speed of 0.60 ms^{-1} in the tidal channel compared to 0.10 ms^{-1} in the open ocean (Kunze and Sanford 1984). As a result, the turbulence in the tidal channel will be undersampled making it impossible to use equation (2.17) to estimate the dissipation rate and instead we use equation (2.33). For example, only 55% of variance of a velocity spectrum with a dissipation of 10^{-5} W kg^{-1} is resolved when mean flow speed is 0.6 m s^{-1}. Therefore, we utilize the inertial-subrange technique. In addition, the vibration of the instrument, mainly due to eddy shedding (Moum and Lueck 1985), is expected to be larger in the tidal channel than that in the

open ocean. The vertical scale of turbulent eddies in the open ocean is typically 0.1 - 0.5m. The size of eddies in Cordova Channel will be O(20m) and this may induce considerable buffeting of the instrument because it is only 5m long. Because of the large eddy scale in the channel, the inertial-subrange is expected to be wide enough to obtain dissipation estimates. The rate of dissipation is several orders of magnitude larger than in the open ocean, where typical values are (1 - 1000)$\times 10^{-10}$ W kg^{-1} (Gargett and Holloway 1984) and usually larger dissipation occurs in the upper layer with stronger mixing compared to samller values in the deep layer. Therefore, the intensity of the voltage output of the shear probe will be much larger than that in the open ocean, and we expect this to compensate for the effects of eddy shedding and buffeting.

Chapter 4

Background

4.1 Experiment

The experiment was conducted in Cordova Channel (Figure 4.3) between the Saanich Peninsula and James Island. Cordova Channel is oriented northwest and forms a minor side passage connecting the George Strait basin with the Pacific Ocean. The channel is approximately 5 km long and 30 m depth on its central line. The channel is 1500 m wide on the surface and 650 m and 500 m wide at the 10 m and 20 m isobaths, respectively, on a cross-channel section near our instruments. The isobaths basically follow the shorelines.

The field work was a collaborative experiment, involving several investigators and a number of different instruments. Here I will describe the major measurements (for the major instruments see Table 4.4) pertinent to the description of turbulence in Cordova Channel. A meteorological station was set up by Dr. Farmer's group of IOS on September 16, 1994, four days before the beginning of the main program at Cordova Spit Station. The meteorological instruments recorded 5-minute-averaged wind velocity, air temperature and barometric pressure. An Anderaa current meter (CMI) of Dr. Farmer's group collected vector averaged current readings at 2 minute intervals starting on the afternoon of September 19. An acoustic scintillation system was also set up by Dr. Farmer's group for measuring the level of the refractive index fluctuation due to velocity and temperature turbulence. An ADCP of Dr. Lueck's group was mounted on the bed for measuring velocity profiles, from 3.5m above the bottom to 4m below the surface, at 1m intervals. Its data are used to

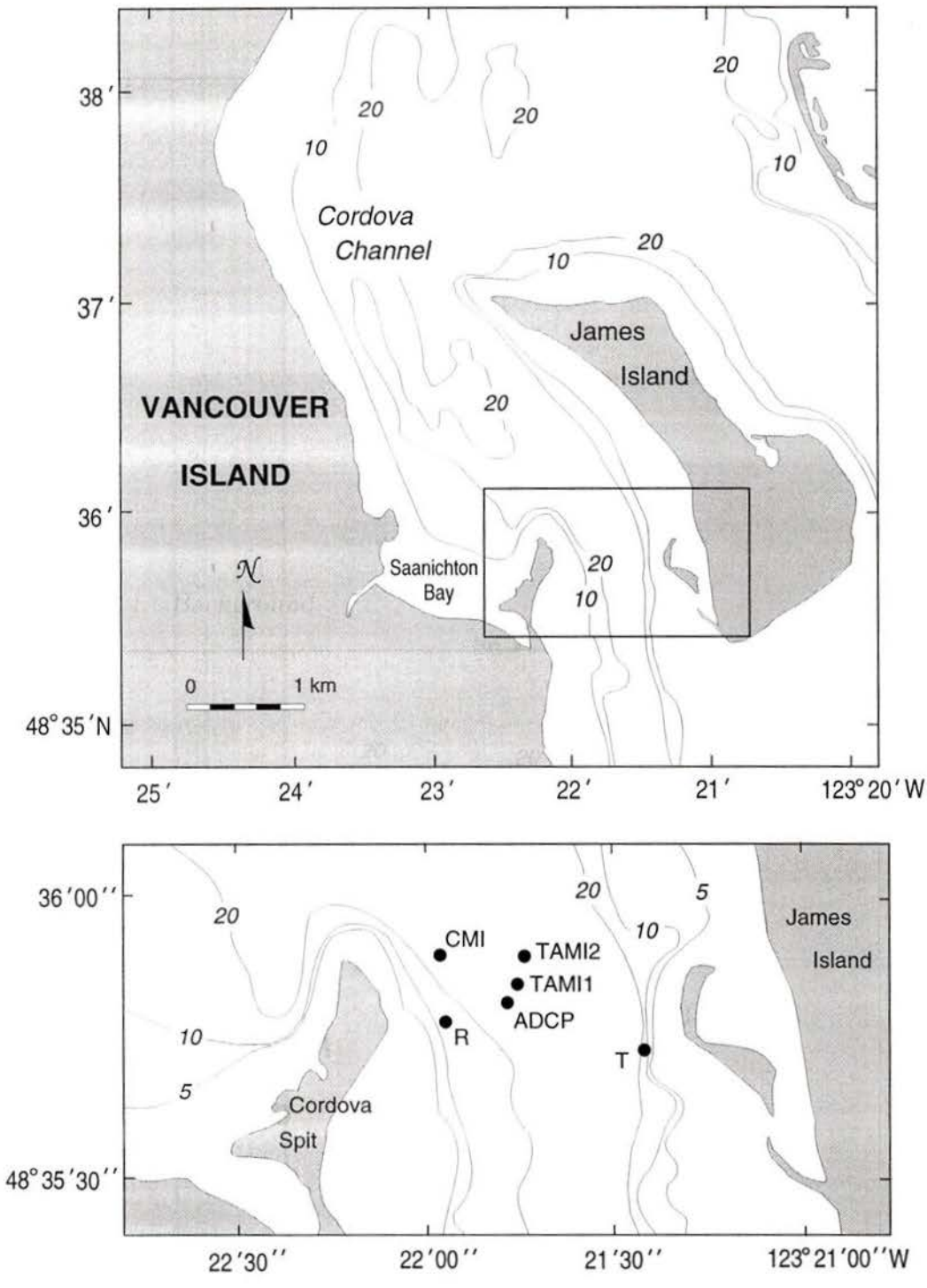

Figure 4.3: Cordova Channel, B.C. Solid dots represent the positions of the Anderaa current meter (CMI), the ADCP, the acoustic scintillation system (R: receivers, T: transmitters), TAMI and tide gauges (G1 and G2). The TAMI1 indicates the location of TAMI during the first deployment, the TAMI2 during the second deployment.

Instrument	Position	Ref. to TAMI2	Depth
Meteorological station	48°35.850′N, 123°22.250′W	N/A	4m above sea surface
CMI	48°35.902′N, 123°21.960′W	West, 300m	20m
Acoustic scintillation system	N/A	its path was 130m south	15m
ADCP	48°21.7885′N 123°35.806′W	South, 90m	bottom mounted
(1st deployment) TAMI (2nd deployment)	48°35.856′N, 123°21.744′W 48°35.892′N, 123°21.733′W	40m 0m	15m
CTD profiler	48°35.0′N, 123°21.8′W	South, 150m	Surface to bottom
(1st) Tide gauges (2nd)	48°36.43′N 123°23.41′W 48°34.78′N, 123°21.90′W	North, 2.5km South, 2.5km	Bottom

Table 4.4: The positions of the major instruments and their relative distances to TAMI

estimate depth averaged velocity, shear, logarithmic layer height, and the production of turbulent kinetic energy. CTD profiles, using Sea-Bird sensors, were taken by Dr. Farmer's group during the period of September 25 - 30. The CTD profiler collected temperature, salinity profiles three times every hour. In addition, two tide gauges were set up by Canadian Hydrographic Service on September 19 at both ends of the channel.

TAMI was deployed in the afternoon of September 21 and recovered in the morning of September 26. After a ballast adjustment, it was redeployed in the morning of September 27 and recovered in the morning of September 30. The positions of both

deployments were close to the center of the channel. The current meter at the top mast was stalled by jellyfish during the first deployment and was dismounted for the second deployment.

Other work includes Lagrangian current measurements by Dr. D'Asaro of the APL/UW, Seattle, WA, using a neutrally-buoyant float and the measurement of acoustic fluctuation induced by waves traveling through turbulence by Dr. Deane of MPL/Scripps, San Diego, CA, using acoustic daylight receiving arrays. In addition, zooplankton were sampled by Dr. Mackas of IOS.

4.2 Instrument movement and orientation

The signal from the compass was used to (1) examine the stability of the instrument by comparing the current direction measured by TAMI against the measurements of the ADCP and the CMI (See Appendix A), and (2) convert the speed measured with the rotor on the mast into current vectors. The variation of the heading of the instrument (Figure 4.4 and 4.5) was nearly continuous and smooth in each tidal cycle. Abrupt change of the heading only occured during the short periods of weak flow near the turning of the tide. Therefore, the orientation of TAMI was usually stable. There were excellent agreements between the current speeds and directions measured by TAMI and by other instruments – the CMI and the ADCP (Figure A.54 and A.55). These agreements indicate that TAMI was directed into the current as expected.

For an ideal and stable condition, the instrument is "fixed" at a point above its anchor and has no motion except rotation in response to changes of direction of the current. In reality, the instrument is not "fixed". Its quasi-steady position is determined by the conditions of zero total force and zero total torque. Without a current (Figure 4.6A), there are three forces – weight (W), buoyancy (B) and the tension (T) from the cable, directed vertically. The center of the weight is slightly

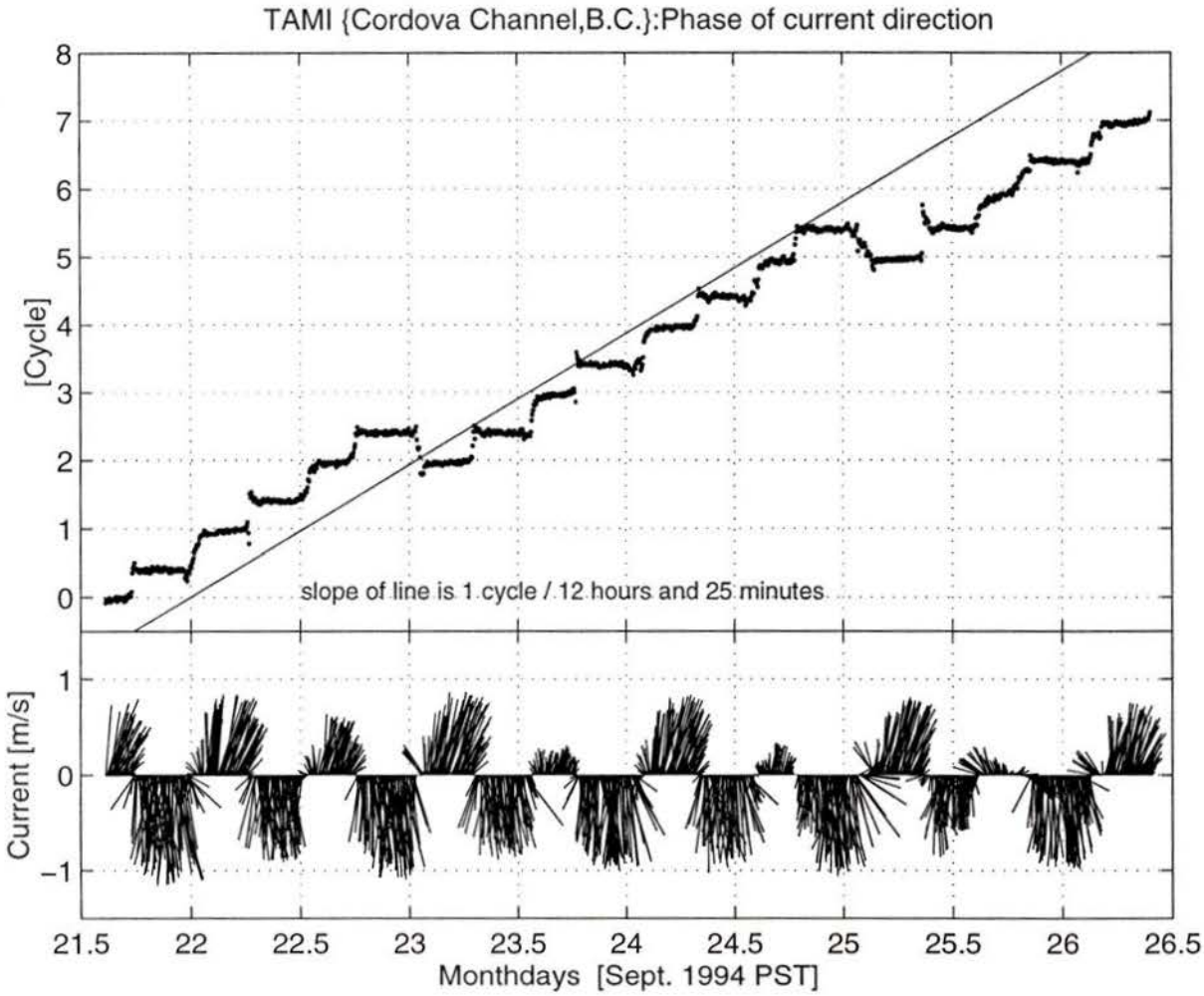

Figure 4.4: The phase of TAMI heading indicated that the instrument was usually stable except during periods of weak current around the turning of the tide. Upper panel: Phase of current converted from the heading of TAMI's. The straight line indicates the phase of the semi-diurnal tide. Lower panel: Current vector sticks, which upward direction indicates ebb, obtained by combining the instrument heading and the current speed. Vertical (horizontal) direction denotes the along-channel (cross-channel) component.

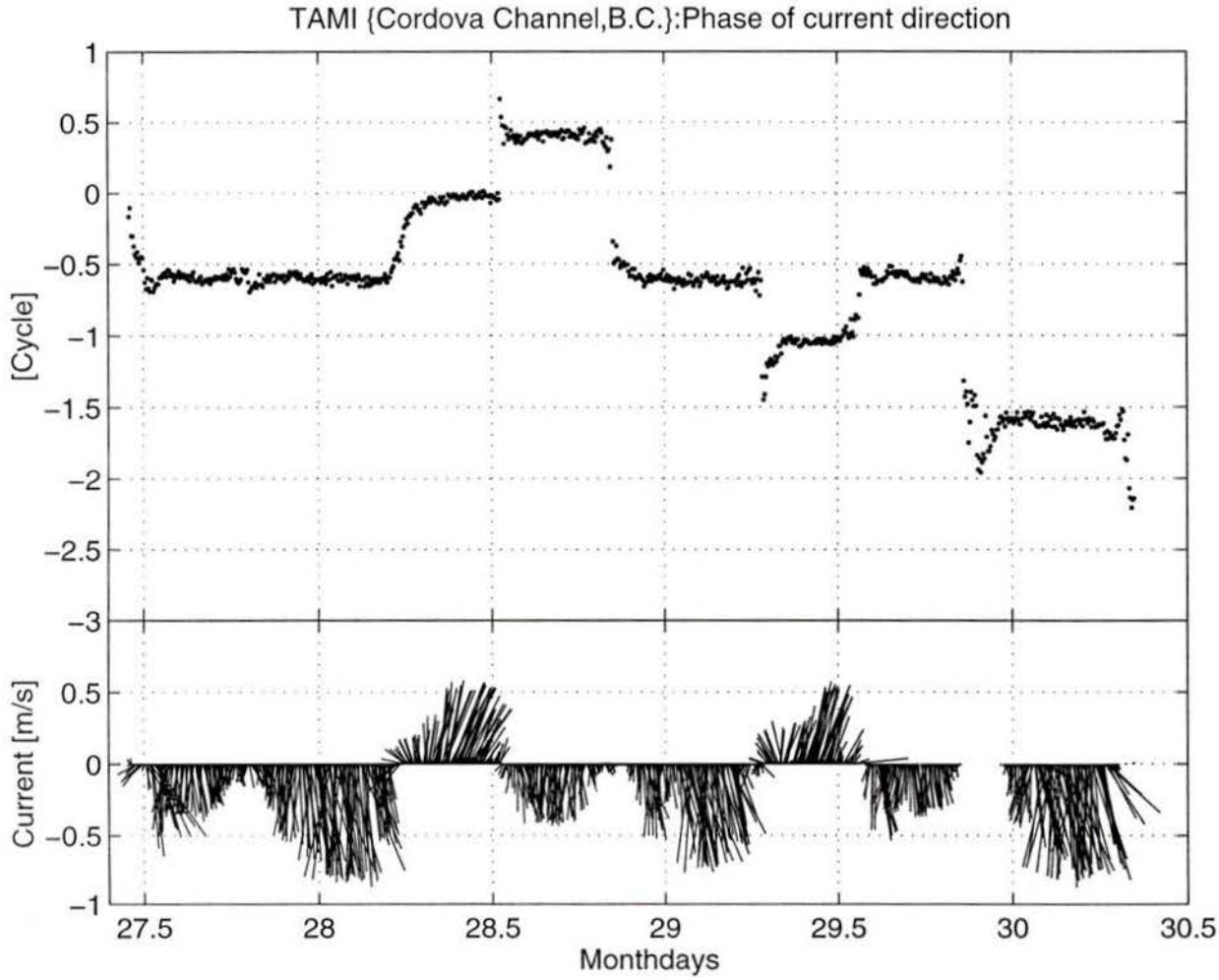

Figure 4.5: The phase of TAMI's heading and current vectors during the second deployment as in Figure 4.4.

forward of the center of the buoyancy, giving the instrument a downward pitch. The pitch was -14° for the first deployment and was reduced to -7° (also downward) for the second deployment by removing a weight mounted on the guard.

When water moves against the instrument, drag forces the instrument backwards and the vehicle is drawn downwards by the cable. Also, a negative lift (downwards) is generated by the tail fins. These two forces (F_D and F_L) generate counterclockwise torques around the bottom of the mast to reduce the downward pitch (Figure 4.6B). There still exists lift when the pitch is zero (Figure 4.6C) because of an intentional bend in the tail fins. However, this lift is too small to compensate the counterclockwise torque by the drag, so the pitch continues to increase (although less strongly) with increasing flow (Fig 4.6D). The maximum pitch was 3° for both deployments. Seventy percent of pitch records are between -10° and 3° during the first deployment and 80% of the records are between -6° and 2° during the second deployment.

The angle of the cable from the vertical can be estimated as $\tan^{-1}(F_D/(B-W))$, where F_D is the drag, and we ignore the small lift. F_D is about 300N (calibrated by towing from a ship) at 1 ms^{-1} and $B - W$ is approximately 550N. Thus, the vertical displacement is approximately 2m in a current of 1 ms^{-1} and 0.5m in 0.6 ms^{-1}. The horizontal displacement is 7.5m in a current of 1 ms^{-1}. The vertical displacement of the instrument is indicated by the difference between the variation of the pressure recorded by TAMI (Figure 4.7) and the tide gauges. The difference of pressure (TAMI - tide gauge) indicates that the vertical displacement is mostly between 0.1 and 1m (Figure 4.8). This vertical displacement is tightly correlated with the current speed. The maximum vertical displacement occured at day 25.8 while there was no corresponding extrema of current speed. This event was accompanied by large roll and suggests that the instrument may have been momentarily broadside to the flow. In general, the roll of the instrument varied between -5° and 5° for 95% of the samples of both deployments.

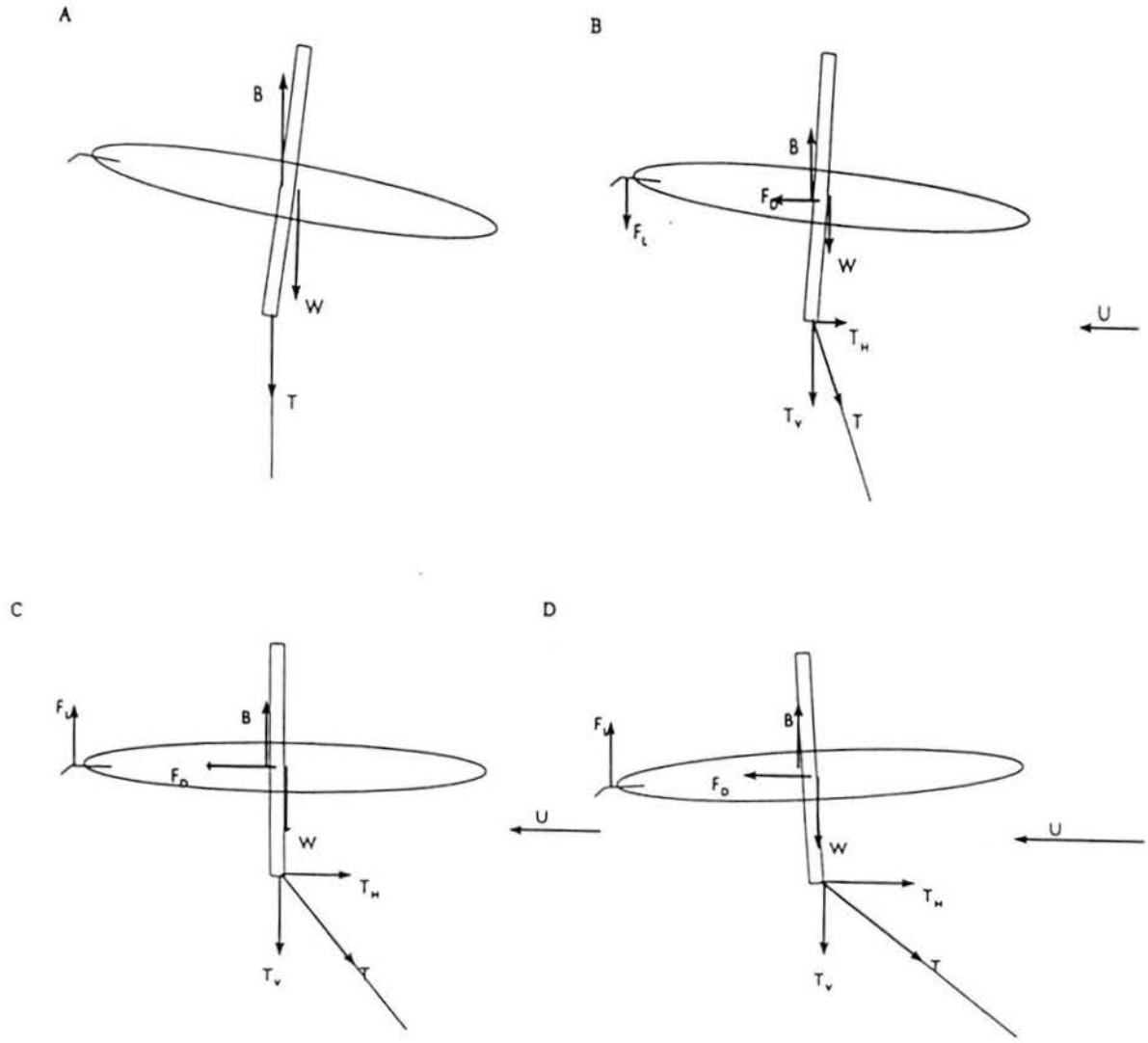

Figure 4.6: The orientation of the instrument. Case A: No current, B denotes the buoyancy, W the weight and T the tension in the cable. Case B: The instrument has a negative pitch (the nose downwards) with a current (U), F_D is the drag and F_L is the lift (downward indicates negative). Case C: The instrument has zero pitch with a current (U), the lift, F_L, is positive due to an intentional bend of the tail fins. Case D: The instrument has a positive pitch with a current (U).

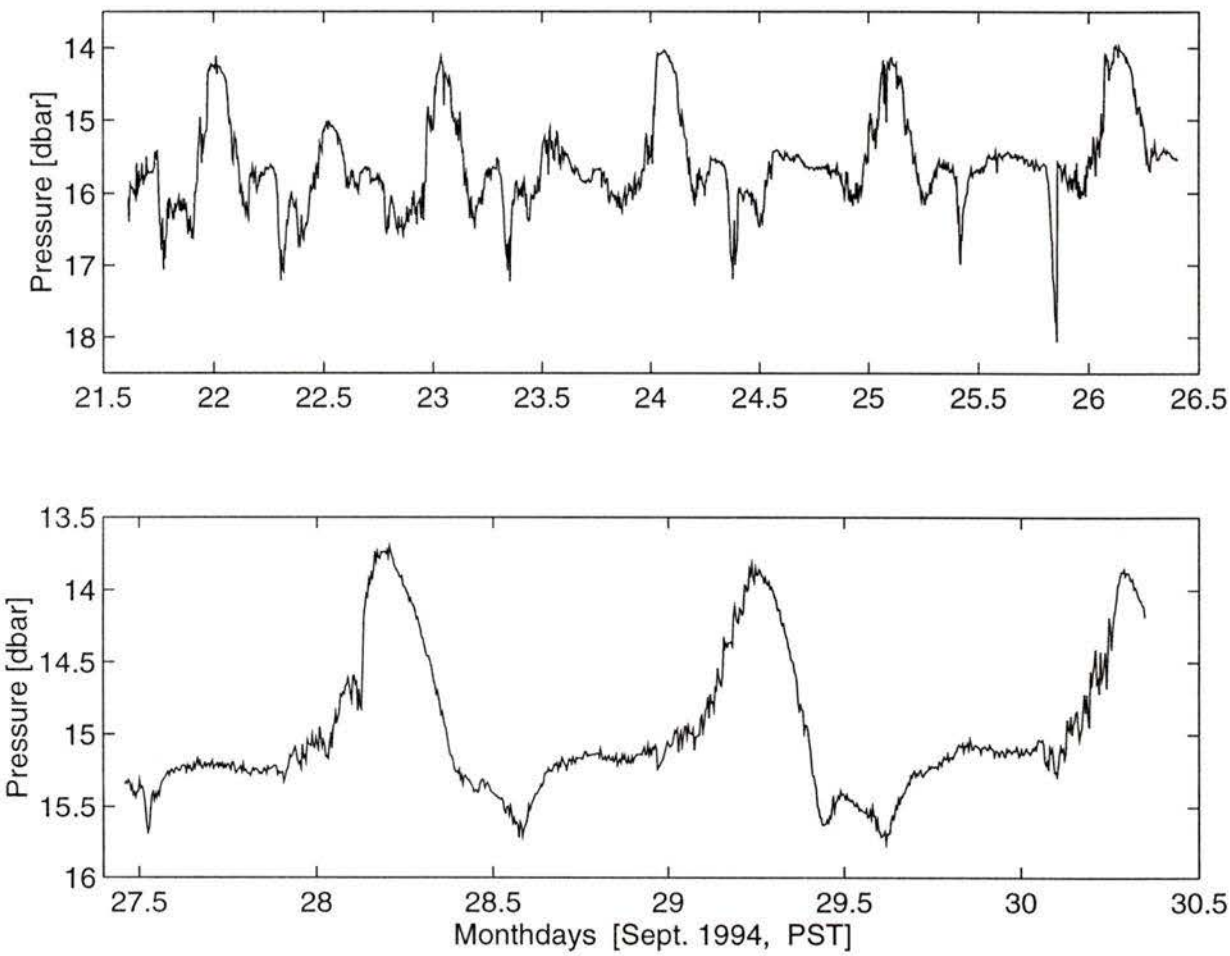

Figure 4.7: Upper panel: Pressure during the first deployment, showing tidal modulation; Lower panel: Pressure during the second deployment.

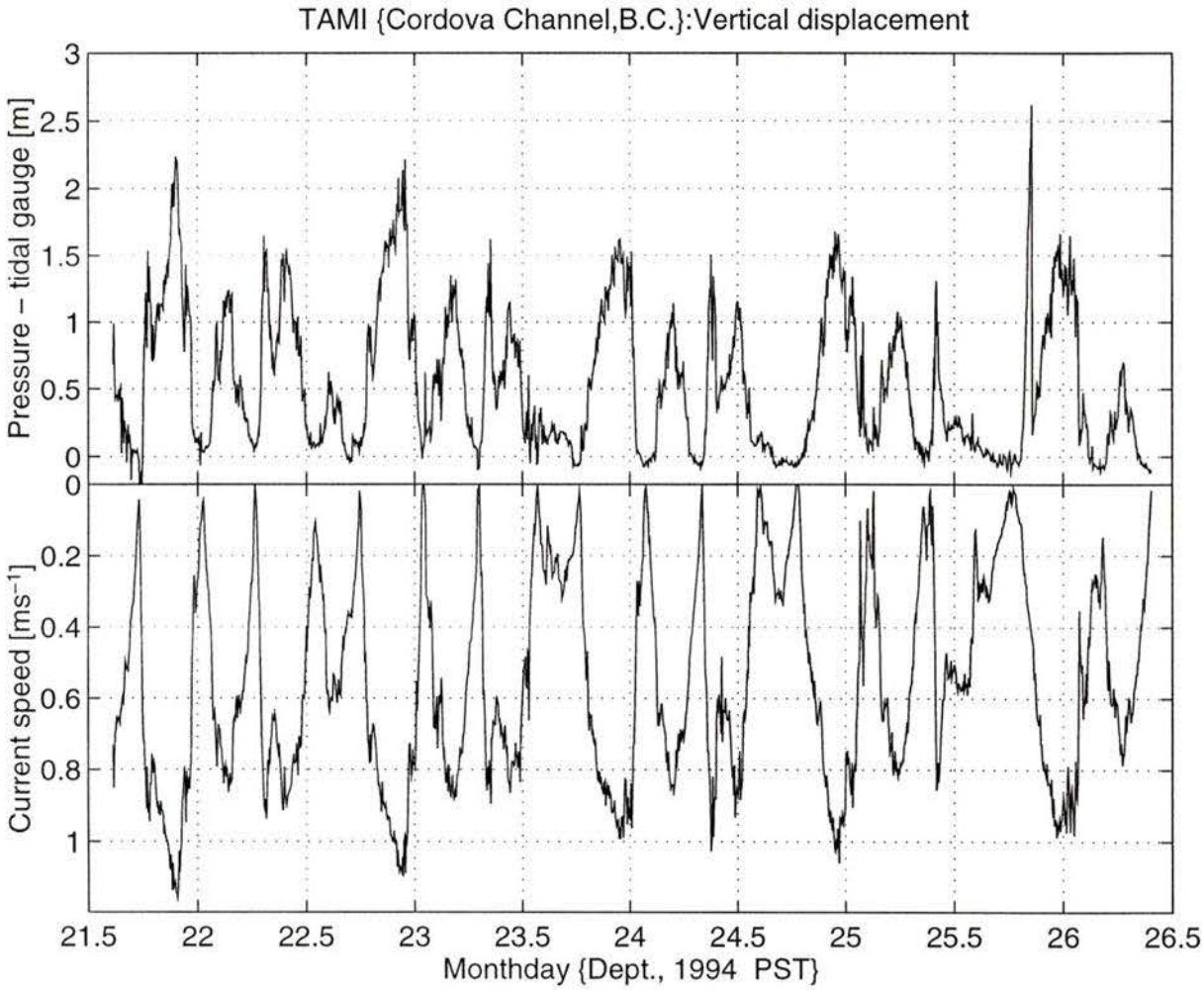

Figure 4.8: Upper panel: Vertical displacement of the instrument obtained by using the variation of the pressure of TAMI minus the tide measured by the bottom mounted gauges (IOS). Lower panel: Current speeds.

4.3 Tidal current

The flow in Cordova Channel was mainly tidal (Robinson 1983; Farmer *et al.* 1987; Foreman *et al.* 1994) and its major constituents are M_2, K_1, S_2 and O_1 (Robinson 1983; Foreman *et al.* 1994). The tide ranged about 2m and was accompanied by strong currents with peak speed of 1.2 m s^{-1}. The measured current was mainly semi-diurnal (M_2) (Figure 4.4) during the first deployment and mixed (M_2 and K_1) (Figure 4.5) during the second deployment due to the fortnightly modulation of the tide.

A least square fit to the tidal signal using sinusoidal variables ($\sin(\omega_n t)$ and $\cos(\omega_n t)$, where ω_n is frequency of the n^{th} tidal constituent, t is time and $n = 1, 2, 3, 4$), was applied to the two current components (u_{ew} – the east-west component and u_{ns} – the north-south component). This method is a harmonic analysis – a common processing technique (Godin 1972; Foreman 1978). However, the lengths of the time series are only 4.8 days for the first experiment and 2.9 days for the second deployment, too short for accurate estimates of the amplitude of the tidal coefficients. A fit employing four constituents, i.e. M_2, K_1, S_2 and O_1, was used because it gives better results (Figure 4.9 and 4.10) than using fewer constituents. Adding M_4 to include rectification by non-linearity does not improve the fit.

The harmonic constants are listed in Table 4.5. The tidal current explains 92% (91%) of the variance of the measured flow during the first (second) deployments. The south-eastward mean current was 0.19 ms^{-1}. The M_2 constituent is the major component contributing almost 50% of the magnitude of the current speed during these two deployments.

The parameters of the current ellipses of the four constituents, obtained using the method of Foreman (1978), are shown in Table 4.6. The major axes were much longer than minor axes for all constituents, as expected for a channel flow. For individual constituents, the major axes of M_2 were much longer than those of other constituents.

First experiment	U_{ew} [ms^{-1}]	θ_{ew} [°]	V_{ns} [ms^{-1}]	θ_{ns} [°]
M_2	0.320	179.8	0.612	10.7
K_1	0.065	124.9	0.161	276.0
S_2	0.087	179.8	0.190	345.8
O_1	0.075	339.0	0.140	126.6
mean term	0.146		-0.122	
Second experiment				
M_2	0.291	67.7	0.428	258.7
K_1	0.068	120.3	0.150	323.9
S_2	0.088	270.9	0.108	95.6
O_1	0.162	176.5	0.207	347.7
mean term	0.132		-0.136	

Table 4.5: The harmonic constants of the tide during the experiment. U_{ew} and V_{ns} denote magnitudes of u_{ew} and v_{ns} respectively. θ represents their phases with PST.

1st deployment	L [ms^{-1}]	α [°]	D [ms^{-1}]	Rotation
M_2	0.688	332	0.054	clockwise
K_1	0.171	335	0.030	counterclockwise
S_2	0.208	335	0.019	counterclockwise
O_1	0.155	328	0.037	counterclockwise
2nd deployment				
M_2	0.516	325	0.037	clockwise
K_1	0.162	334	0.025	clockwise
S_2	0.139	321	0.006	clockwise
O_1	0.262	321	0.020	counterclockwise

Table 4.6: The parameters of the ellipses of the four constituents. L denotes the length of major axis of an ellipse. α represents the direction of the major axis, bearing clockwise and starting from the north. D denotes the length of a minor axis.

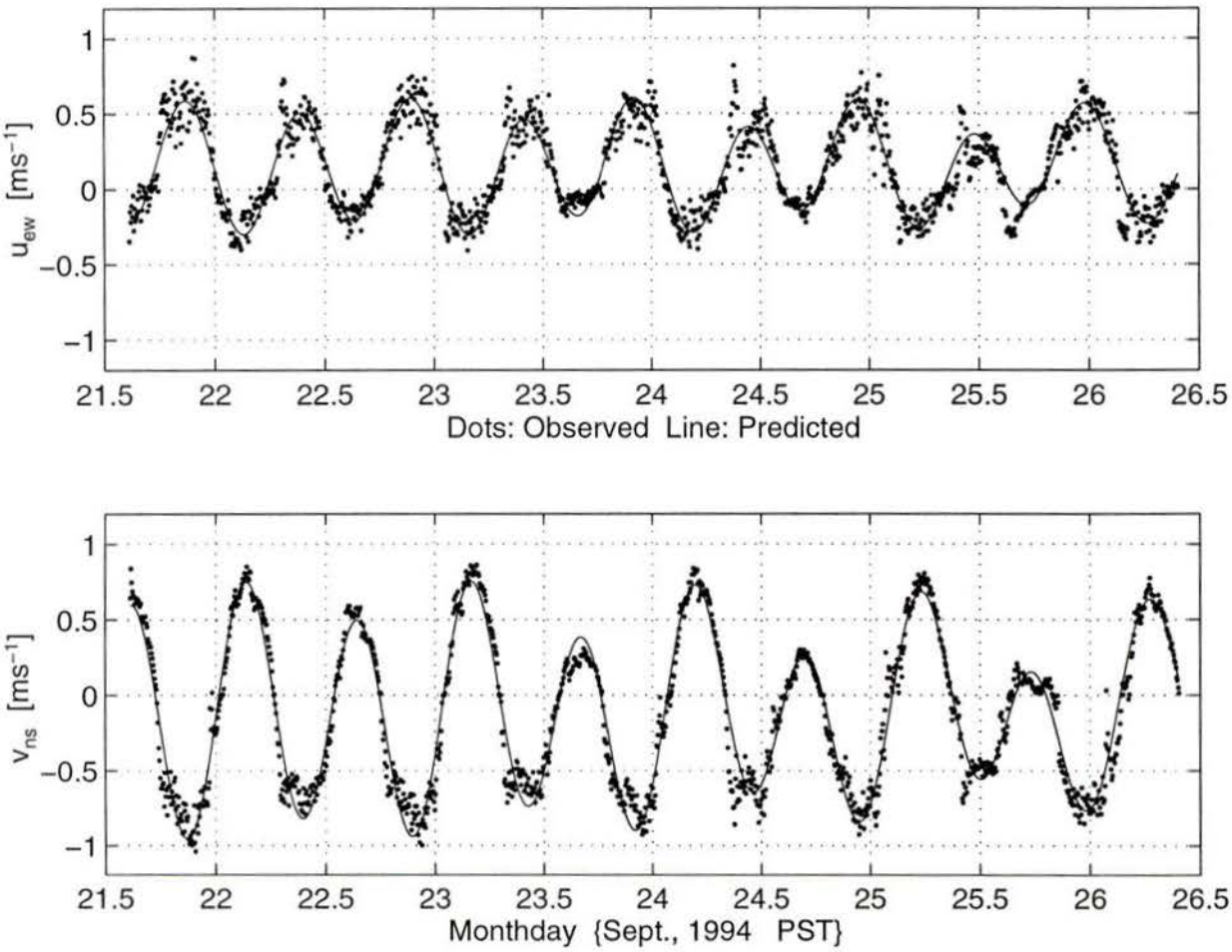

Figure 4.9: Comparison of the observed (dots) and predicted (curves) current components during the first deployment. The predicted current combines the four constituents, M_2, K_1, S_2, O_1. The harmonic constants are in Table 4.5. Upper panel: East-west component. Lower panel: North-south component

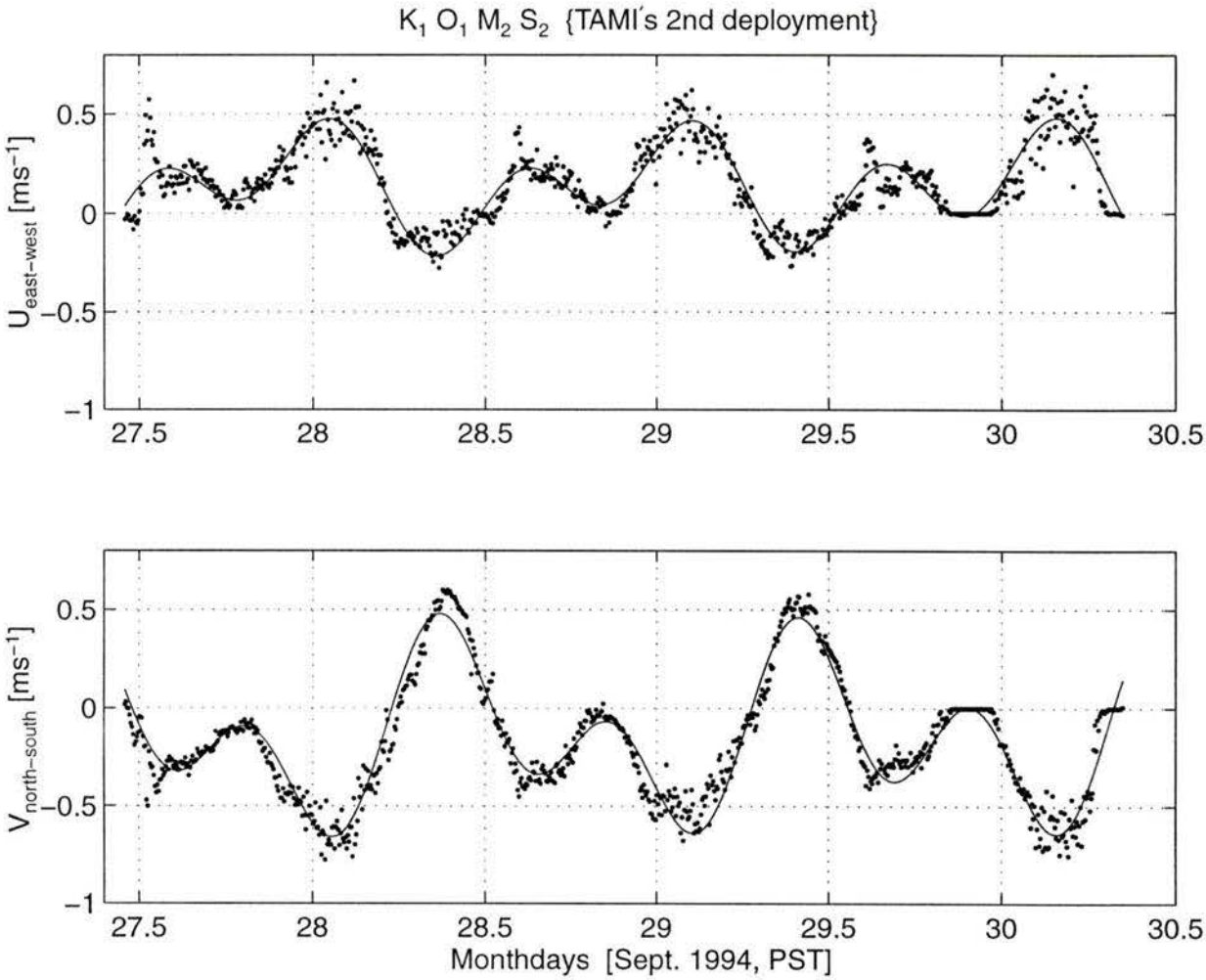

Figure 4.10: Comparison of the observed (dots) and predicted (curves) current components during the second deployment as in Figure 4.9.

The directions of all major axes were very close to each other (Table 4.6), ranging from 321° to 335° (bearing clockwise starting from the north). These directions were also close to the direction of the channel, which is approximately 327°.

The measured currents had a principle axis of 345° during the flood and 147° during the ebb (Figure 4.11). The directional asymmetry of the flood and ebb arose from the geometry of the channel. During the ebb, the direction of the flow was closer to the direction of the tidal ellipse than during the flood. Therefore, a principle axis of 327°, which was aligned to the direction of the ebb, was chosen as the axis for decomposing the measured current into two components, namely, the along-channel component, v, and the cross-channel component, u (Figure 4.9 and 4.10). The magnitude of the along-channel component, typically 0.6 ms^{-1} was much greater than that of the cross-channel component, 0.1 ms^{-1}. A mean current of 0.19 ms^{-1} was evident from the larger average current during the ebb compared to the flood.

The residual current – the observed less the tidal current – accounts for 8.8% of the tidal kinetic energy (KE) during the first deployment, and 11.2% of the tidal KE during the second deployment. The residual current (Figure 4.12) was scattered, random and isotropic during the first deployment and had nearly identical variances for two components, $\overline{u^2_{residual}} = (1 \pm 6\%)\overline{v^2_{residual}}$. The anisotropy of the residual current during the second deployment (Figure 4.13), stems from inaccurate constants due to the short record length. The fitted and the measured data, particularly in v_{ns}, are phase shifted (Figure 4.10). The residual currents represent 2-D horizontal eddies which are probably generated by flow separation and topographic effect. Numerical modelling (Maddock and Pingree 1978; Pingree 1978) reveals that two-dimensional horizontal eddies can be generated near a headland. In a tidal flow parallel to a coastline, vorticity is produced because the flow close to the coast experiences more bottom friction, due to the shallower depth, than the deeper flow farther from the shore. If the coastline is straight, then there is no net vorticity generated due to

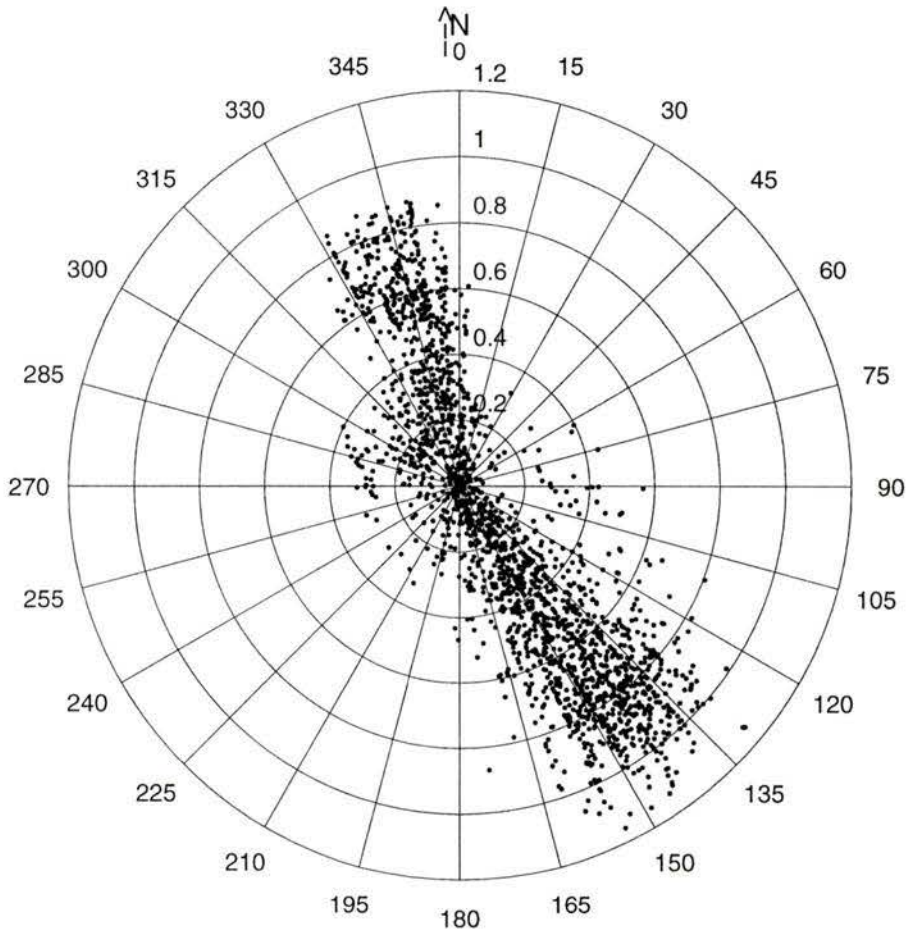

Figure 4.11: The current plotted in polar coordinates (bearing clockwise starting from the north). Radius indicates the current speed and azimuth gives the direction of the current ([°]).

an equal and opposite contribution from both sides of the channel. However, with a headland, a vorticity gyre will separate from the headland due to the tendency of streamline overshoot (Robinson 1983). Flow separation occurs behind a headland due to a reversal of the pressure gradient (Schlichting 1955, Kundu 1990). In Cordova Channel, sources of eddy generation are likely the north end of James Island and Cordova Spit.

Log-layer heights, deduced from the measurement of the ADCP (Lueck and Lu 1996), varied tidally and reached 15m, the nominal position of TAMI. However, only 16% of the 306 velocity profiles taken over 4.5 days had logarithmic layers with heights greater than 15m. Therefore, TAMI was out of the log-layer during most of the time of the experiment.

4.4 CTD profiles

Throughout the experiment, water became fresher and warmer (Figure 4.14 and 4.15), due to Fraser River runoff which was brought southwards by the mean current. [For salinity correction see Appendix A.] The variation of density was produced primarily by the variation of the salinity, and salinity record shows the modulation by the tide. The temperature had more fluctuations at higher frequencies than the salinity during both deployments. The $T - S$ relationship (Figure 4.16) confirms that the warmer fluctuations was correlated with freshening and vice versa.

CTD profiles illustrate that the channel was fairly well mixed during periods of strong current, particularly during the ebb. For example, a profile taken at midnight of day 25 is shown in Figure 4.17. Numerous inversions suggest that flow was turbulent. These inversions were overturns because they only formed local extrema.

Another CTD profile taken when the flow was weak and during a flood (Figure 4.18) provides a different picture – the water below approximately 15m depth was weakly stratified with a small slope in S, T and hence in σ_t. The stratification

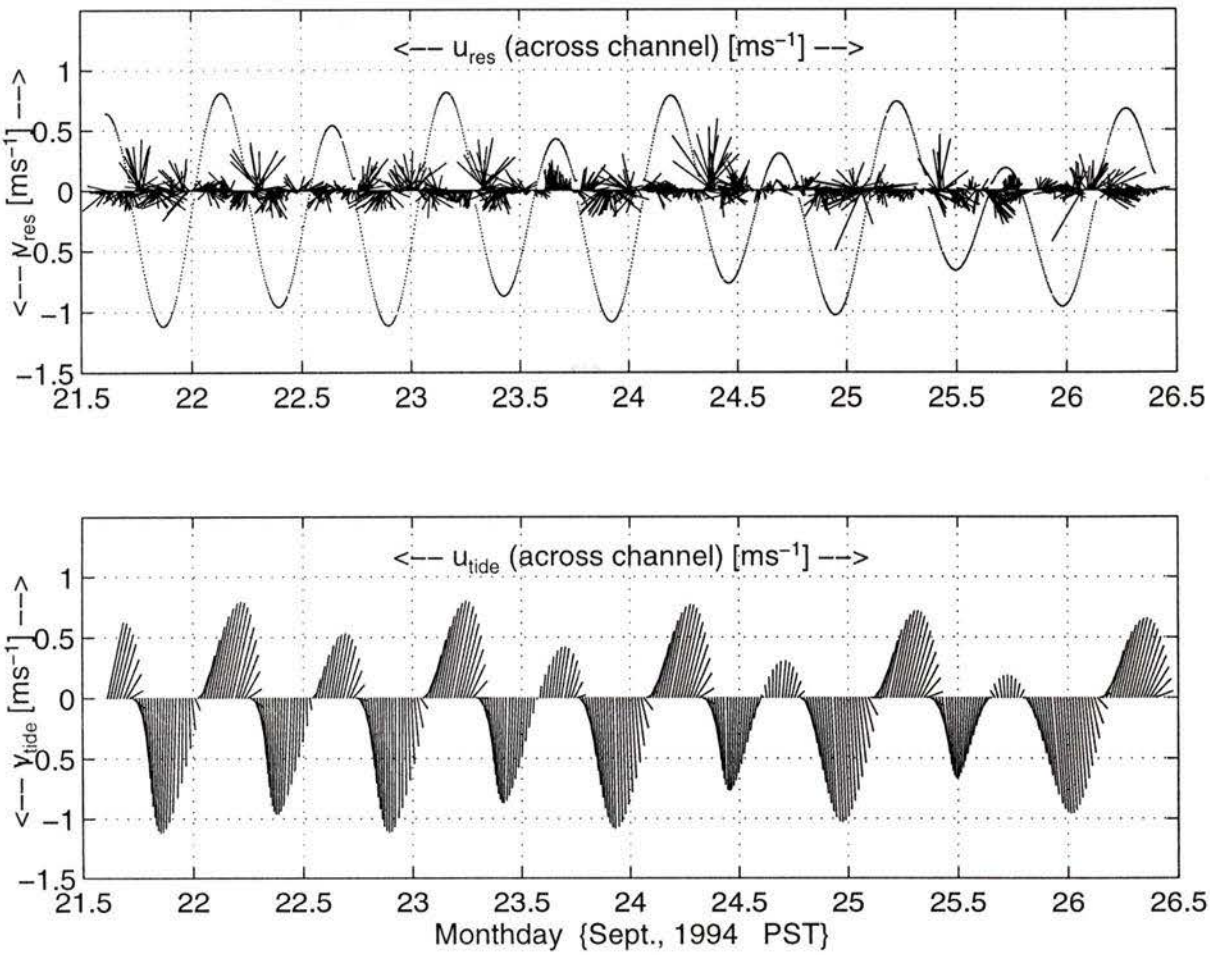

Figure 4.12: The tidal current and residual current vectors during the first deployment. Upper panel: Residual current vectors and tidal current speeds (dotted line). The residual current is rotated to the the direction of the channel, 327°. Lower panel: The tidal current vectors (only every fourth sample), also rotated to the direction of the channel, 327°.

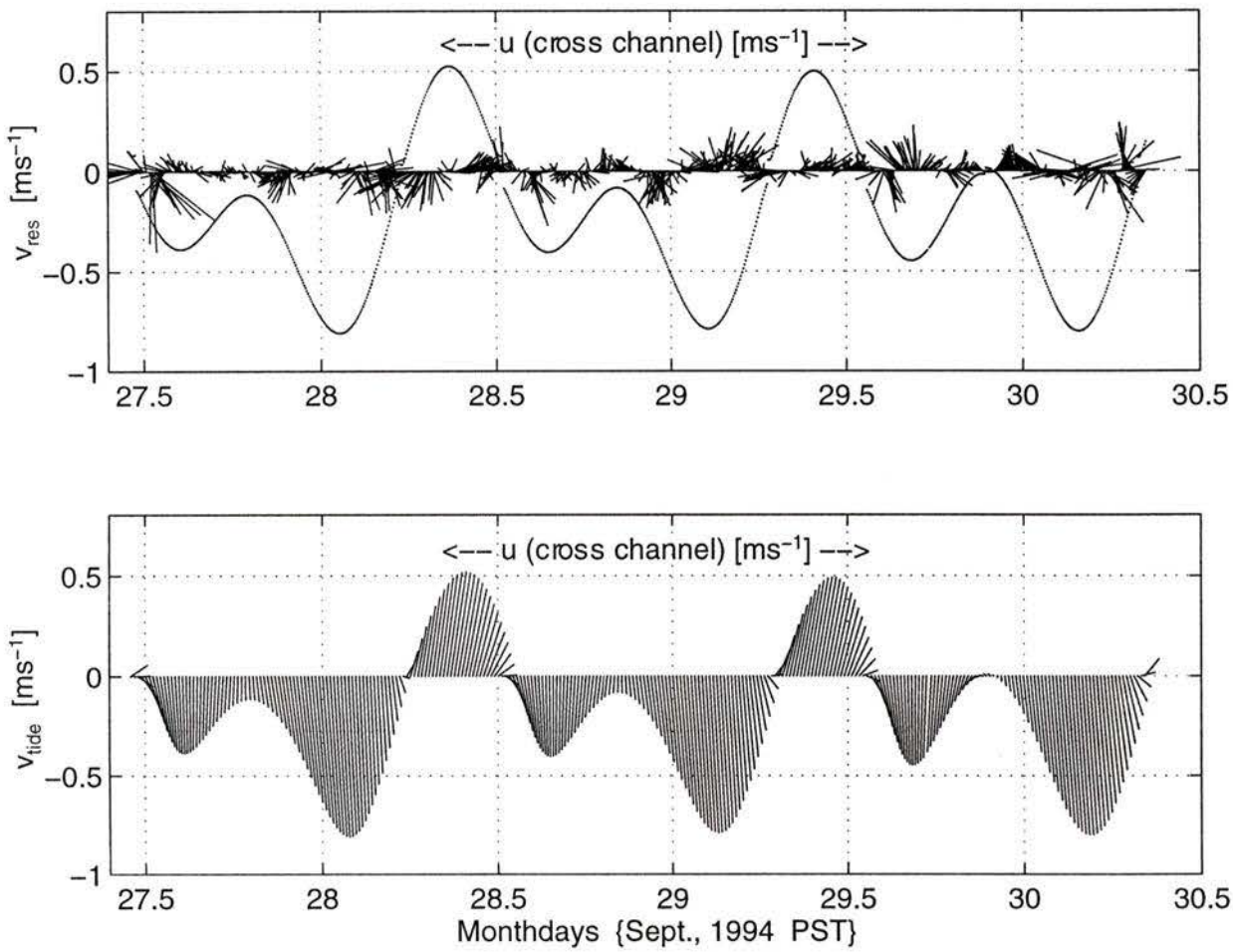

Figure 4.13: The tidal current and residual current vectors during the second deployment as in Figure 4.12. Only every third sample of the tidal current is plotted. Note that there is no current data around day 29.9 for several hours.

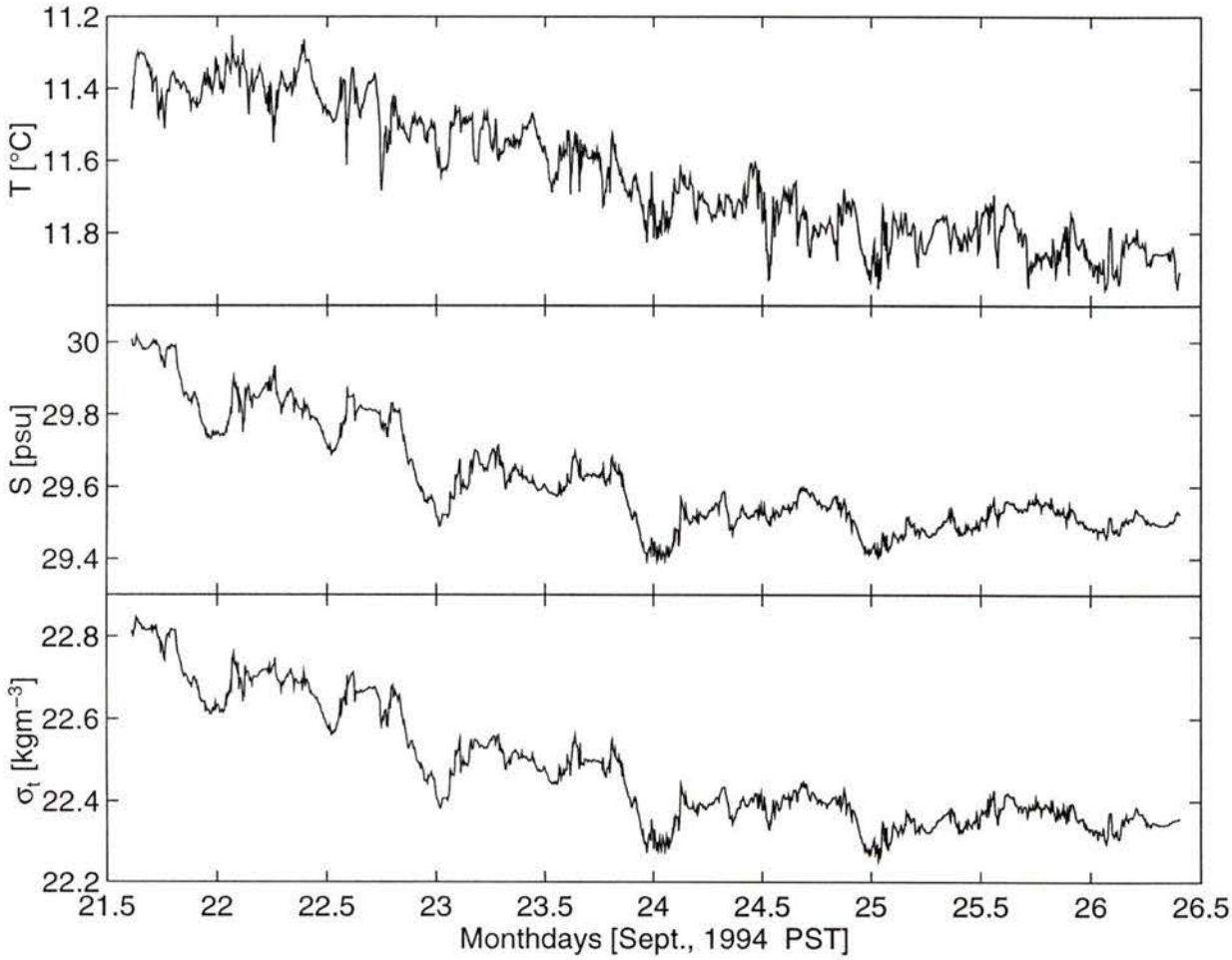

Figure 4.14: Temperature, salinity and σ_t from the Sea-Bird sensors, at mid-body, during the first deployment.

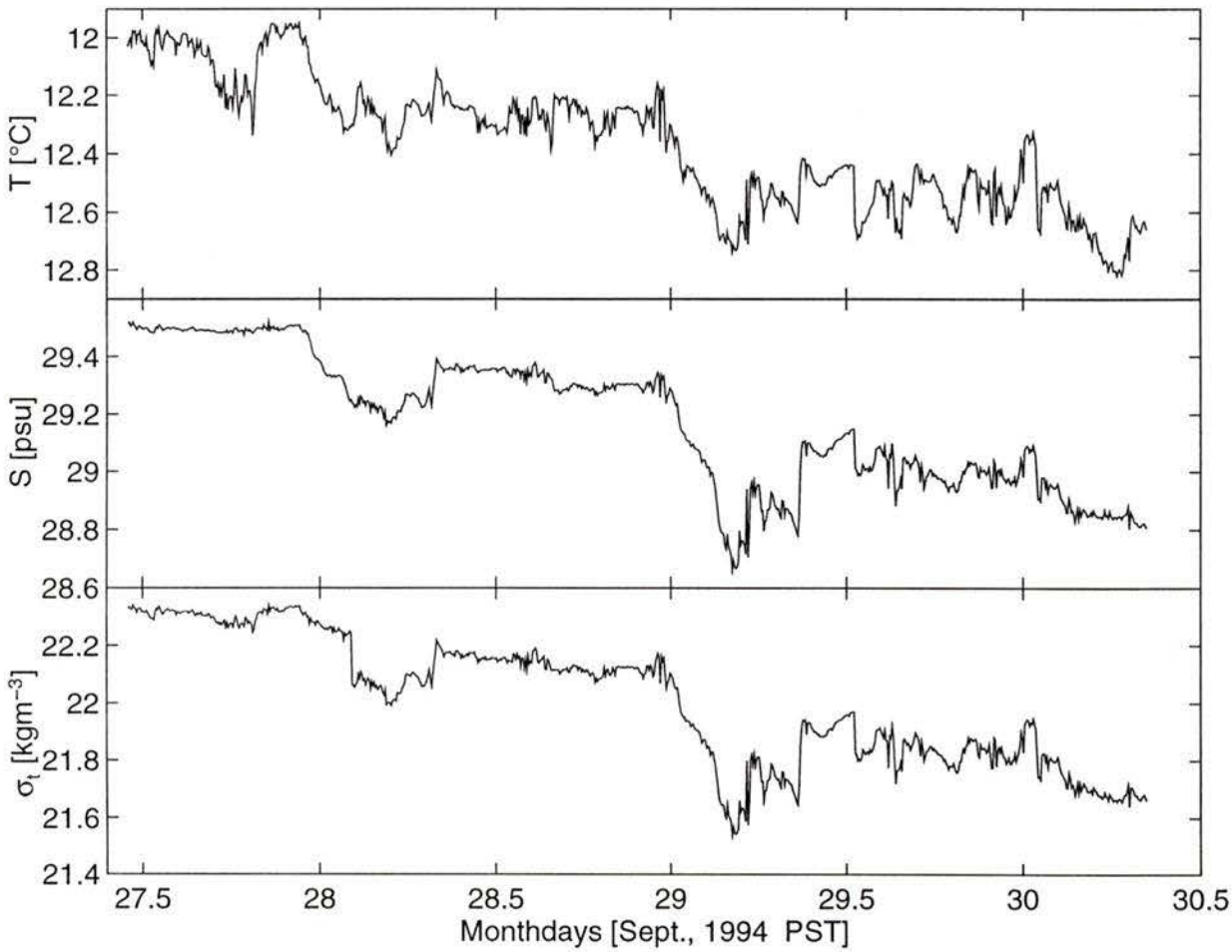

Figure 4.15: Temperature, salinity and σ_t from the Sea-Bird sensors, at mid-body, during the second deployment.

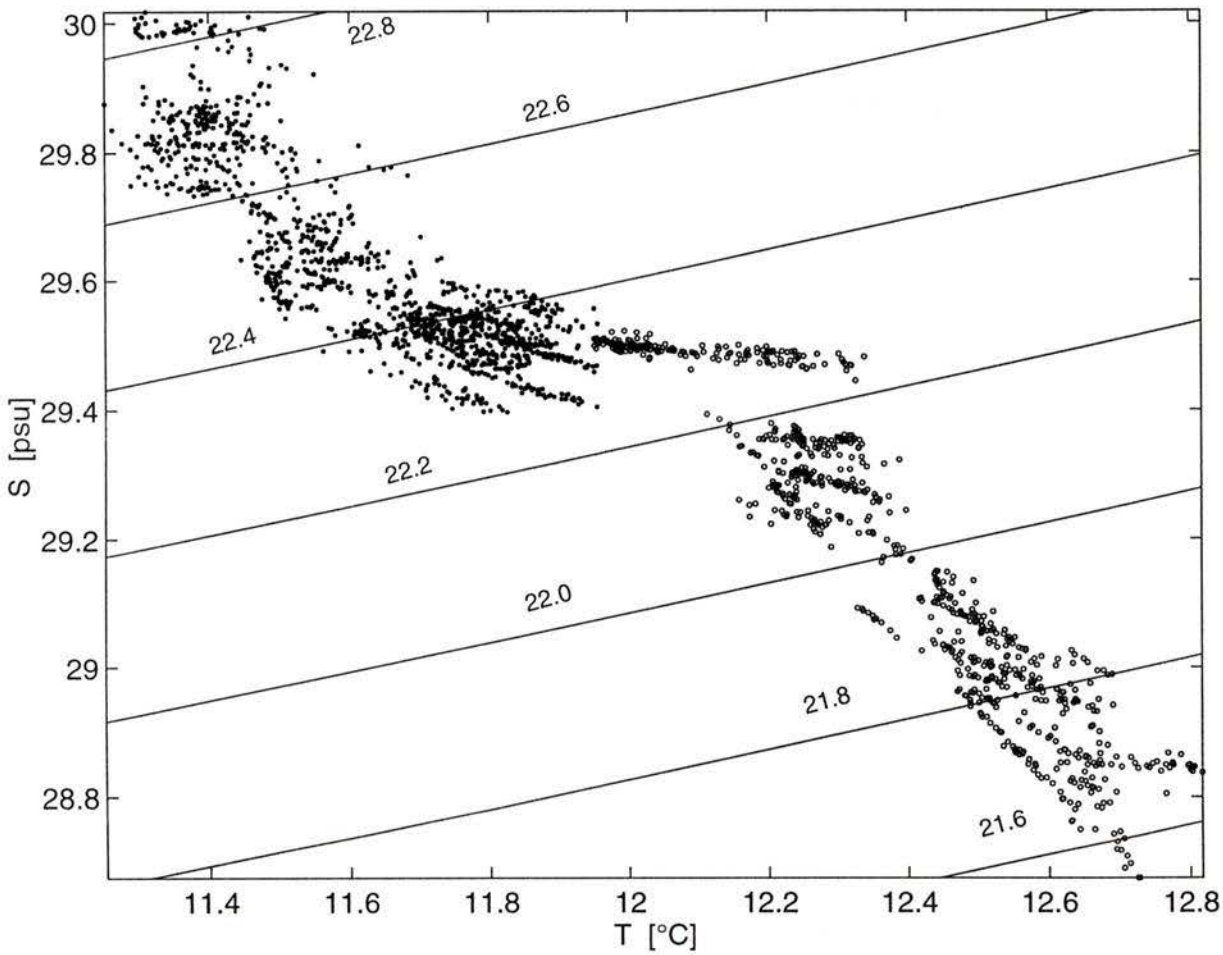

Figure 4.16: T-S relationship during the experiment. Solid (open) dots come from the first (second) deployment. A line represents a constant σ_t [kgm^{-3}].

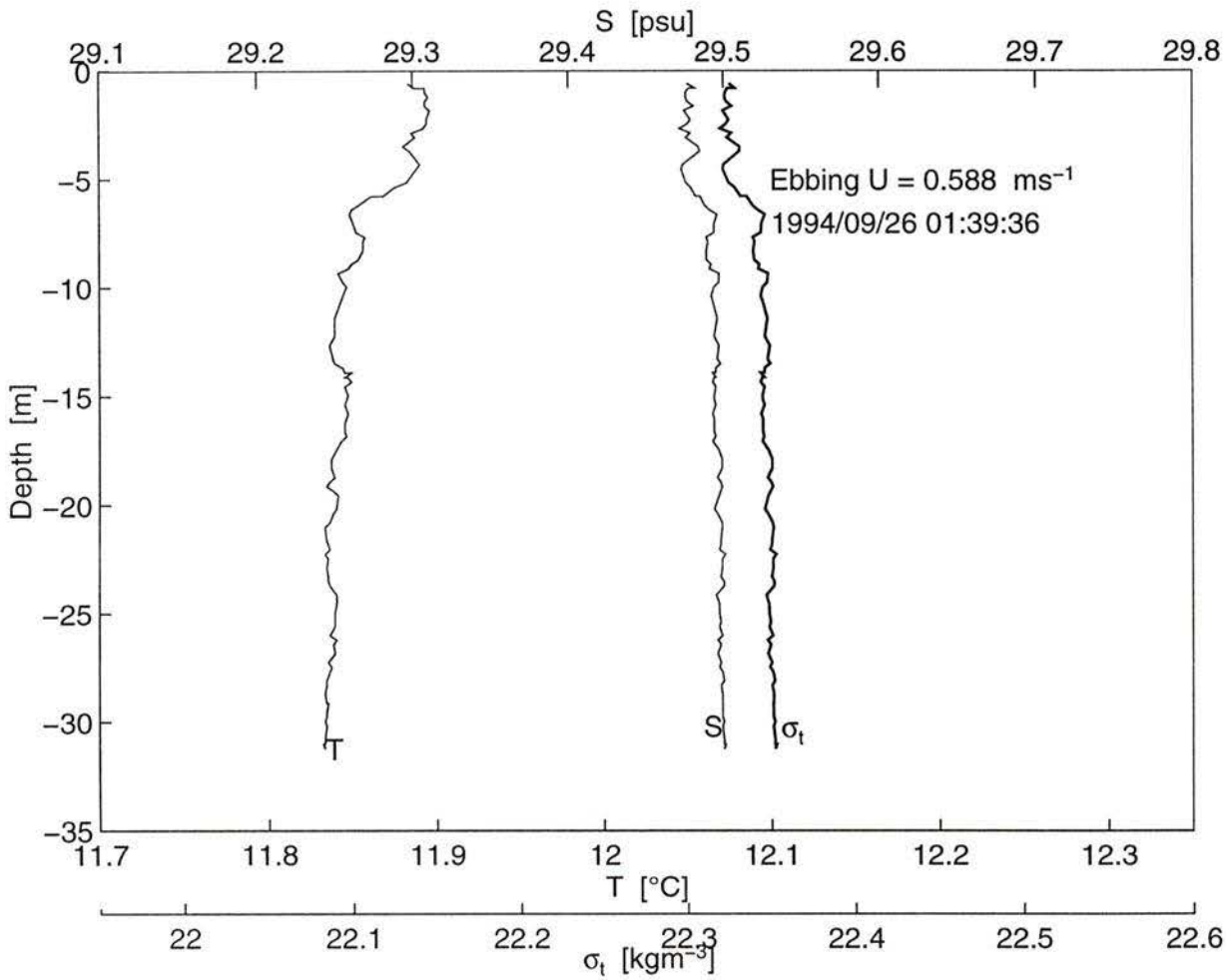

Figure 4.17: A CTD profile taken during a strong ebbing.

very near the bottom was slightly stronger. The salt tongue at 13m depth had a density much larger than in any other part of the water column. This extrema can not be produced by overturning and must have resulted from the horizontal advection of anomalously dense water. This tongue was gravitationally unstable and suggests vigorous turbulence well removed from the bottom even during weak flows.

A third CTD profile sample, taken near the turning of the tide and during an ebb (Figure 4.19), indicates strong stratification throughout the water column. The stratification was strongest near the bottom. However, there still were significant inversions indicative of turbulence, for example at 20m depth.

4.5 Stratification and shear instability at mid-depth

The Brunt-Väisälä frequency squared, N^2, was estimated from the density gradient using the data measured by the top and bottom Sea-Bird sensors. [For the Brunt-Väisälä frequency correction see Appendix A.] No tidal modulation was evident in the N^2 estimate (Figure 4.20 and 4.21). The value of N^2 was generally small during the strongest part of the ebb (the shaded areas in Figure 4.20). This pattern existed only during the morning ebb for the second deployment (the shaded areas in Figure 4.21). The distribution of N^2 values was highly skewed (Figure 4.22). Eighty-three percent of the ebb and 87% of the flood had N^2 value smaller than $4\times10^{-5}s^{-2}$. The most probable value was approximately $5\times10^{-6}s^{-2}$ while the mean was $N^2 = 2\times10^{-5}s^{-2}$. Inversions, indicated by $N^2 < 0$, occurred more frequently during the ebb than during the flood. Inversions occurred for 9.2% (6.4%) of the ebb (flood) during the first deployment and for 24.7% (11.4%) of the ebb (flood) during the second deployment (Table 4.7).

The Richardson number, Ri, was calculated using N^2 obtained with TAMI and shear with the ADCP. As mentioned in Chapter 3, N^2 was calculated with top and bottom thermometers. [The top (bottom) thermometer is 1.5 m higher (lower) than

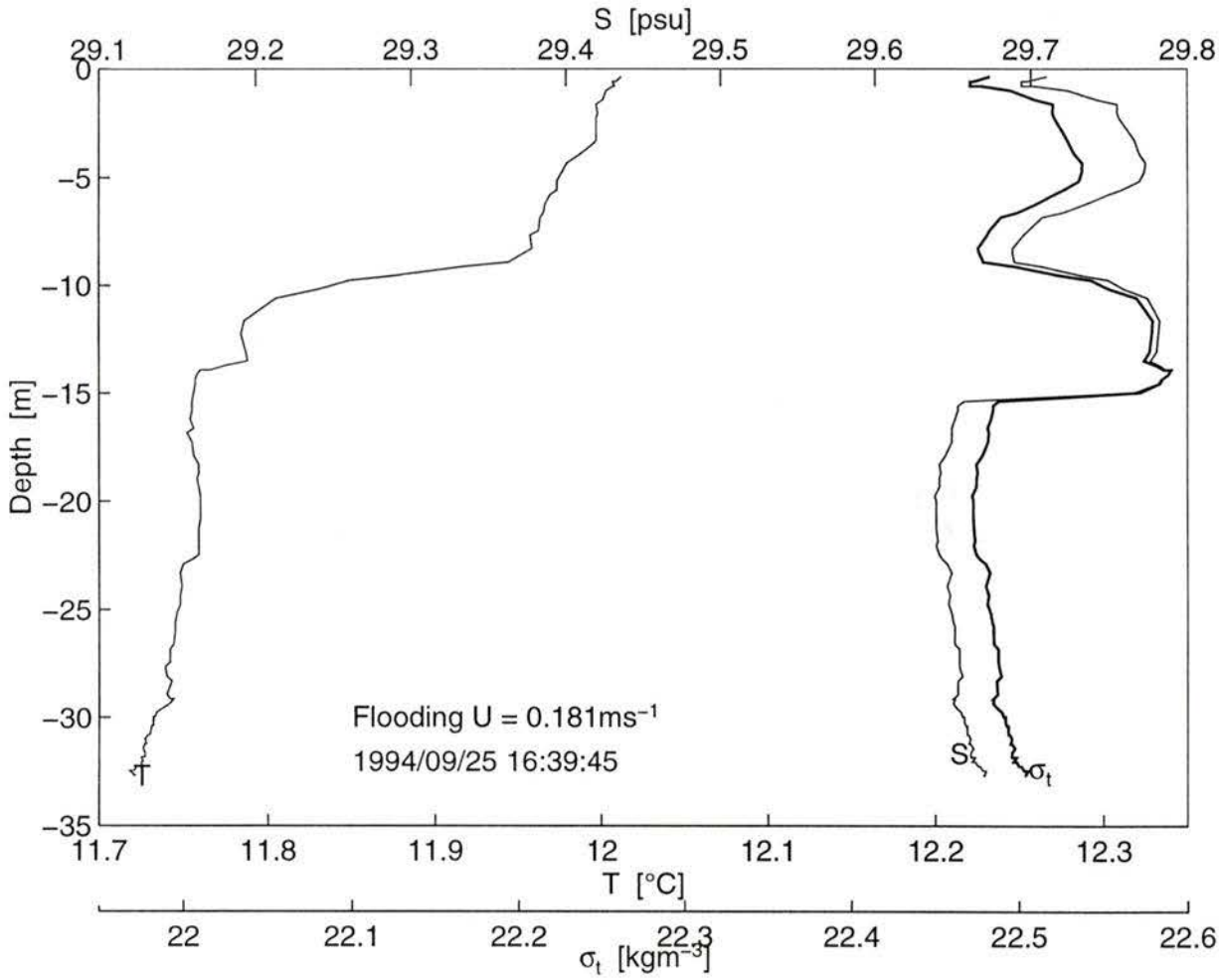

Figure 4.18: A CTD profile taken during a weak flooding and close to the turning of the tide.

the first deployment	Total	Ebb	Flood
%	7.9	9.2	6.4
the second deployment	Total	Ebb	Flood
%	21.9	24.7	11.4

Table 4.7: Percentage of inversion events ($N^2 < 0$) during the experiment. A percentage indicates that the ratio of the number of negative N^2, to the total number of N^2 observed during a specific kind of period, for example, ebb.

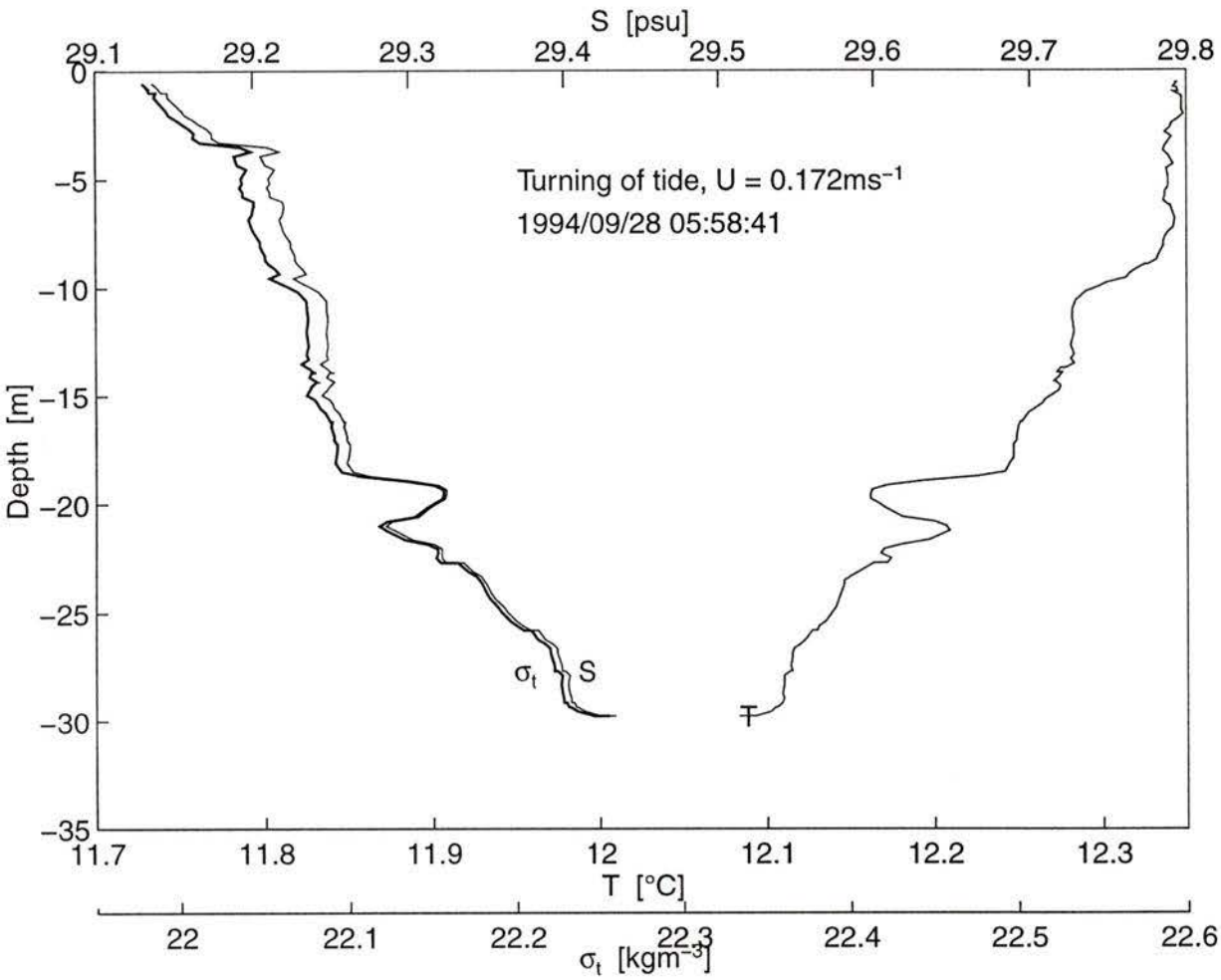

Figure 4.19: A CTD profile taken during a weak ebbing around the turning of the tide.

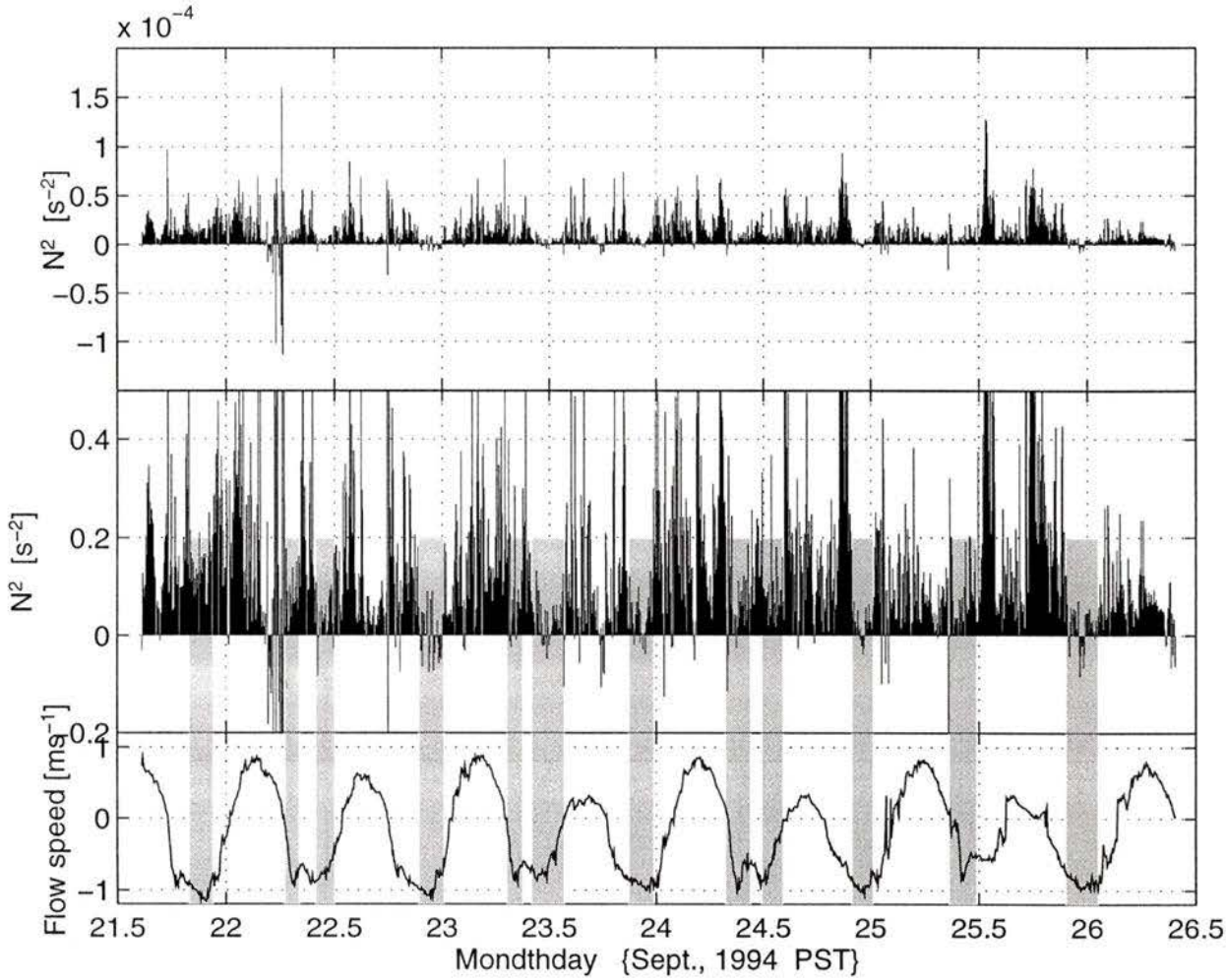

Figure 4.20: The Brunt-Väisälä frequency squared, N^2 ([s^{-2}]), during the first deployment. A negative N^2 indicates an inversion. Grey shading areas indicate the periods of strong ebbing associated with weak stratification. Upper panel: N^2 shown in the upper panel. Middle panel: A close look of N^2 in the upper panel. Lower panel: Current speed, upward (downward) direction indicates flooding (ebbing).

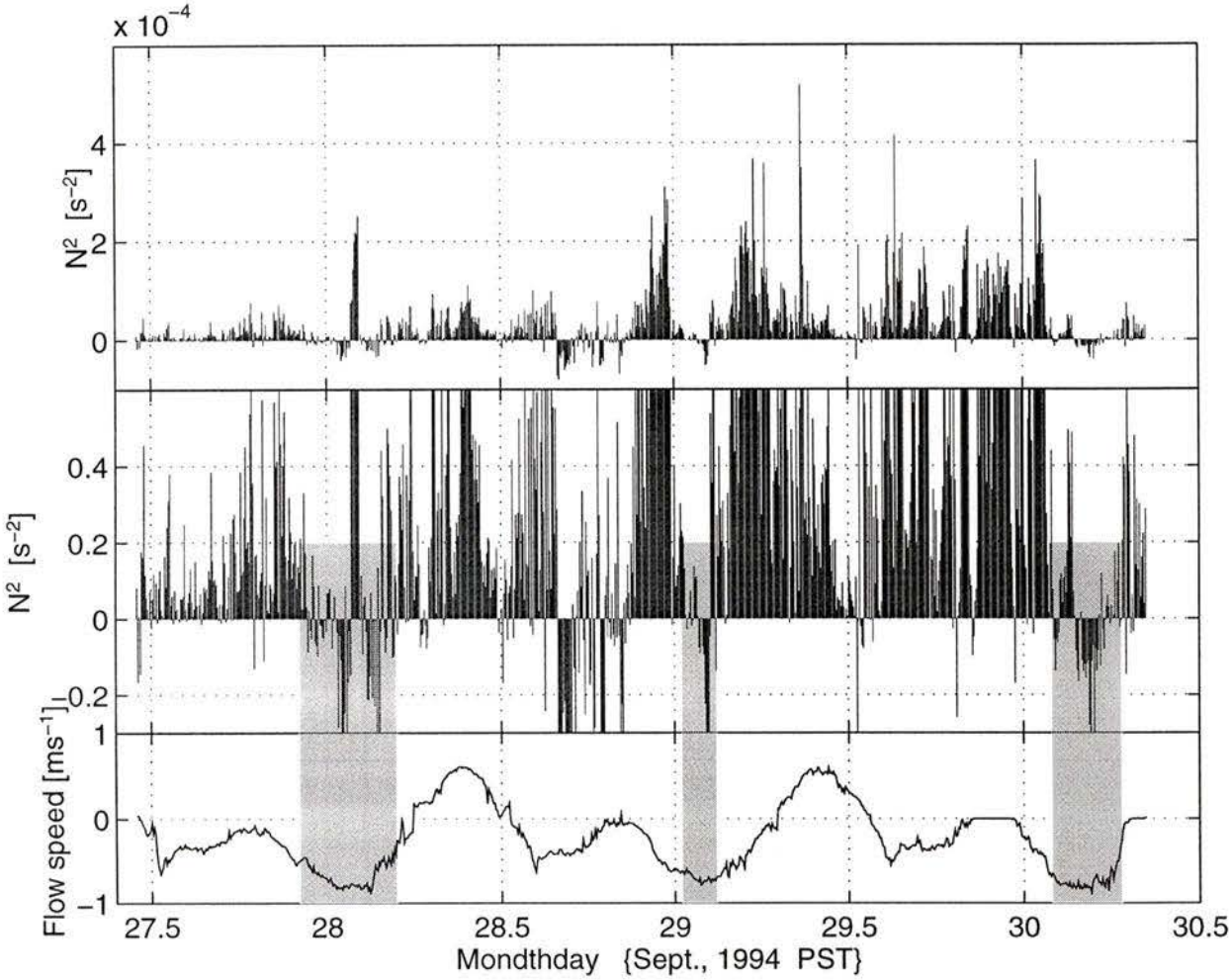

Figure 4.21: The Brunt-Väisälä frequency squared, N^2, during the second deployment as in Figure 4.20. Note that the positive peaks (about 1 hour) around day 28.1 may have resulted from fouled conductivity cell.

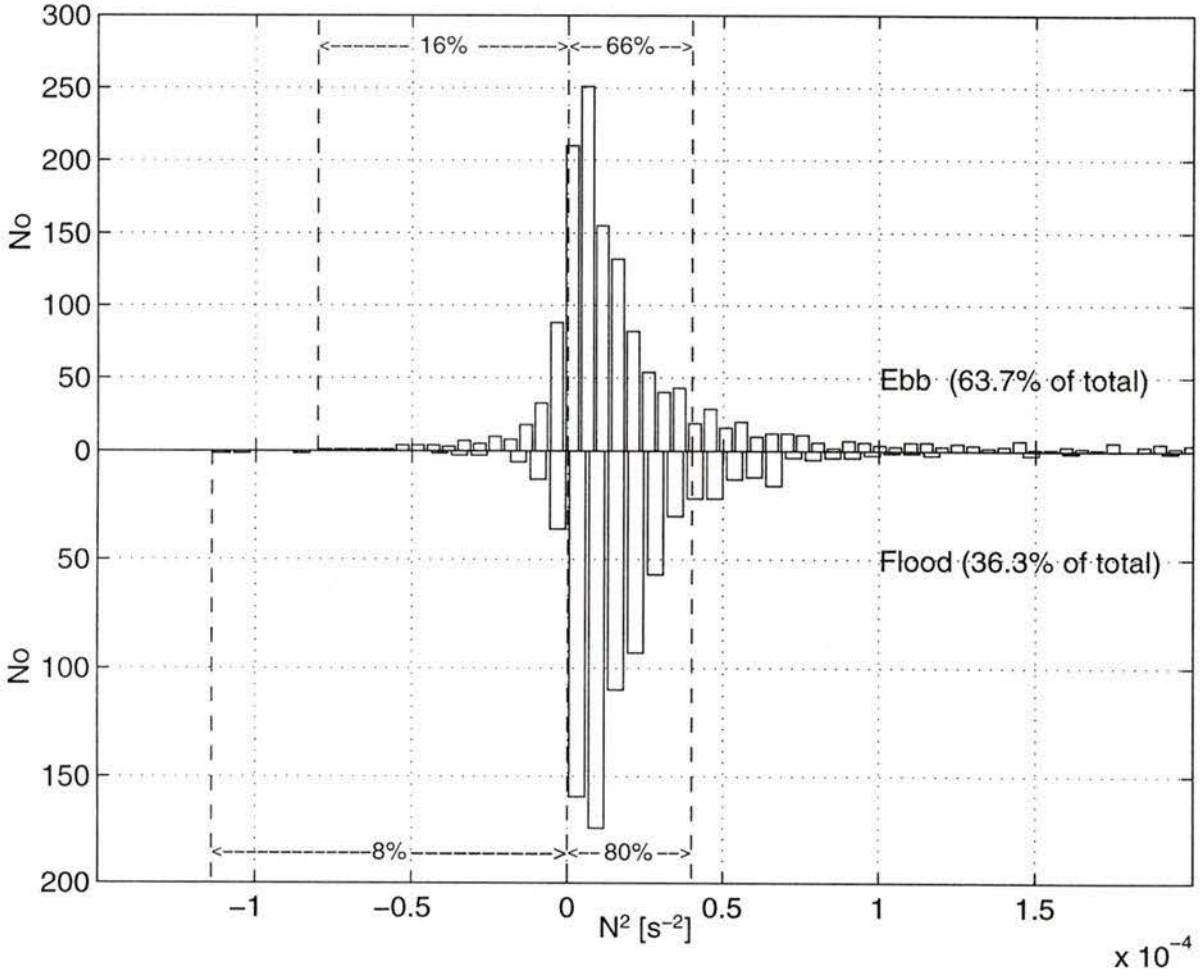

Figure 4.22: Histogram of N^2 during the ebb and the flood for the entire experiment.

the shear probes.] Shear was computed with two velocity estimates which were averaged in two 1-m bins – one is 0.5 m higher than the shear probes and the other is 0.5 m lower. The Richardson numbers were estimated for only three days (Figure 4.23) because we only have 3 days of shear estimates from ADCP at the depth of TAMI. Because neither N^2 nor the shear had a tidal modulation at 15m above the bottom, the Richardson number, Ri, also had no tidal signal. There was also no evident relationship between the current speed and Ri. Forty-seven percent of the Ri estimated were less than 1/4 during the ebb while only 26% were less than 1/4 during the flood (Figure 4.24). For these three-day data, $Ri < 0$ (determined exclusively by $N^2 < 0$) occurred more frequently during the ebb than during the flood, with 11% and 5%, respectively.

4.6 Meteorological condition

Meteorological records showed that the wind was light with typical speed of 2 ms^{-1} and occasionally gusted to 4 ms^{-1}. The surface stress due to the wind was O(0.02 Pa) if we use $\tau = \rho_A C_D U_{10}^2$, where ρ_A is density of air, $C_D = 1.3 \times 10^{-3}$ (Smith 1980) is the drag coefficient and U_{10} is the wind speed at a height of 10m, and we used the speed at 4m instead. The surface stress was much less than the bottom stress, typically 2.5 Pa (Lueck and Lu 1996). Because TAMI was at 15m above the bottom, the surface stress is unimportant compared to the bottom stress.

It was clear and sunny during the experiment. The record of air temperature showed a diurnal cycle with the highest temperature occuring around noon and the lowest temperature occuring around mid-night. The maximum temperature was 21°C and the lowest temperature was 12°C during the warm days (days 21 - 23, 27 - 30). The daily extrema were 15°C and 10°C during the cool days (days 24- 26).

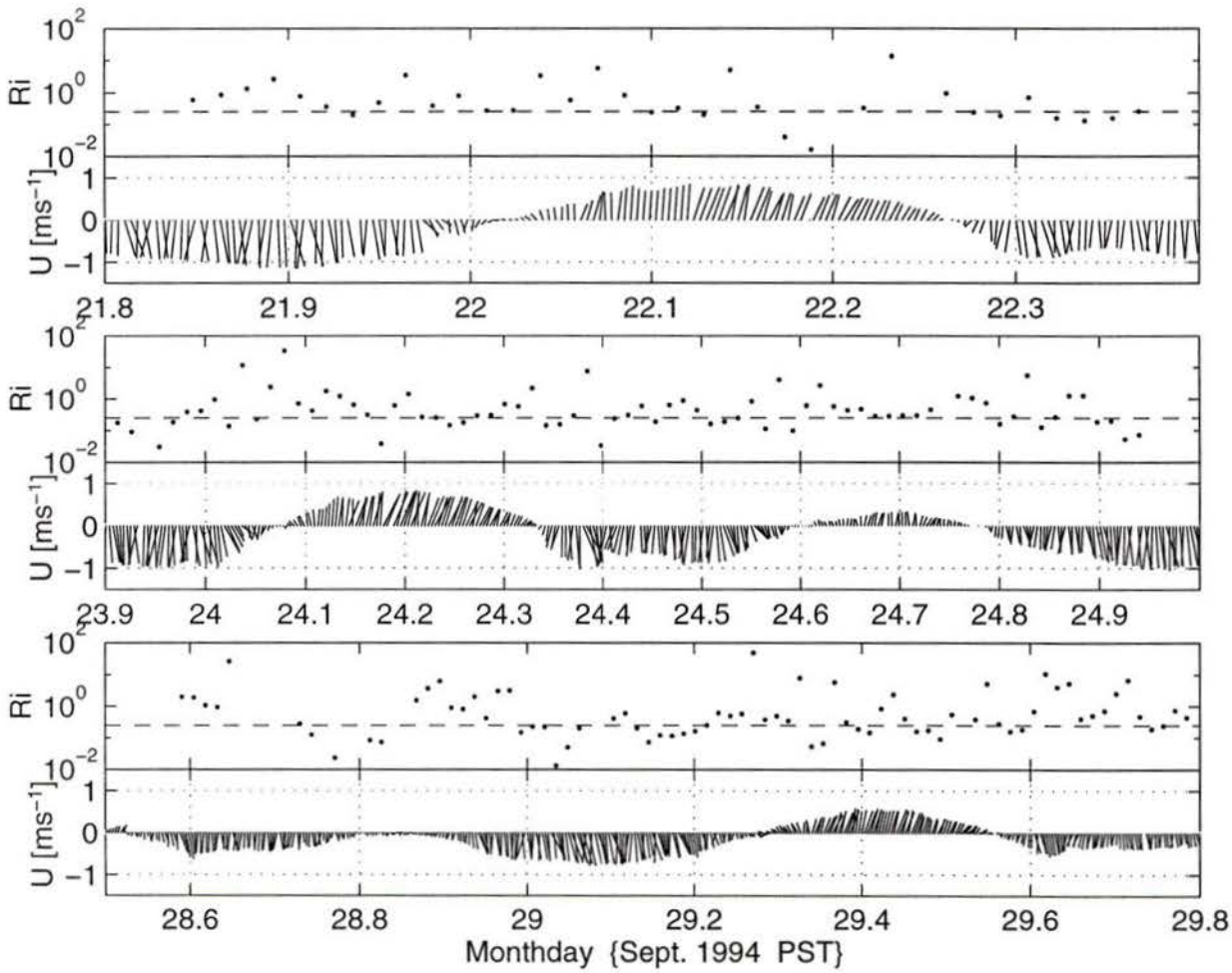

Figure 4.23: Three days of Richardson numbers calculated by using the Brunt-Väisälä frequencies squared (N^2) measured by TAMI and shears measured by the ADCP. Top panel: Days 21.8 - 22.4; Middle panel: Days 23.9 - 25.0; Bottom panel: Days 28.6 - 29.8. Note that blanks indicate negative Ri caused by negative N^2.

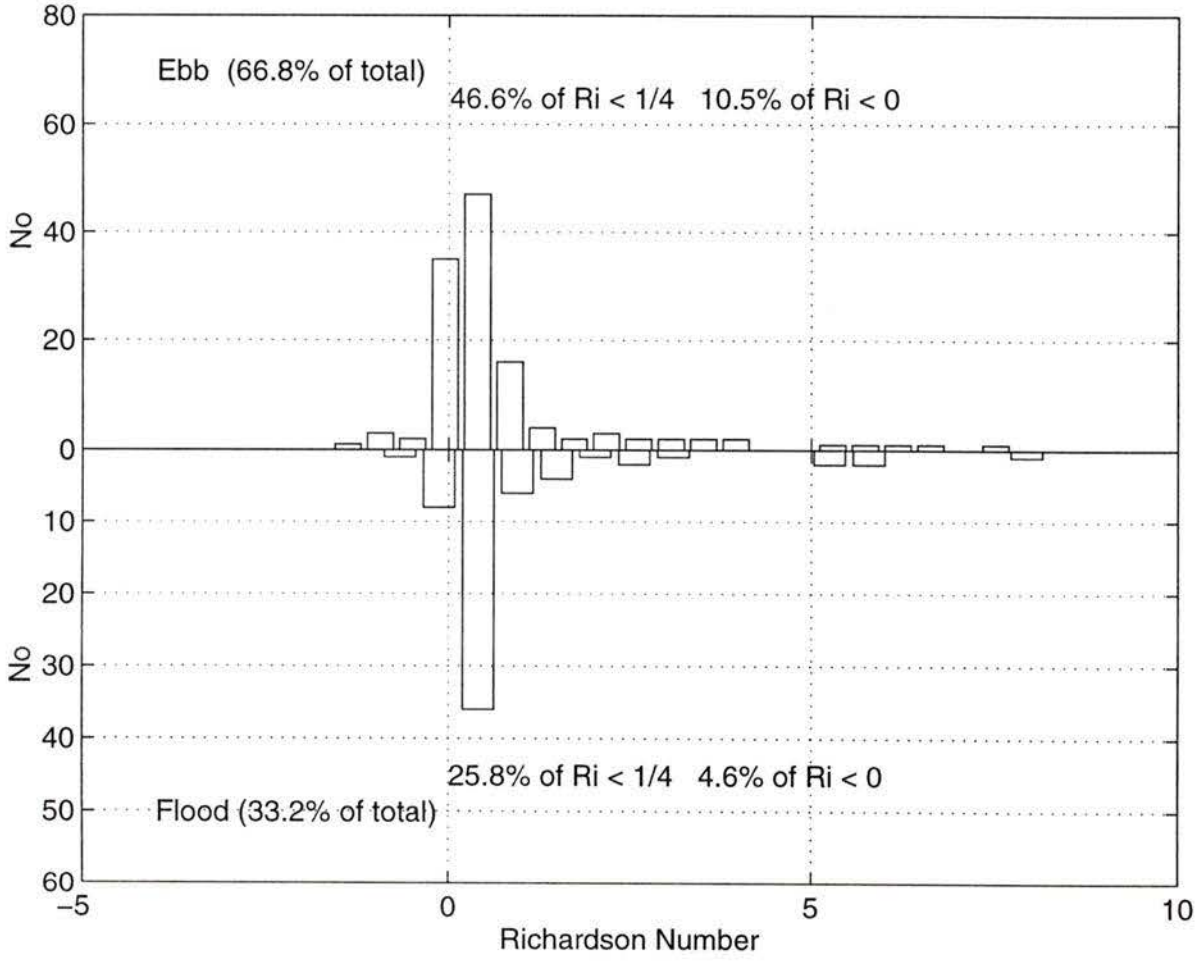

Figure 4.24: Histogram of Richardson number, Ri, in Figure 4.23. For the ebb, only 4 samples of Ri are larger than 10 (the maximum is 48) and 2 samples of Ri are less than -5 (the minimum is -41). For the flood, just 2 samples of Ri are larger than 10 and the maximum is 107.

Chapter 5

Microstructure shear and acceleration

As mentioned in Chapter 2, the vibration of the instrument is expected to be stronger in Cordova Channel than that in the open ocean. However, the signal is also stronger than that in the open ocean. In this Chapter, I examine the time series to show that the measured shear was not contaminated by the body vibration.

5.1 Time series of shears and accelerations

Every 6 hours we have a 128 second long sample of unprocessed data for all channels in addition to the processed data. Here I present a typically unprocessed samples. The time series of shears ($\partial v/\partial x$ and $\partial w/\partial x$) taken during a current of 0.79m s^{-1} are shown in Figure 5.25. For this 128 second interval, the distance which water traveled is equivalent to 100m. The fluctuation of the measured shear with full bandwidth are large and intermittent, and this characteristic is not significantly changed by a low-pass filter set to 16Hz (20cpm). The choice of 16Hz will be justified in section 5.2.

The vibration of the vehicle is detected with tri-orthogonal accelerometers. The signal produced by an accelerometer is composed of two parts (Moum and Lueck 1985; Osborn and Lueck 1985a; Lueck *et al.* 1996). The output at low frequencies is due to gravity and at high frequencies comes from inertial acceleration. The apparent shear signals due to body vibration are a_z/U and a_y/U for $\partial w/\partial x$ and $\partial v/\partial x$, respectively (Osborn and Lueck 1985a; Lueck *et al.* 1996), where a_y is the horizontal cross-stream acceleration and a_z the vertical acceleration. The "fuzz" on the full-bandwidth

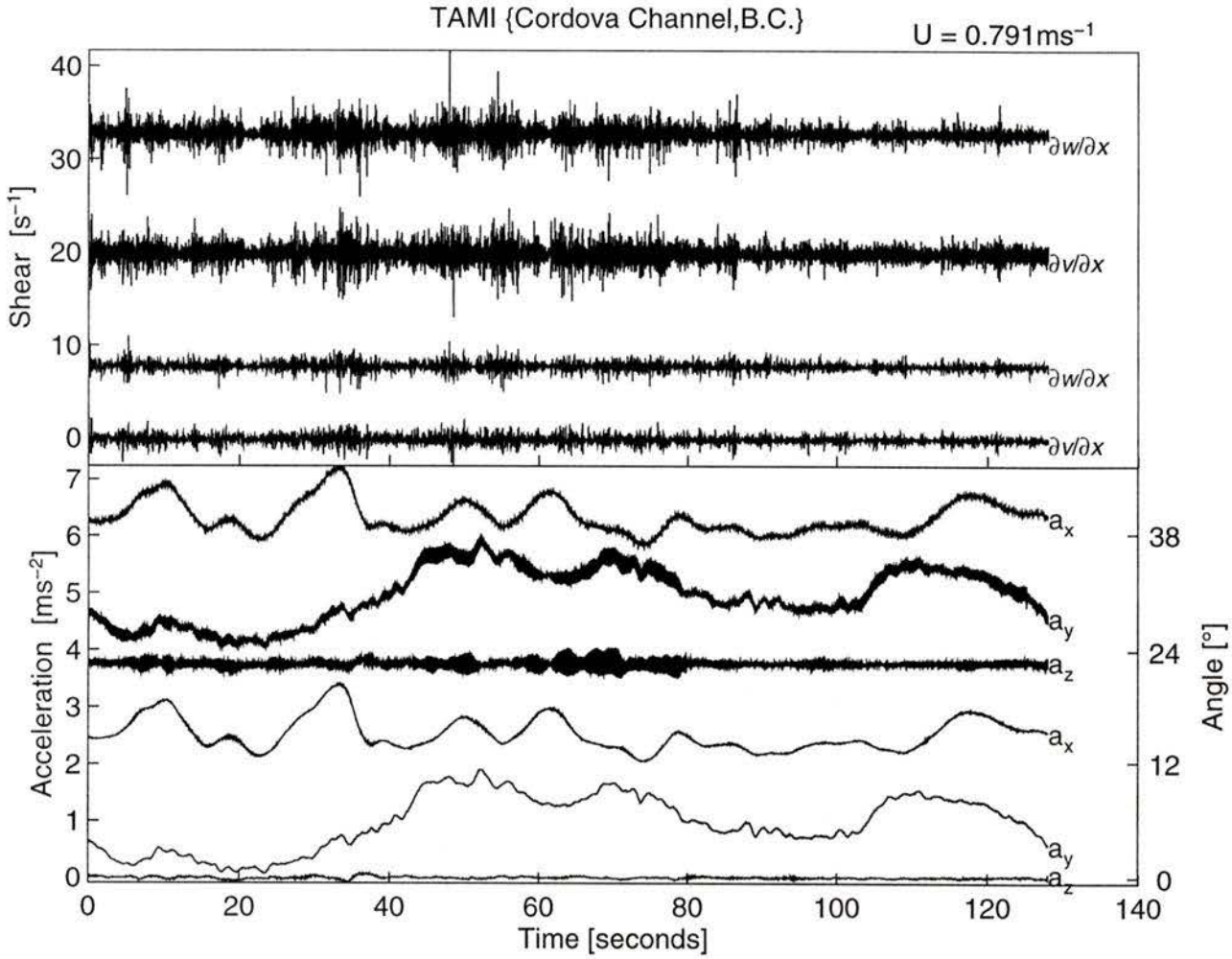

Figure 5.25: The shear and acceleration measured in a current of 0.79m s^{-1}. Upper panel: The shears with full bandwidth (*two upper lines*) and the shears low-pass filtered (*two lower lines*) starting at 16Hz (20cpm). The rates of dissipation, ϵ_w and ϵ_v, are 1.56×10^{-5}W kg^{-1} and 1.52×10^{-5}W kg^{-1}, respectively, estimated with the inertial-subrange technique (see Appendix C). Lower panel: The full-bandwidth accelerations (*three upper lines*), the low-pass filtered accelerations (*three lower lines*), using the same filter as for the shears. The labels on the axis at right represent the angle of pitch and roll. The offsets for these six lines from bottom to top are 0, 1.2, 3, 4, 5.2 and 6.8 m s^{-2}. For the filtered pitch and the filtered roll, the offsets are equivalent to 18° and 7°, respectively.

acceleration data represents the high-frequency inertial acceleration while the low-frequency variations (with time scale longer than ~1 second) of a_x and a_y represent pitch and roll, respectively. When the accelerometer signals are convolved by the same low-pass filter (Figure 5.25) used for the shear signals, there is no correlation between the variances of the filtered accelerations and the filtered shears. The signal magnitudes are very different. The filtered accelerations are typically 0.03m s^{-2} for a_z and a_y, equivalent to 0.05s^{-1} for a/U, and this is 60 times smaller than the measured shears. The signals produced by the gravity are

$$[a_x, a_y] = g[\sin(\alpha), \sin(\beta)] \tag{5.53}$$

where α is the pitch angle (positive with nose up) and β is the roll angle (positive port down). The typical peak-to-peak pitch is 5° with a period of ~10 seconds and the roll is less than 5° with a period of ~30 seconds. A peak-to-peak of roll of 0.5° and ~2 second period is also evident and this signal may be either roll or inertial acceleration.

The further examination of another 30 samples of unprocessed data taken during current speeds ranging from 0.3m s^{-1} to 1.1m s^{-1} also indicates that the measured shears are not contaminated by vibrations. In these samples, the magnitude of the measured shears is usually at least 20 times larger than the contribution from vibrations. Therefore, the measured shears are real environmental signals.

5.2 Spectra of shears and accelerations

By comparing the spectra of the measured shears ($\phi_{\partial w/\partial x}$ and $\phi_{\partial v/\partial x}$) against the spectra of the shears induced by the vibration of the instrument (scaled acceleration spectra – ϕ_{a_z}/U^2 and ϕ_{a_y}/U^2), we can determine which, if any, frequencies are contaminated.

A typical shear spectrum (Figure 7b of Lueck *et al.* 1996) rises at small wavenumbers with a slope of 1/3 to its spectral peak and then falls quickly at large wavenumbers. Electronic noise and vibration usually appear as a rise of the spectrum at very high wavenumbers. Spectra (Figure 5.26) are estimated with two methods – one using the unprocessed times series and the other using the spectra processed (*in situ*) by the DSP of the instrument. The spectra of the shears measured in Cordova Channel rise from small wavenumber up to about 20cpm, reaching a spectral maximum, and then fall at large wavenumbers. These spectra fall even more quickly than those of Lueck *et al.* (1996) at high wavenumbers because (1) the spectra from Cordova Channel reach larger wavenumbers, (2) the electronic noise of the instrument was 10^4 times smaller than in Lueck *et al.* (1996), and (3) the influence of the anti-aliasing low-pass filter (at 43Hz) is more pronounced because of (1).

The scaled acceleration spectra ($\phi_{a_{(y,z)}}/U^2$) fall below the shear spectra from 0.2cpm (for $\partial w/\partial x$) and 0.8cpm (for $\partial v/\partial x$) to 21cpm. Within this range, the separations between the shear spectra and the scaled acceleration spectra are very clear. A peak at 4cpm (3Hz) in the scaled acceleration spectra has no influence on the spectra of the measured shears. The vibration at this frequency is due to the mast (Lueck *et al.* 1996). The spectra of the measured shears are contaminated by vibrations starting from 21cpm (17Hz). The vibration at this frequency is also associated with the mast (Lueck 1996, personal communication). The spectral peaks of the measured accelerations, at 23, 43, 47, 64, 65 and 70cpm, contaminate the measured shears. The scaled acceleration spectra rise above the spectra of the measured shears at small wavenumbers ($\leq$ 0.4cpm). However, the output of the accelerometers in this range is due to pitch and roll which has negligible affect on the measured shears (Moum and Lueck 1985).

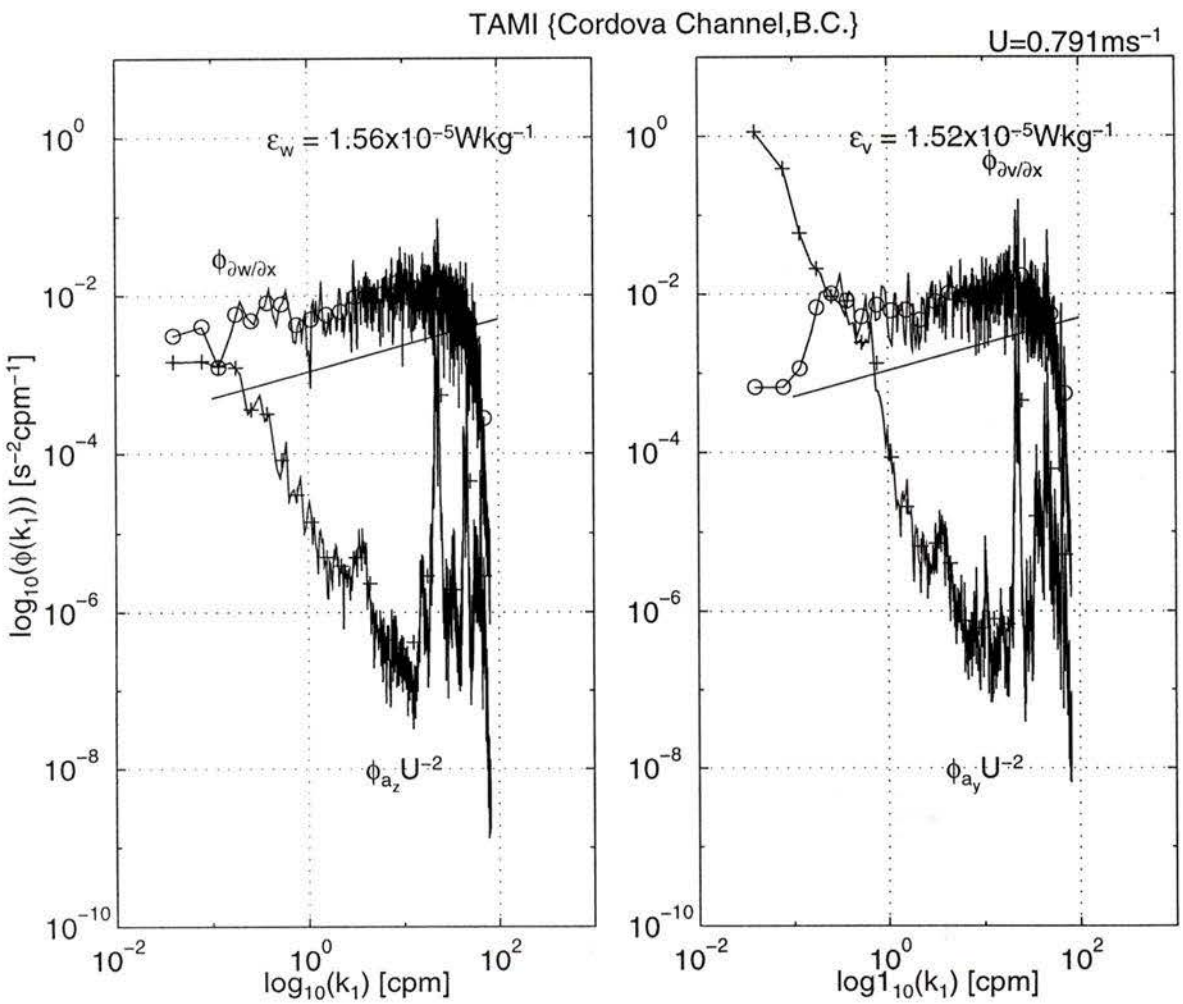

Figure 5.26: The spectra of the time series in Figure 5.25. The curves denote the spectra computed from the time series and the symbols represent the spectra calculated *in situ* by the DSP on TAMI. The upper curve in each panel is the shear spectrum and the lower curve is the acceleration spectrum. The straight lines indicate 1/3 slope. Left panel: Spectra of $\partial w/\partial x$ ($\phi_{\partial w/\partial x}$) and scaled vertical acceleration (ϕ_{a_z}/U^2). [ϵ_w = 1.56×10^{-5}W kg^{-1}.] Right panel: Spectra of $\partial v/\partial x$ ($\phi_{\partial v/\partial x}$) and scaled lateral acceleration (ϕ_{a_y}/U^2). [ϵ_v = 1.52×10^{-5}W kg^{-1}.]

Chapter 6

The inertial subrange

In this chapter, I will examine the characteristics of the velocity and temperature spectra, including (1) the slope of the spectra in the inertial-subrange, (2) the width of the inertial and inertial-convection subranges and (3) the local isotropy of the velocity spectra. All three issues bear on whether the inertial-subrange technique can be used to estimate the rate of dissipation of TKE.

6.1 Velocity

The velocity spectra used in this chapter are converted from the shear spectra. These spectra have been corrected for the spectral resolution of the shear probe (Ninnis 1984; see Appendix B) and for small deviations of the differentiator gains. The gain of the differentiator was calibrated with a spectrum analyzer to an accuracy of $\pm 1/2\%$ in amplitude. Therefore, the spectral slope over one decade of wavenumber can be determined to be approximately $\pm 1\%$, and $1/2\%$ over two decades. The spectra that will be described are selected by using criteria similar to those used for the dissipation estimates in Lueck *et al.* (1996). These criteria are (1) the maximum and minimum of output of the analog-to-digital converter do not exceed $\pm 2{,}000$ (no data saturation) [There are more than 96% of all spectra within this range, except the spectra from only one of two probes for measuring v with a slightly smaller percentage, 90%.] (2) flows are larger than 0.15m s^{-1}, (3) the spectrum is free from the contamination by body motion, (4) the rms angle of attack is less than 5° (the shear probe response is fairly linear), and (5) rotation speed of the instrument is less than 3° per minute

(steady orientation).

Individual velocity spectra generally have well-defined -5/3 slopes over 2 decades of wavenumber regardless of whether the effect of stratification, which is characterized by the buoyancy Reynolds number (R_B), is high or low (Figure 6.27). Each spectrum comes from data collected at a unique interval. There is very little difference between spectra from data taken simultaneously. Gargett *et al.* (1984) used the criterion, $I = R_B^{3/4}$ in (2.38), to classify the effect of buoyancy on the velocity spectra. For $I \geq 3000$, their velocity spectra – one stream-wise and two cross-stream spectra – all had well-defined -5/3 slopes. However, for $I < 900$, only the stream-wise velocity spectrum had a well-defined -5/3 slope but the two cross-stream velocity spectra were below the -5/3 slope at low wavenumbers. Gargett *et al.* suggested that the change of slope of the cross-stream spectra was due to stratification. We find that the cross-stream velocity spectra in strong stratification ($I \leq 900$) have a well defined -5/3 slope down to wavenumbers as small as those examined by Gargett *et al.* (1984).

Because all of our individual velocity spectra have well-defined -5/3 slopes, we have an opportunity to examine the statistics of this characteristic (-5/3 slope) in the inertial-subrange. The velocity spectra are scaled into non-dimensional form using (2.33). With the scaling of (2.33) a "perfect" spectrum would equal 1 for all wavenumbers and, by flattening the spectrum, small deviations of the slope are greatly emphasized. In this scaling, the dissipation, ϵ, is estimated first, using the inertial-subrange technique (see Appendix C). The range of a spectrum selected as the inertial-subrange is determined only by one criterion – we reject those spectral points contaminated by vibration. Because the portion of the spectra most likely to be contaminated by vibration lie below 1cpm (Figure 6.28 and 6.29), the range chosen for the inertial-subrange is generally from approximately 1cpm to 20cpm. The spectra at low wavenumbers were frequently affected by body motion. For the vertical spectra, these motions may be caused by body vibrations or internal wave motions.

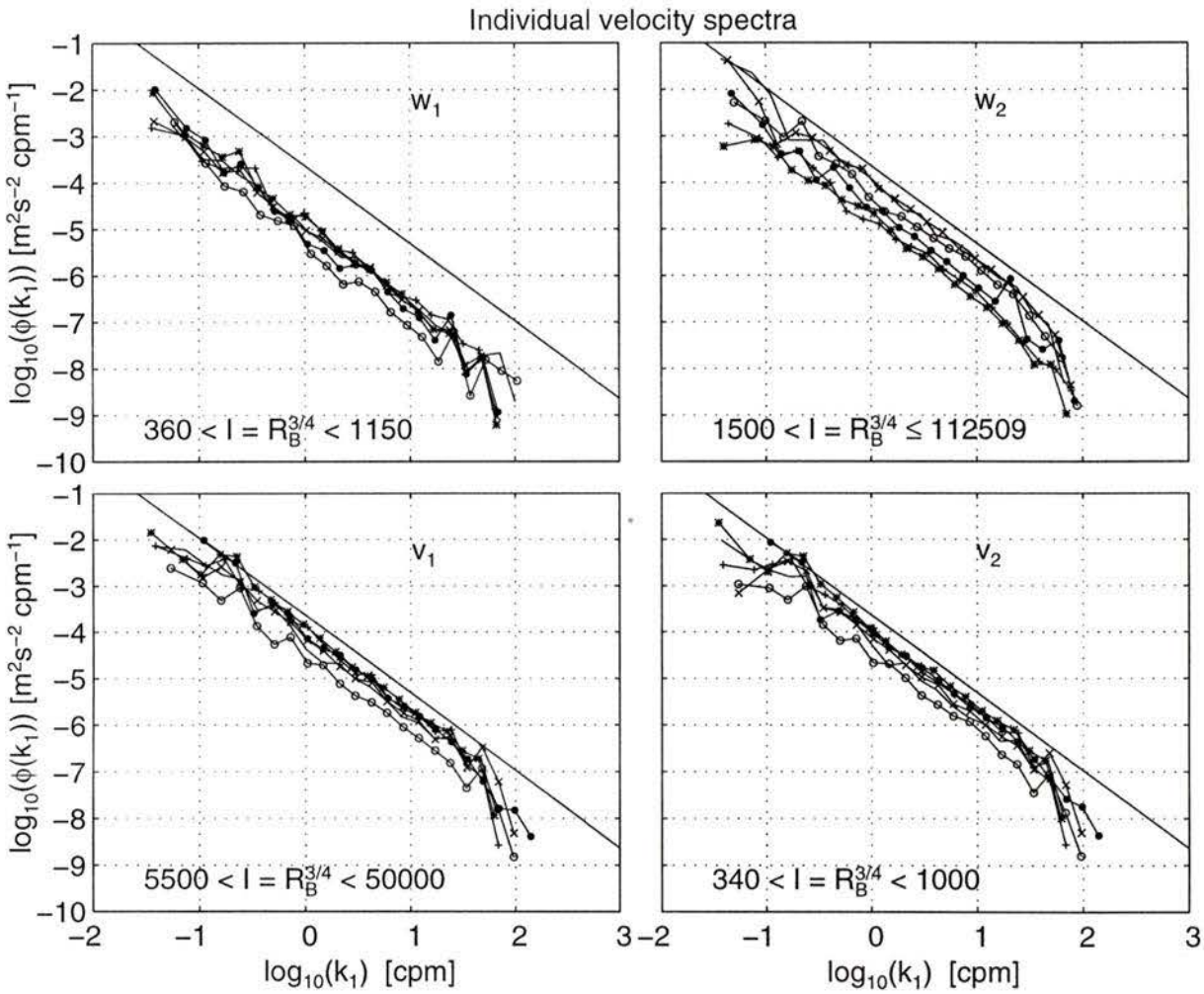

Figure 6.27: Twenty-four individual velocity spectra from the four shear probes, all for different times. In each panel, there are 6 spectra from a probe. Of the 6 spectra in a panel, the first 5 spectra are denoted by five symbols combining 5 curves together and the last spectrum by only a curve. The straight lines indicate -5/3 slopes. R_B is the buoyancy Reynolds number and $I = R_B^{3/4}$ in (2.38).

For the horizontal component, the spectra at low wavenumbers are also affected by changes of the current direction. Because the instrument is free to rotate into the direction of flow, this effect is equivalent to a high pass-filter and is evident in the roll-off below 0.2cpm (Figure 6.29).

The dissipations estimated from the spectra of v and w taken simultaneously are statistically identical (Figure B.56). Also, the dissipations estimated from the spectra of w_1 and w_2 as well as of v_1 and v_2 taken simultaneously are statistically identical (Figure B.56).

The non-dimensional velocity spectra in the inertial-subrange are shown in Figure 6.30 and 6.31. Only the spectra from two of the four shear probes – one for ϕ_{w_1} (866 spectra) and the other for ϕ_{v_2} (793 spectra) – are shown. The spectra from the other two probes are nearly identical to their counterparts. In Figure 6.30 and 6.31, at least 98% of the non-dimensional spectral points fall within $\pm 1/4$ decade of unity. A single slope fitted by least squares to the non-dimensional spectra from each probe (Table 6.8) are used to examine the deviation from the ideal spectral slope of -5/3. The slope of the non-dimensional ϕ_{w_1} spectrum (Figure 6.30) is -0.007 and its 95% confidence interval is [-0.01, -0.00], estimated by using the Bootstrap method (Efron and Gong 1982). This 95% confidence interval suggests that the slope of the spectrum of w_1 is within a range of -5/3$\pm$0.01 because $\pm$0.01 is the limit imposed by our ability to calibrate the transfer function of the differentiator. The slope of all 1740 non-dimensional spectra from the vertical component (Table 6.8) is -0.000 and the 95% confidence intervals also indicates that the slope is within -5/3$\pm$0.01. Further, the slopes for the non-dimensional spectra from the horizontal component is -0.011 only for ϕ_{v_2} (793 spectra) (Figure 6.31) and is -0.006 for all 1538 non-dimensional ϕ_v. Again, the slope of the horizontal velocity spectrum is within -5/3$\pm$0.01. Finally, combining all non-dimensional spectra (3278 samples) from all four shear probes together, the slope and its 95% confidence intervals (also Table 6.8) is within -5/3$\pm$0.01.

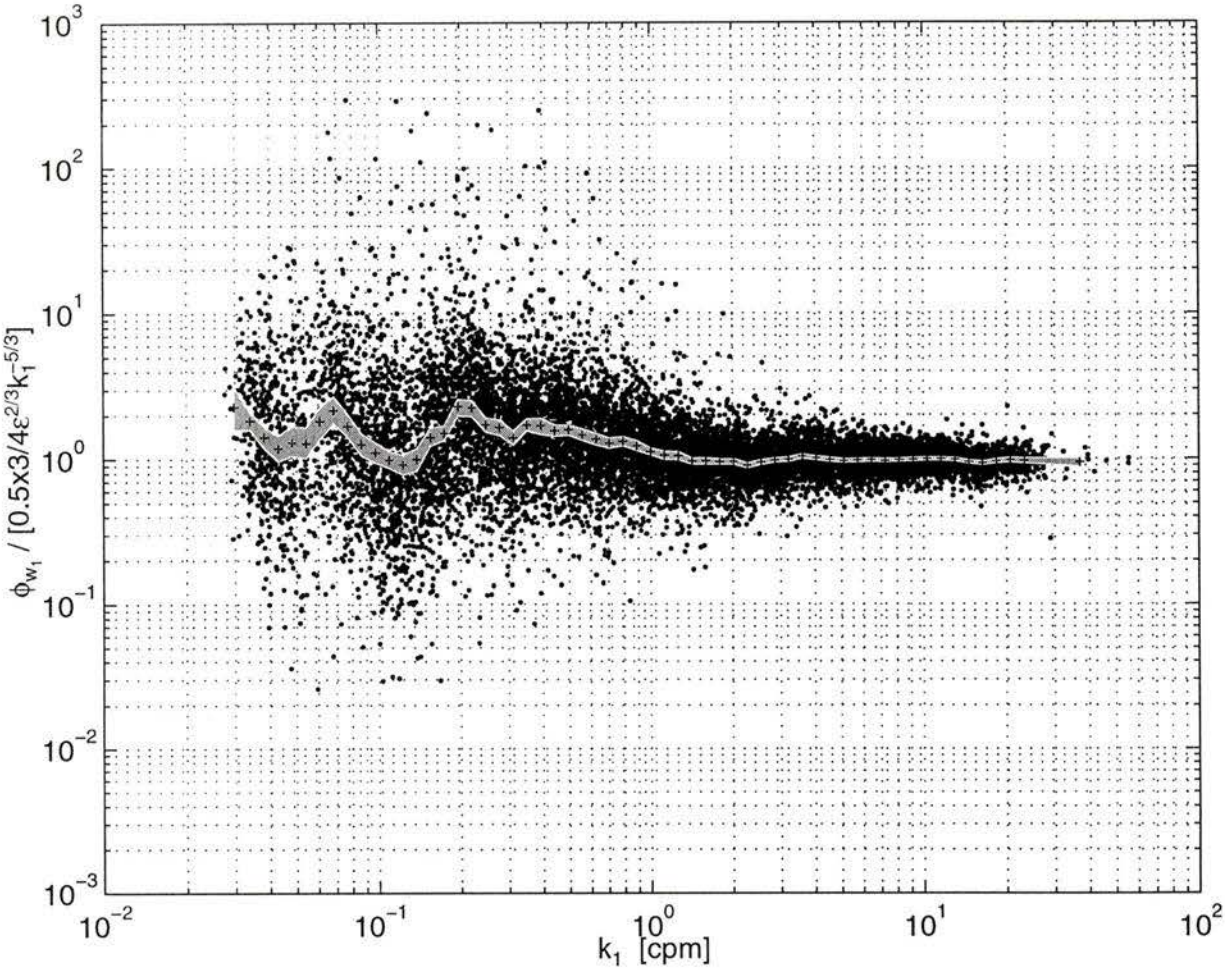

Figure 6.28: Non-dimensional spectra of w_1 from the lowest measured wavenumber to the upper edge of the inertial-subrange. The inertial-subrange of these spectra are in Figure 6.30. Shaded area is the 95% confidence interval for the averaged spectrum, using the Bootstrap method (Efron and Gong 1982).

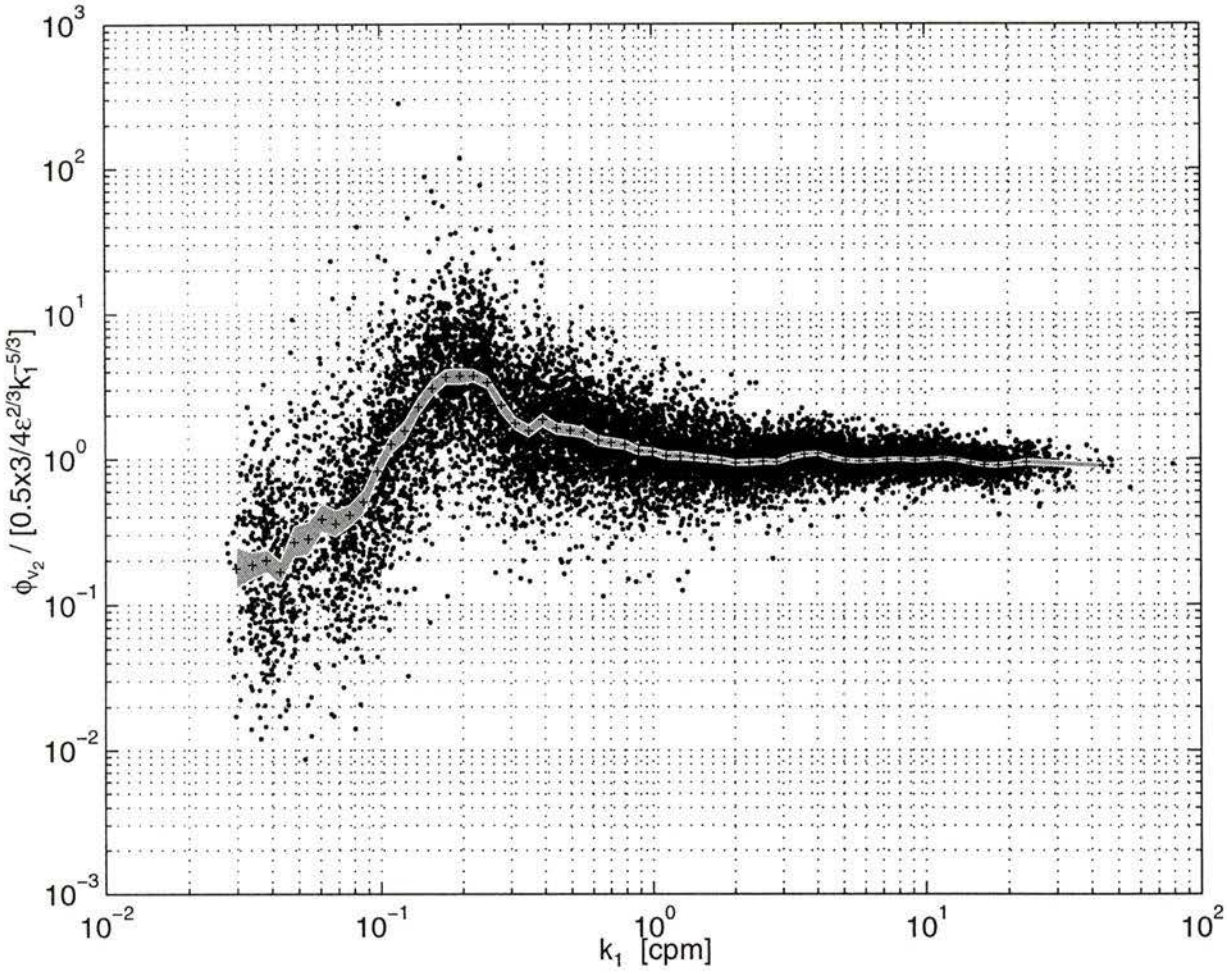

Figure 6.29: Non-dimensional spectra of v_2 from the lowest measured wavenumber to the upper edge of the inertial-subrange. The inertial-subrange of these spectra are in Figure 6.31.

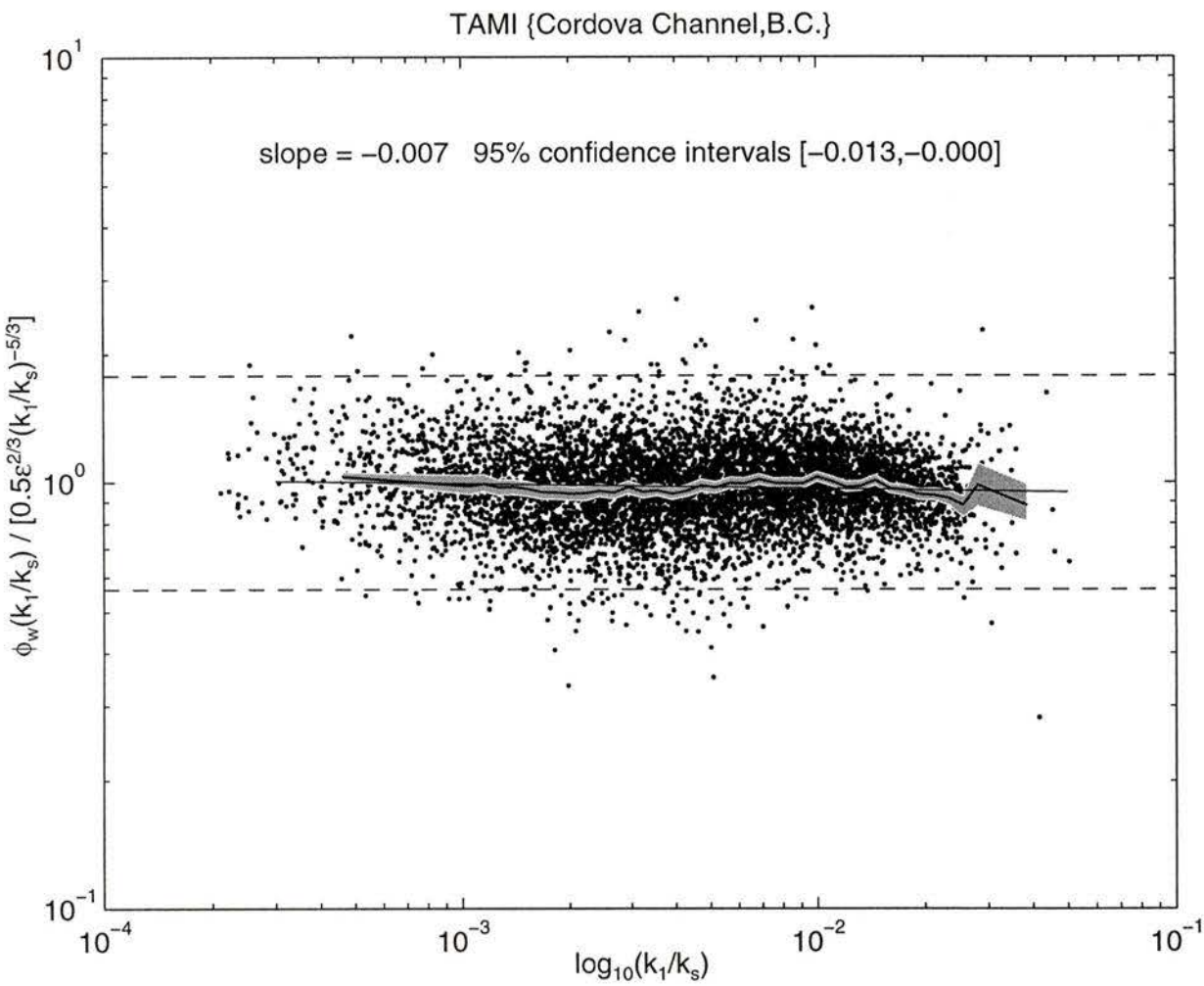

Figure 6.30: Eight-hundred-sixty-six non-dimensional spectra of w_1. The straight line indicates the slope fitted by least squares. The curve represents the averaged spectrum at 38 frequency bins with equal intervals. The two dashed lines indicate a range of $\pm 1/4$ decade of unity.

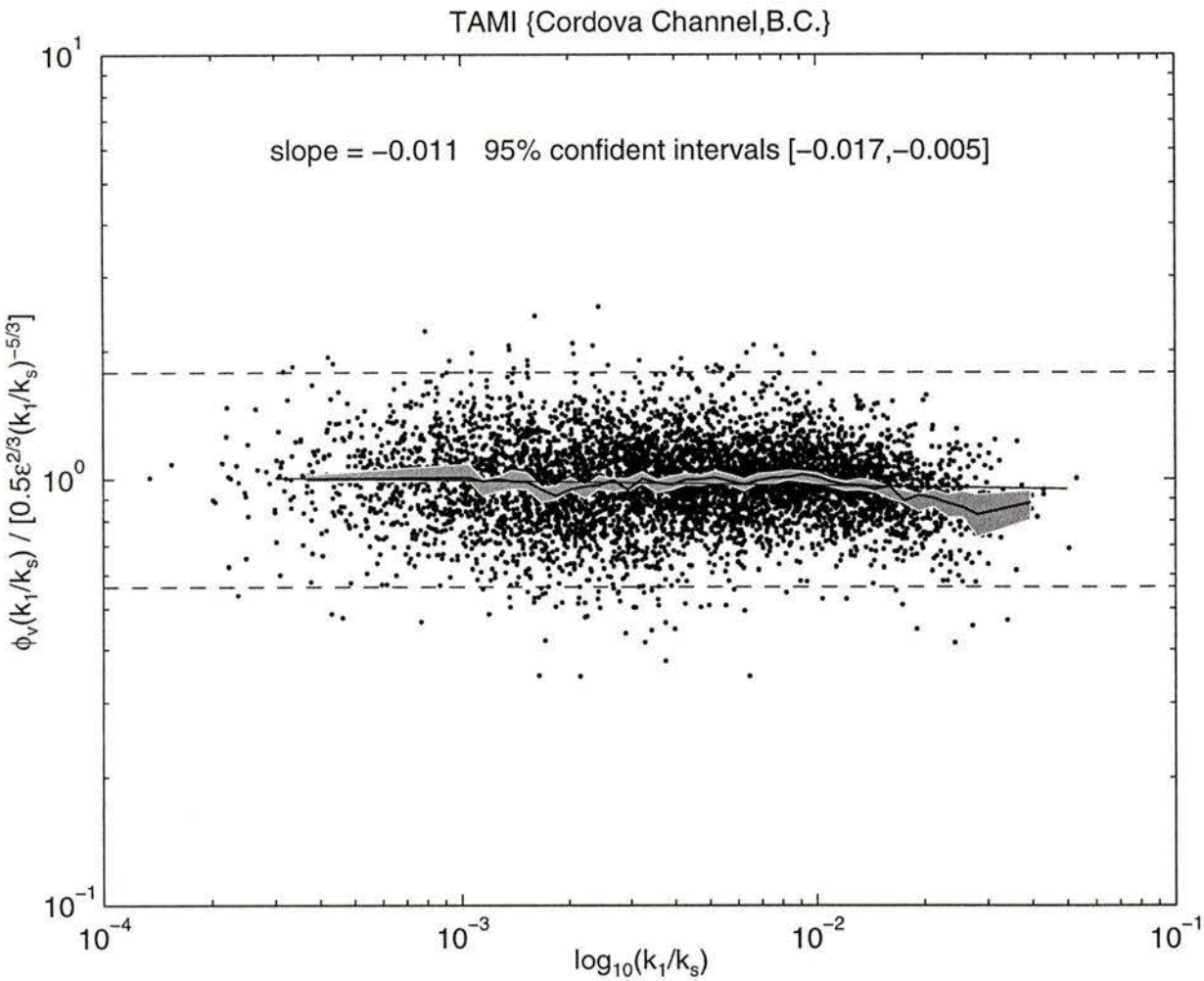

Figure 6.31: Seven-hundred-ninety-three non-dimensional spectra of v_2. Text is as that in Figure 6.30.

Spectrum	Number	slope	lower $cfd_{95\%}$	upper $cfd_{95\%}$
$(k_1/k_s)^{5/3}\phi_{w_1}(k_1/k_s)$	866	-0.007	-0.01	-0.00
$(k_1/k_s)^{5/3}\phi_{w_2}(k_1/k_s)$	874	0.006	0.00	0.01
$(k_1/k_s)^{5/3}\phi_{v_1}(k_1/k_s)$	745	0.000	-0.01	0.01
$(k_1/k_s)^{5/3}\phi_{v_2}(k_1/k_s)$	793	-0.011	-0.02	-0.00
$(k_1/k_s)^{5/3}\phi_w(k_1/k_s)$	1740	-0.000	-0.004	0.003
$(k_1/k_s)^{5/3}\phi_v(k_1/k_s)$	1538	-0.006	-0.010	-0.001
$(k_1/k_s)^{5/3}\phi(k_1/k_s)$	3278	-0.003	-0.006	-0.000

Table 6.8: Slopes of normalized spectra and their 95% confidence intervals.

The range of the inertial-subrange – where the slope is -5/3 – is more than one decades for both the vertical velocity and the horizontal velocity spectra (Figure 6.30 and 6.31). The scale of the largest eddies expected in the inertial-subrange is O(15m) – the half depth of Cordova Channel. This suggests that the inertial-subrange could extend to O(0.07cpm). However, because of body motion, the range of the detected inertial-subrange generally starts around 1cpm while 10% of spectra start from below 0.5cpm. The minimum wavenumber represented is 0.2cpm. This minimum wavenumber indicates that the scale of the largest eddies detected in the inertial-subrange is 5m. The CTD profiles suggest that there may be O(10m) eddies in Cordova Channel (Chapter 4). The vertical eddy scale (5m) is much larger than that in the open ocean, where typically scales are 0.1 - 0.5m (Gregg 1987). The largest eddy in the inertial-subrange measured at 17m below the ice in the western Weddell sea by McPhee (1995) was 4.5m. The minimum wavenumber extends to $2\times10^{-4}k_s$ for the spectra of w and v in the Kolmogoroff scaling sense (Figure 6.30 and 6.31). The maximum wavenumber for both components is between 0.2 and $0.3k_s$. This wavenumber is consistent with the upper edge of $0.25k_s$ in the inertial-subrange for the Nasmyth universal spectrum (Nasmyth 1970; Oakey 1982). The upper dimensional wavenumber is between 20 and 30cpm.

Two universal functions, $F_{22}(k_1/k_s)$ and $F_{33}(k_1/k_s)$, are obtained by scaling the

velocity spectrum of (2.33) by $(\epsilon\nu^5)^{1/4}$ in the inertial-subrange. The scaled velocity spectra are used to calculate the ratio of F_{33} to F_{22} for a pair of vertical and horizontal velocity spectra (ϕ_{w_1} to ϕ_{v_1} and ϕ_{w_2} to ϕ_{v_2}). The vertical velocity spectrum is more easily influenced by stratification than the horizontal velocity spectrum. Should stratification be important, then we expect the ratio of F_{33} to F_{22} to be significantly smaller than unity for wavenumbers smaller than the buoyancy wavenumber, $k_b = (N^3/\epsilon)^{1/2}$, and we also expect this ratio to decrease with decreasing wavenumber. The ensemble ratio of F_{33} to F_{22} formed from 113 pairs of spectra for $I < 900$ indicates that F_{33} is statistically identical to F_{22} (Figure 6.32a). If stratification had had an effect on the spectra, then the rate of F_{33}/F_{22} would be less than 1 for $k_1/k_b < 1$. The variations of the ratios about unity are random and not wavenumber dependent. Of the 26 estimates of F_{33}/F_{22} in Figure 6.32a, the confidence interval of only one the estimate is below unity. The ratio of F_{33} to F_{22} taken from 247 pairs of spectra for $900 \leq I < 3000$ (Figure 6.32b) and 981 pairs of spectra for $I \geq 3000$ (Figure 6.32c) show that F_{33} is statistically identical to F_{22} but for these spectra the resolved wavenumbers are larger than k_b and these spectra do not provide a good test for the effect of stratification. Thus, we see no evidence for the effect of stratification for non-dimensional wavenumber as small as $0.3k_1/k_b$.

6.2 Temperature

The temperature spectra examined here are also converted from the temperature gradient spectra. The spectra have been corrected for minor deviation of the gain of the differentiator. A close examination of the time series of both thermistors and the low spectral content at high frequencies of one of the thermistors (T_1) indicates that it may have been covered by material, such as jelly fish membrane. Therefore, we used only the data from the other thermistor (T_2).

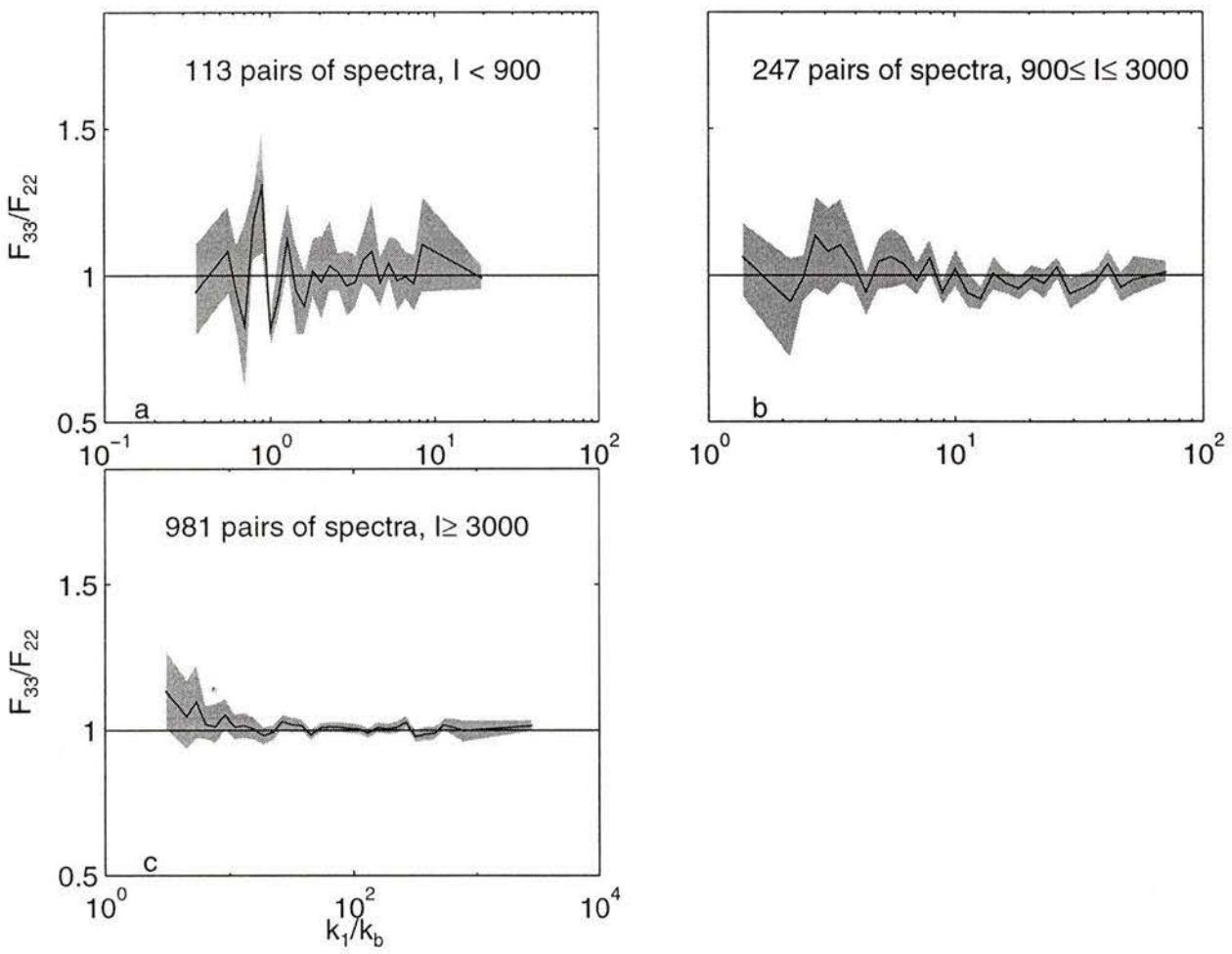

Figure 6.32: Ratio of the two universal functions in (2.33), $F_{33}(k_1/k_s)$ to $F_{22}(k_1/k_s)$, for the different levels of stratification. Buoyancy wavenumber $k_b = (N^3/\epsilon)^{1/2}$ and $[k_1]$ = cpm. Panel a: For $I = R_B^{3/4} < 900$ using 26 bins. Panel b: For $900 \leq I \leq 3000$ using 30 bins. Panel c: For $I \geq 3000$ using 32 bins.

6.2.1 Individual spectra

Like the velocity spectrum, our temperature spectra generally have well-defined minus-five-third slopes in the inertial-convection subrange regardless of whether stratification is strong or weak (Figure 6.33 and 6.34). Seventy-three percent of our spectra have very high buoyancy Reynolds numbers, where $R_B^{3/4} = I > 3000$ while only 5% have $R_B^{3/4} = I < 500$. The inertial-convection subrange of our spectra spans from $2\times10^{-4}k/k_s$ to $0.02k/k_s$.

For $I \geq 3000$, unlike our temperature spectra, Gargett (1985) found that her temperature spectra did not have a -5/3 slope while the velocity spectra, measured at the same time in Gargett *et al.* (1984), had -5/3 slope in the inertial-subrange and Gargett *et al.* deduced that the turbulence was local isotropic. The slope of her temperature spectra in the inertial-convection subrange was -3/2. Gargett suggested that this -3/2 slope of the spectra in the inertial-convection subrange was due to turbulence intermittency. The correlation coefficient, ρ, between $\ln\epsilon$ and $\ln\chi$ is zero for Gargett's measurement. According to van Atta (1971, 1973) in (2.39), a zero ρ gives a -1.56 slope. For our spectra, the correlation coefficient between $\ln\epsilon$ and $\ln\zeta$ is 0.32. [The temperature spectral level, ζ, in (2.43) is used instead of temperature dissipation, χ, due to the inconsistency of B in the literature (Gargett 1985).] According to the formula (2.39) of van Atta, the slope should be 1.61. However, the slopes of our temperature spectra are -5/3 in the inertial-convection subrange despite the intermittency of the turbulence.

Like our temperature spectra for small buoyancy Reynolds numbers ($I \leq 500$), Gargett found that her spectra had -5/3 slopes in the inertial-convection subrange for $I \sim 50 - 100$, and this low value of I was mainly due to weak turbulence rather than strong stratification. Her accompanying stream-wise velocity spectrum had -5/3 slope but the cross-stream velocity spectra did not have a -5/3 slope. Gargett suggested that the slope of her temperature spectra in the inertial-convection subrange was

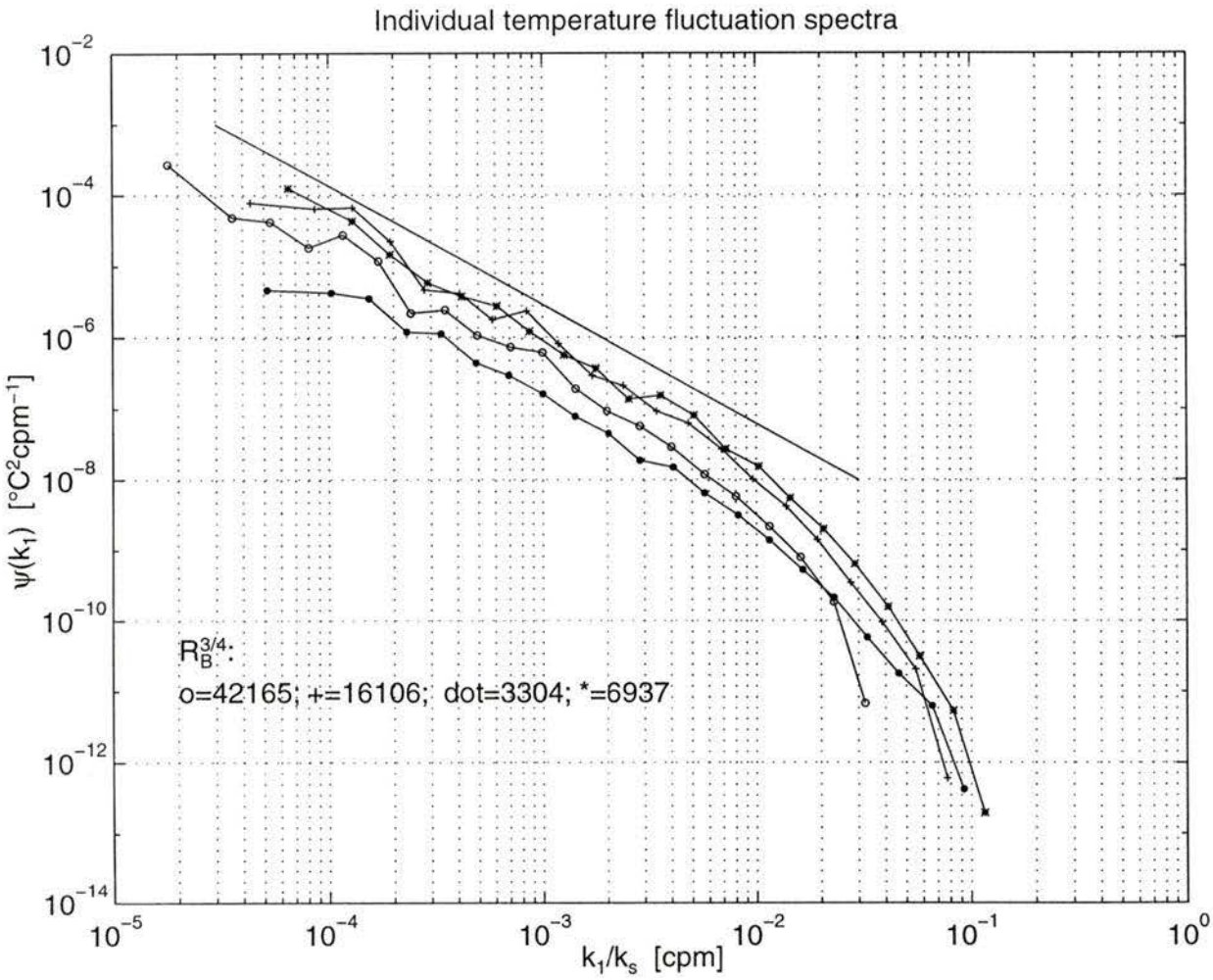

Figure 6.33: Typical individual temperature fluctuation spectra with high buoyancy Reynolds numbers. $I > 3000$ and the term $I = R_B^{3/4}$ is in (2.38). The straight line represents a -5/3 slope.

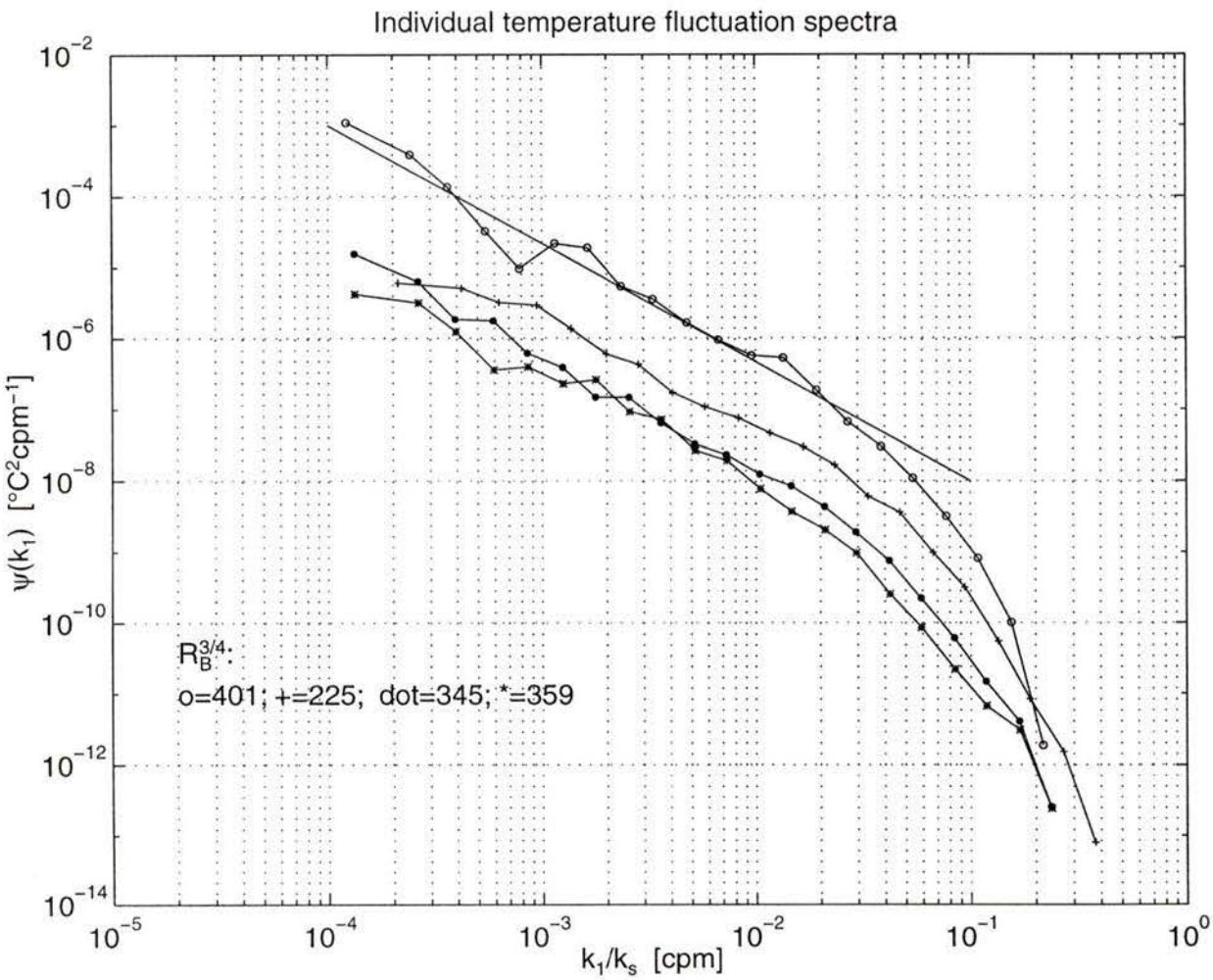

Figure 6.34: Typical individual temperature fluctuation spectra with low buoyancy Reynolds numbers ($I = R_B^{3/4} \leq 500$). The straight line represents a -5/3 slope.

-5/3 for $I \sim 50 - 100$ because the scalar spectrum was dominated by the advection of internal wave motions, giving it the same characteristics (slope of -5/3) as the horizontal velocity spectrum (ϕ_{11}). Because our spectra have a -5/3 slope for both small and large buoyancy Reynolds number, our data provide no support for Gragett's hypothesis.

6.2.2 Averaged spectrum

The fact that all of our temperature spectra have a well-defined -5/3 slope also provides us another opportunity to examine the ensemble slope from all available spectra. There are 948 temperature spectra that have simultaneous dissipation estimates from the first deployment. These 948 spectra are scaled using (2.37) and combined into a single ensemble (Figure 6.35). This scaling provides a spectrum that ideally is flat and equal to 1 for all wavenumbers. Ninety-eight percent of the non-dimensional temperature spectral points are within $\pm 1/4$ decade of unity. The mean slope is -0.003 and the 95% confidence interval of [-0.008, +0.002] indicates that the slope of the temperature spectrum in the inertial-convection subrange is -5/3$\pm$0.01. Calibration of the differentiator gains is the limiting factor on the confidence interval. The inertial-convection subrange extends from $3\times10^{-4} k/k_s$ to $0.02 k/k_s$, and is consistent with the range of the inertial-subrange for our velocity spectra. For the individual spectra, the range chosen as the inertial-convection subrange is generally the same as that of the inertial-subrange for the velocity spectra.

6.3 Discussion

The turbulence described by Gargett *et al.* (1984) is quite different from that found in Cordova Channel. In Knight Inlet, the turbulence is produced by the instability of a large amplitude lee wave generated at the sill. As the wave propagates up the inlet, it decays and progressively less energy is available for generating turbulence. Gargett

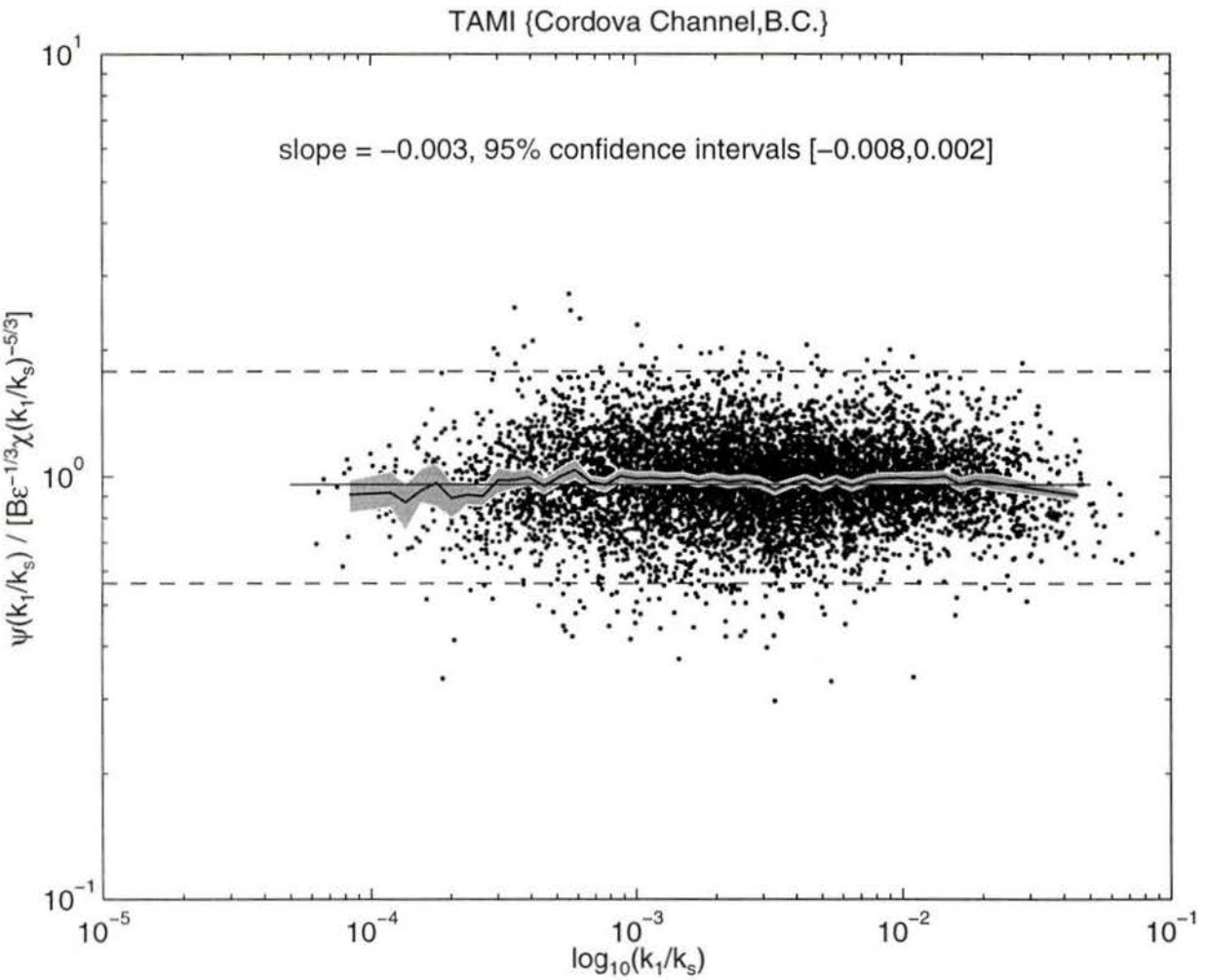

Figure 6.35: Nine-hundred-forty-eight non-dimensional temperature spectra. Text is as that in Figure 6.30. The slope of the averaged spectrum is -0.003 with a 95% confidence intervals [-0.008,+0.002].

et al. took advantage of this up-inlet weakening of the wave to sample a wide range of buoyancy Reynolds number. The background stratification did not change much in the up-inlet direction. In Cordova Channel, the turbulence is quasi-steady for time scales shorter than 2 hours. The turbulence in Cordova Channel is generated by the instability of the tidal current. Therefore, the turbulence in Knight Inlet is mostly in a state of decay and this may make the fluctuations of velocity and temperature more susceptible to the effect of stratification compared to the turbulence in Cordova Channel. This may be the reason why our spectra conform closely to the expected slope of -5/3 in the inertial-subrange.

Chapter 7

Tidal evolution of rate of dissipation of TKE

Three issues will be addressed in this chapter – (1) the evolution of the turbulence in the center of the channel and at 15m above the sea bed, (2) the relationship between the dissipation and the tidal current, and investigation that if the turbulence was generated by local bottom stress, and (3) the relationship between eddy KE and dissipation.

7.1 Time series of dissipation

Two time series of dissipation (Figure 7.36 and 7.37) are obtained by averaging all acceptable estimates from the four sensors, for each 5 minute interval. [Note that the dissipations and the measured currents are plotted separately for each lunar day.] These two time series cover 183 hours (948 estimates) for the first deployment and 114 hours (478 estimates) for the second deployment. The turbulence was very intense with the dissipations ranging from 10^{-8} to 10^{-4}W kg^{-1}. The distribution of the dissipation shows that slightly more than a half of the dissipation (52% of 1426 estimates) is between 10^{-6} and 10^{-5} W kg^{-1} while 11% is larger than 10^{-5} W kg^{-1}, and the mean is 4.1×10^{-6} W kg^{-1}. For both deployments, dissipation was usually larger by a factor of 2 - 10 during the ebb than during the flood while the current speed was also larger during the ebb than during the flood.

During the first deployment, the pattern of current and dissipation repeated with every lunar day (Figure 7.36). This pattern consists of two ebbs (E_1 and E_2) and two floods (F_1 and F_2). Current during E_1 was usually stronger than during E_2 and

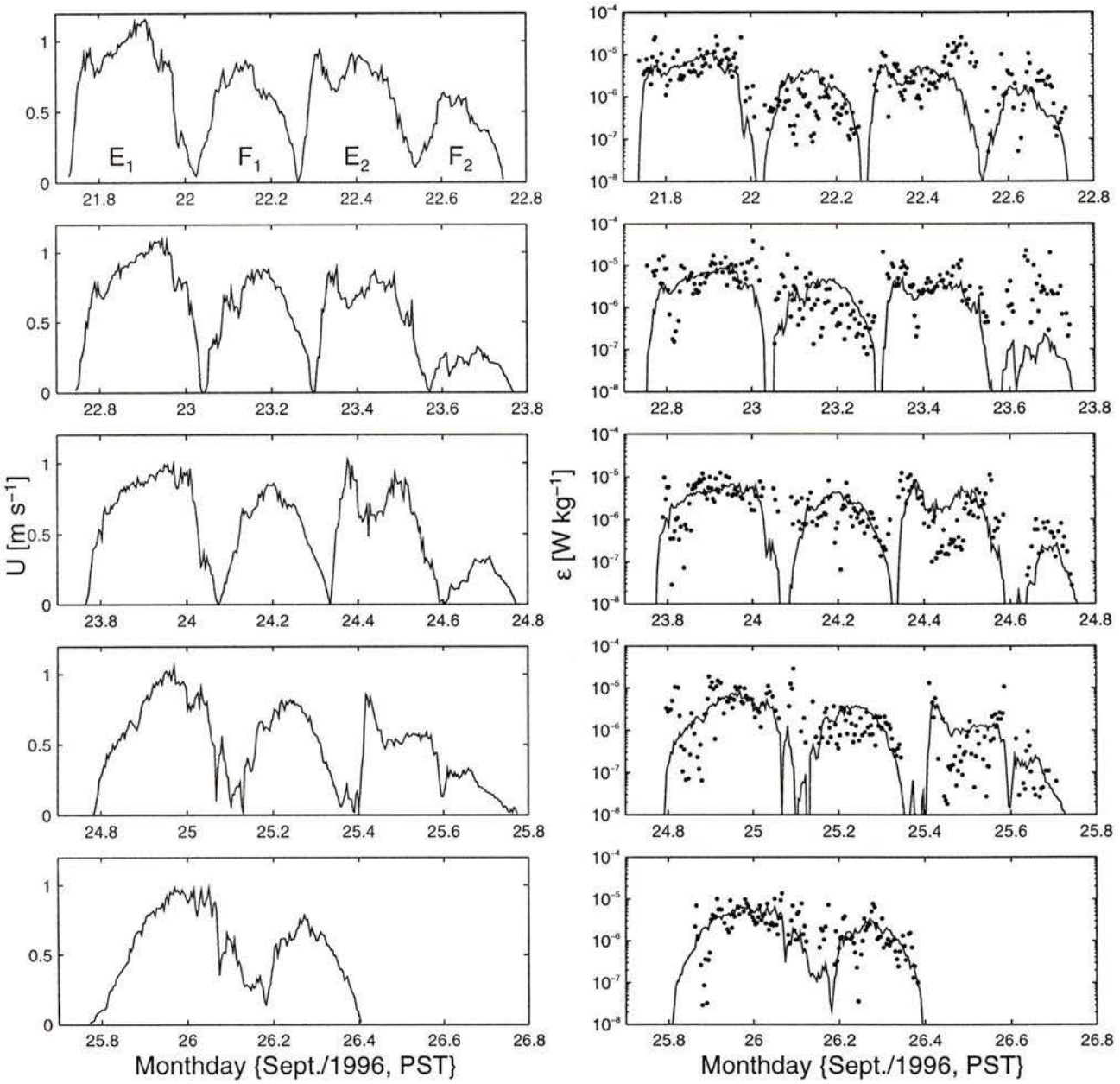

Figure 7.36: Variations of current speed and dissipation rate for each lunar day of the first deployment. Left panels: The current speed. The pattern consists of an ebb (E_1), followed by a flood (F_1), one more ebb (E_2) and one more flood (F_2). Right panels: Dissipation (points) with solid line representing $\frac{C_D^{3/2}U^3}{\kappa z}$, where $C_D = 1.2 \times 10^{-3}$.

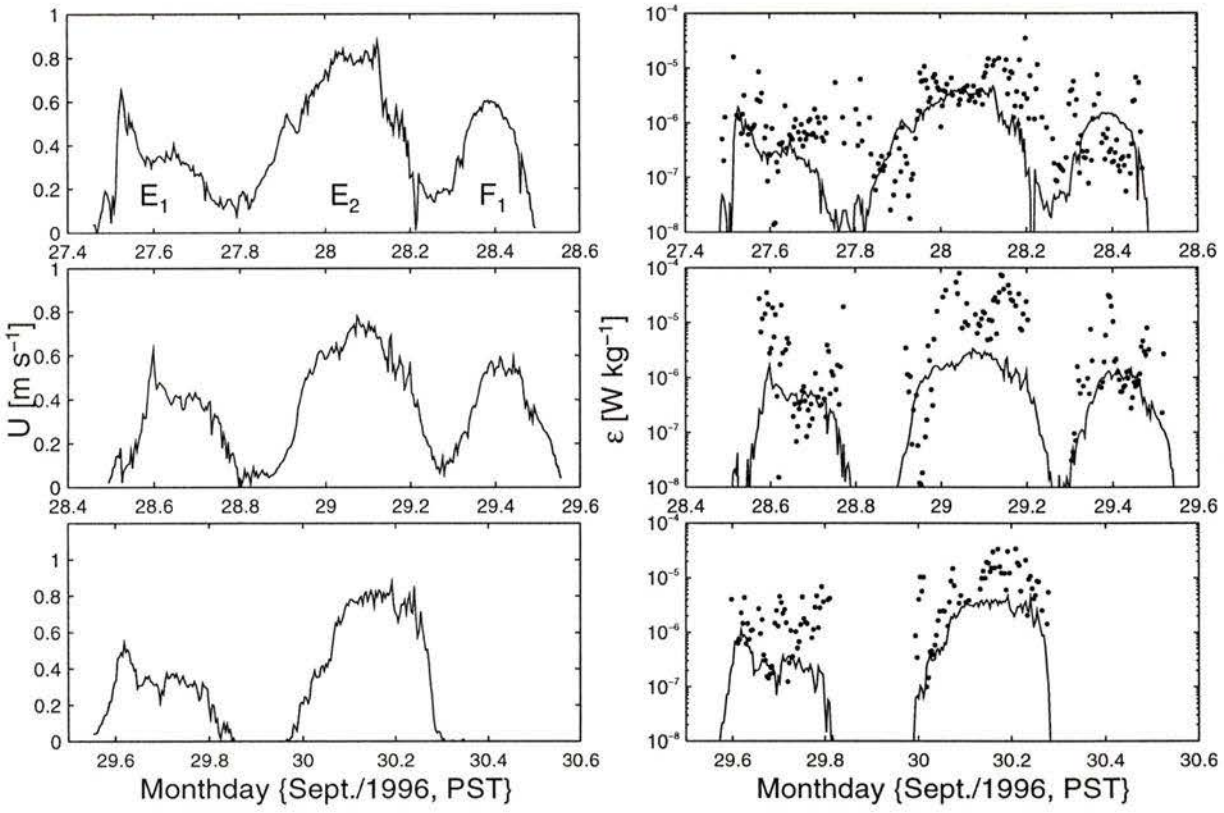

Figure 7.37: Variations of current speed and dissipation rate for each lunar day of the second deployment. Left panels: The current speed. The pattern consists of an ebb (E_1), followed by one more ebb (E_2) and a single flood (F_1). Right panels: Dissipation (points) with solid line representing $\frac{C_D^{3/2}U^3}{\kappa z}$, where $C_D = 1.2 \times 10^{-3}$.

both F_1 and F_2, while current during F_1 was usually stronger than during the second F_2. Two peaks of current during E_2 were accompanied by two peaks of dissipation during the first deployment. Dissipation during E_1 and E_2 was comparable. However, dissipation during F_2 was sometimes weaker than during F_1.

During the second deployment, the pattern consisted of two ebbs (E_1 and E_2) and a single flood (F_1). An extremum of current speed occured near the beginning of E_1. Current during E_2 was usually stronger than during E_1 and F_1 while current during E_1 was comparable to that during F_1. The difference between the two kinds of patterns of the current speeds during the two deployments was due to the evolution of the fortnightly tide.

7.2 The relationship between dissipation and tidal current

If turbulence was generated by local bottom stress, the rate of dissipation would be proportional to U^3 as given in (2.48) under the assumption of constant stress in the log-layer. However, the comparison between the dissipation and U^3 (Figure 7.36 and 7.37) shows that dissipation does not follow very closely a curve proportional to U^3.

To examine the time variation of dissipation more closely, we scale both current speed and dissipation by the local tidal peak speed cubed (U^3_{max}) in each ebb/flood, and then overlay the four-day scaled values of the first deployment separately into two single patterns, one for the scaled speed and the other for the scaled dissipation (Figure 7.38). The scaled speed (U/U_{max}) evolves sinusoidally during E_1 and F_1. During the second ebb (E_2), the scaled speed does not follow a sinusoidal pattern because of the existence of two extrema. The scaled speeds during F_2 are very scattered. During the first ebb, most of the scaled dissipations (ϵ/U^3_{max}) scattered in a range of one decade, except a few small values which occur early in this ebb. Even near the turning of the tide, when the current is weak, the scaled dissipations (ϵ/U^3_{max}) are

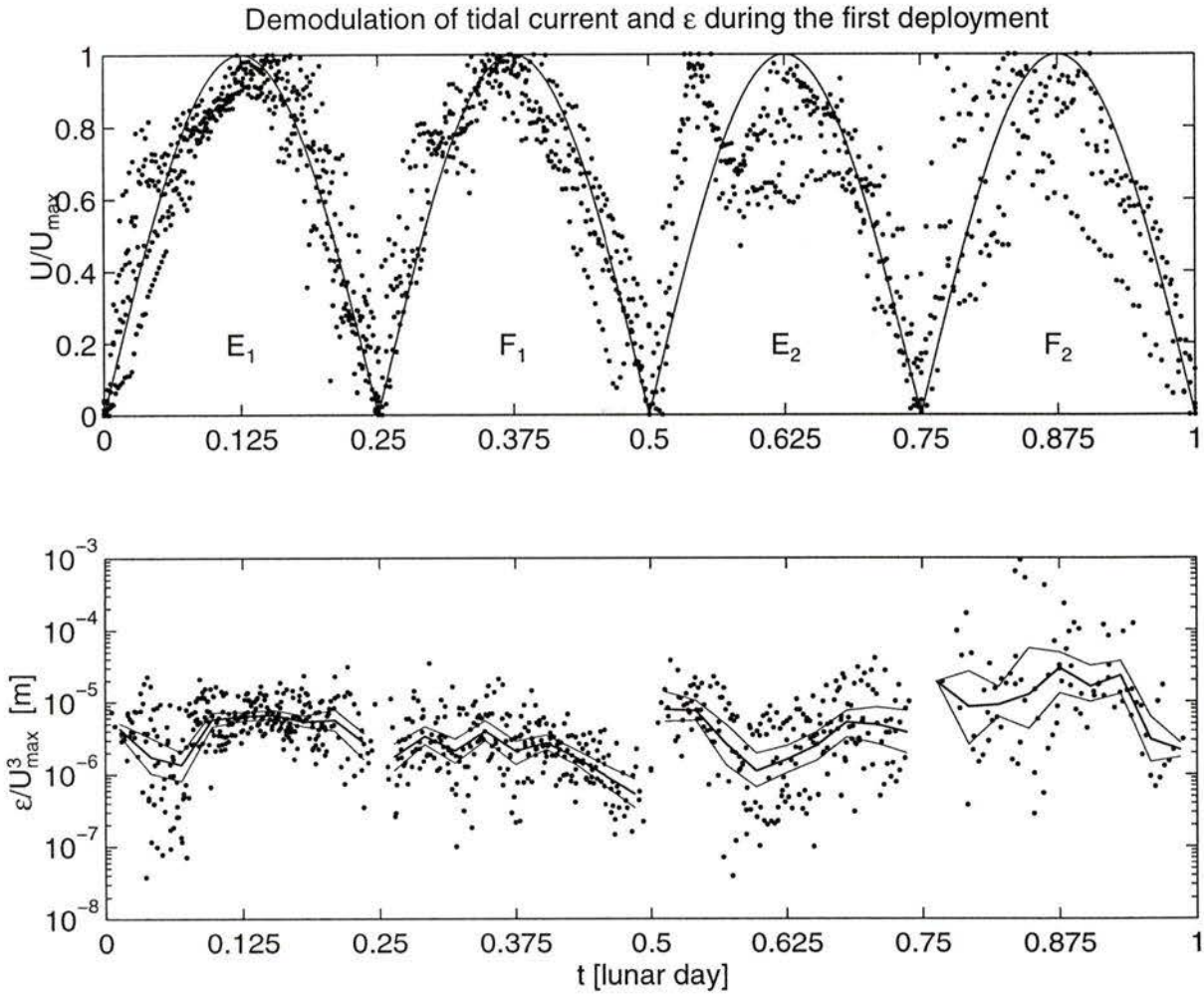

Figure 7.38: Demodulations of scaled tidal current speeds and scaled dissipations, overlaid from 4 lunar days, during the first deployment after the pattern shown in Figure 7.36. A phase of one represents a complete lunar day. Upper panel: The scaled current speed, U/U_{max}, – the current speed (U) is scaled by the maximum speed, U_{max}, of each ebb/flood. Lower panel: The scaled dissipation, ϵ/U^3_{max}.

still large. The averages over 10 uniform intervals for this ebb (E_1) and their 95% confidence intervals indicate that the scaled dissipations do not follow a sinusoidal wave. For F_1, most of the scaled dissipations also collapse into a one-decade range and their running average also indicates that the scaled dissipations do not vary sinusoidally. The scaled dissipations are more scattered during E_2 and F_2, compared to E_1 and F_1. Clearly, the rate of dissipation does not collapse into a single pattern when scaled by U_{max}^3.

During the second deployment, we also find that the scaled dissipations (ϵ/U_{max}^3) do not vary sinusoidally. The scaled dissipations also vary randomly, and, remain large near the turning of the tide.

We conclude that the turbulence was not generated by the local current, and that the rate of dissipation can not be estimated using (2.46) and (2.48). Many turbulence measurements in coastal areas with a background of tidal current have been made very close (usually within a few meters) to the sea bed (Grant *et al.* 1990; Gross and Nowell 1985; Dewey and Crawford 1988; Crawford and Dewey 1990; Bowden and Ferguson 1982). Their measurements were taken within the log-layer and the dissipation was proportional to current speed cubed as given in (2.48).

The major reason why our estimate of the rate of dissipation is not related to current speed is that the log-layer usually did not reach to the height of the moored instrument, which was nominally 15 m above the bottom. Secondly, even within a log layer, the stress is not constant and (2.46) and (2.48) may not be applicable. The stress from the measurements of the ADCP at 10 m above the sea bed is about half of that at the sea bed (Lu and Lueck 1996b). Third, the assumption of negligible pressure gradient (Tennekes and Lumley 1972; Monin and Yaglom 1970;) is violated because the pressure gradient was of the first order importance at heights exceeding several meters above the sea bed (see Chapter 4).

7.3 The relation between dissipation and eddy KE

The turbulence was not generated by the local bottom stress. Is the turbulence related to the eddy kinetic energy ?

As described in chapter 4, the measured current is composed of a tidal current and a residual non-tidal current which represents 2-D eddy velocity. Events of large eddy KE coincide with the occurrence of large dissipation rates (Figure 7.39). For example, the events of large eddy KE marked with arrows during the first deployment are accompanied by the events of the large dissipation (Figure 7.39). This coincidence suggests that the turbulence may be generated by eddies. Moreover, both dissipations and eddy KE are usually intense during the ebb. However, both dissipations and eddy KE are usually weak during the flood. During the ebb, eddies were very likely generated near Cordova Spit and the north end of James Island, which are located up-stream of TAMI but down-stream during the flood. However, the section of channel south of TAMI is quite straight and there is not obvious site for the generation of eddies. Finally, for the individual estimates, the eddy KE is not proportional to dissipation. It is not necessary to expect that there is a tight correlation in magnitude between dissipation and eddy KE because the eddy KE is advected downstream possibly from a number of source sites and the stress, shear and hence production of TKE within an eddy may not be proportional to its velocity anomaly or its KE.

During the second deployment, the dissipations also coincide with eddy KE (Figure 7.40). Again, both turbulence and eddy KE are usually intense during the ebb while both are usually weak during the flood. The eddy KE estimates from the second deployment are not reliable because of the poor fit of the tidal constituents (see Chapter 4).

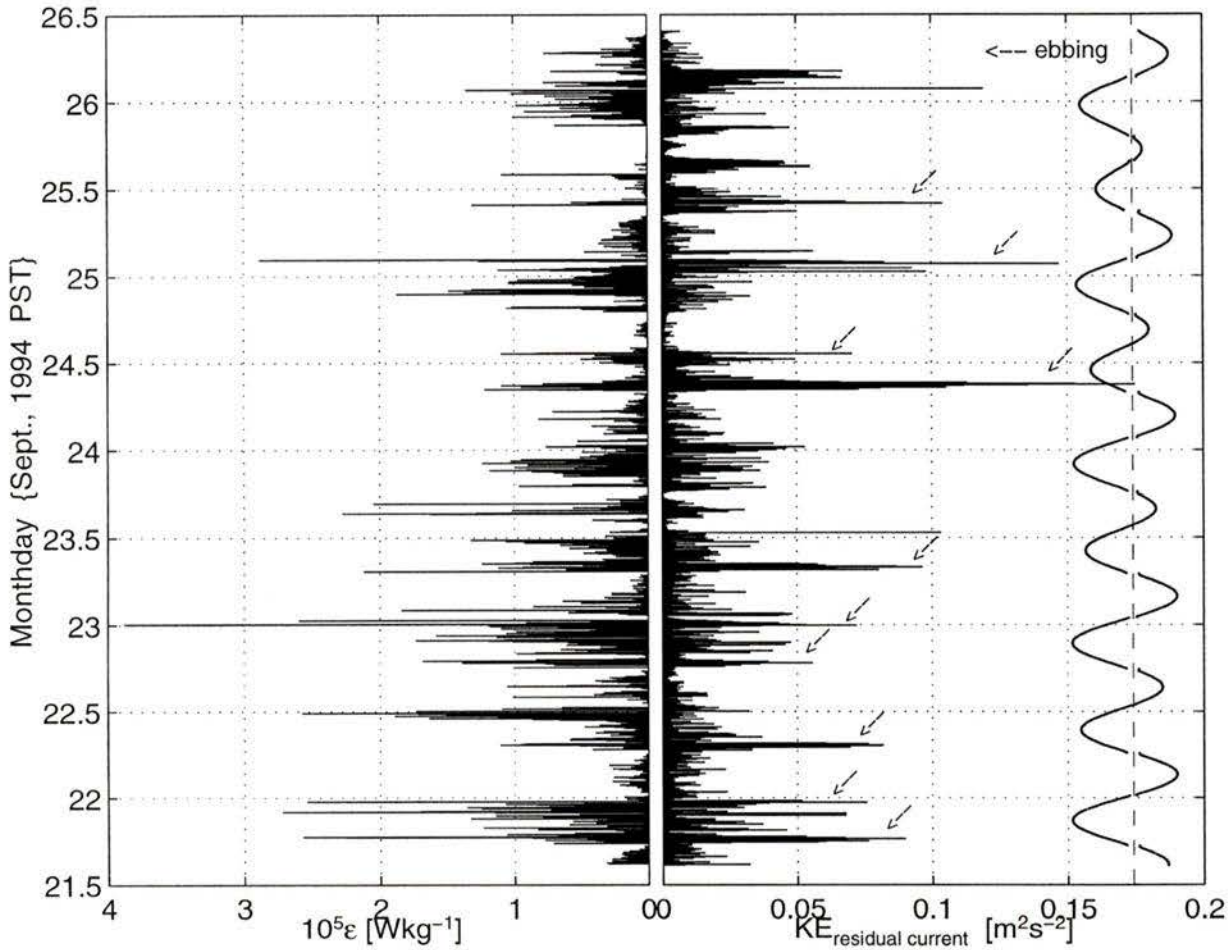

Figure 7.39: Comparison of dissipation (ϵ) against KE of the residual current (2-D horizontal eddy KE) during the first deployment. Left panel: Dissipation. A blank indicates that there was no acceptable ϵ estimated from any probe. Right panel: KE of residual non-tidal current. Arrows mark events of large eddy KE associated with events of large rates of dissipation. The tidal current speed is plotted on the right side, the dashed line denotes zero speed.

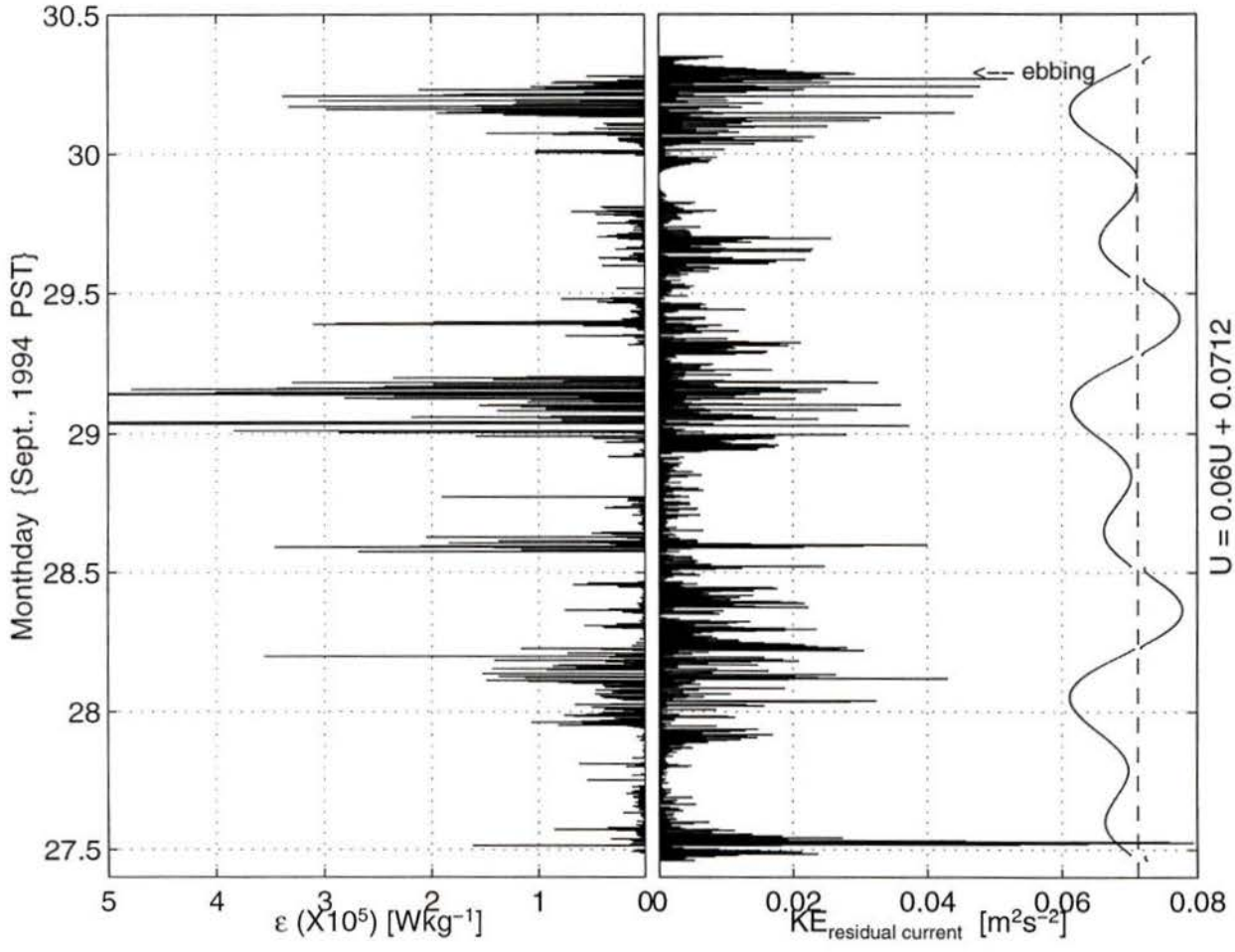

Figure 7.40: Same as Figure 7.39 except for the second deployment. Note that the maximum of dissipation on day 29.1 is 8×10^{-5}W kg^{-1}.

7.4 Discussion

There are two points that would be interesting. Turbulence at mid-depth is unrelated to the bottom stress. Even though flow was so strong the log layer seldomly reach the mid-depth. Most measurements that show the relationship between turbulence and bottom stress were conducted nearly the bottoms.

The other interesting point is that pattern of dissipation during the ebbs was pronouncedly different from that during the flood. However, the patterns of the flow was not evidently different. Stronger eddy was more during the ebbs than during the floods. These findings suggest that the geometry,i.e. headland (Cordova Spit) and the north end of James Island would be a important factor. South to the instrument, the channel is quite straight, particularly two 20 isobaths each closing a shore. Water during the flood straightly flows into the channel and passes through. There is no evident eddy generation sites.

Chapter 8

Turbulent mixing in Cordova Channel

In this chapter, I will (1) compare the estimated rate of dissipations of TKE obtained from TAMI against that from an acoustic scintillation system, (2) test if dissipation is balanced by the production of TKE, and (3) estimate the decay times for eddy KE and the tidal KE. In addition, I will examine the relationship between eddy diffusivity and Richardson number, and the relationship between temperature spectral level and mean temperature gradient.

8.1 Comparison of the rates of dissipation obtained with TAMI against an acoustic scintillation system

As mentioned in chapter 4, the path of the acoustic scintillation system was within 130 m of TAMI. The dissipation estimated with the acoustic system was based upon the spectral level of a cross-stream velocity fluctuation (v), using the inertial-subrange technique (Di Iorio 1994, 1995). The estimates were typically averaged over 30 minutes and provided a cross-channel average at 15m depth. [Note that the estimates of the acoustic system were not uniformly spaced in time.] The estimates obtained with TAMI were five-minute averages. For consistency, we only used the dissipation estimated from v-probe on TAMI for this comparison.

The comparison between the dissipations estimated with TAMI and the acoustic system is shown in Figure 8.41. Individual estimates are in a good agreement. The variations of individual estimates for the two instrument follow each other closely,

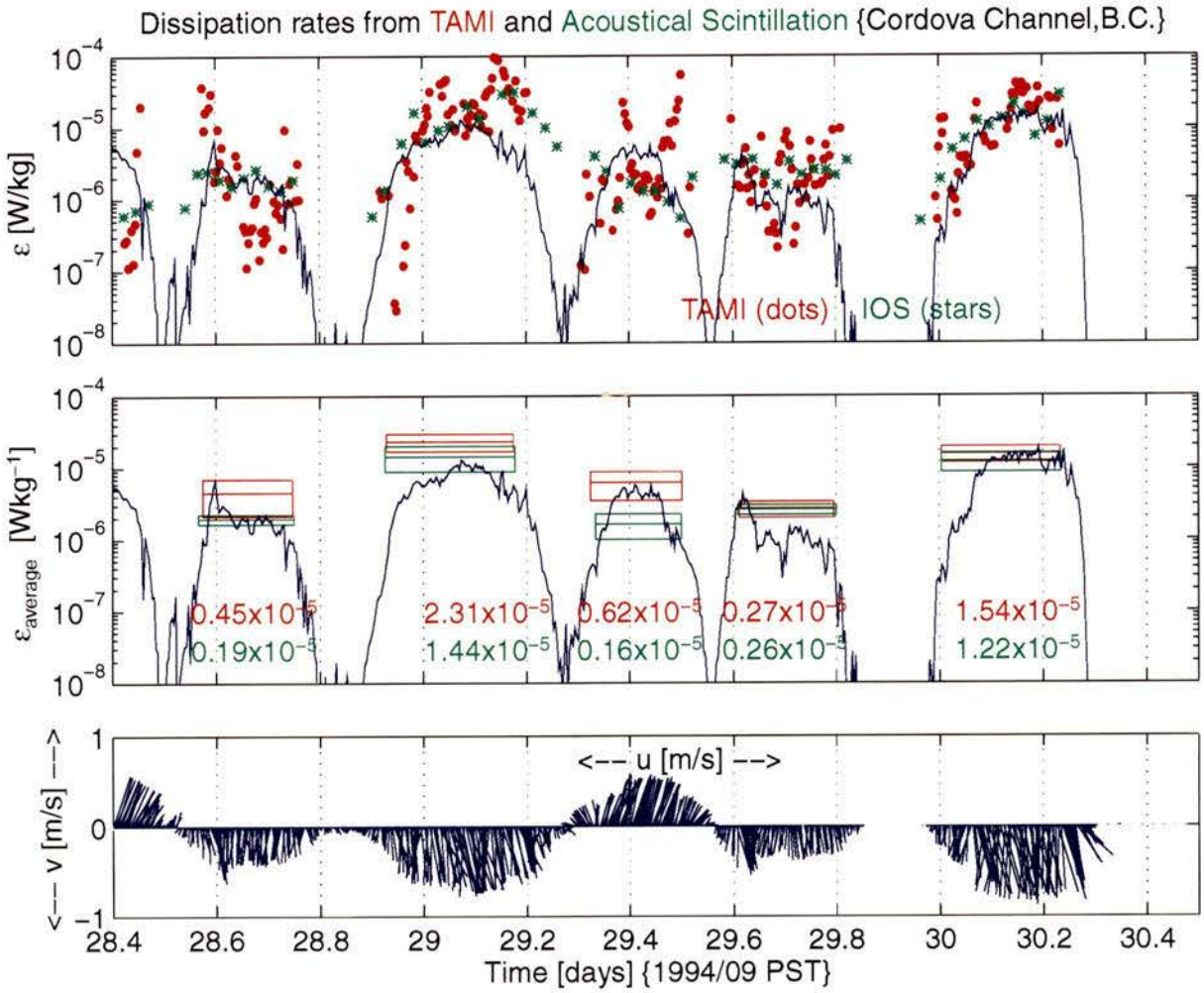

Figure 8.41: Comparison dissipation estimates of TAMI (red) against that of the Acoustic Scintillation system (IOS) (green). Upper panel: Individual estimates. Solid line is proportional to U^3. Middle Panel: Averages over common intervals. The middle line in a box represents the average and the upper line and lower line indicates 95% confidence interval. Lower panel: Current vectors.

particularly during the second, third and fourth ebbs. Because our estimate is averaged over a shorter period and represents a "single" point in the center of the channel, the variation of our estimate is larger than that from the acoustic system because of occasional anomalous events. Anomalous events are observed by TAMI during the first ebb and the second flood and usually have extremely large dissipations. The averages over common intervals are also in a good agreement (Figure 8.41), except for the values during the first ebb and the second flood. However, the averages from TAMI and the acoustic system during these two periods are still within the same orders of the magnitudes, and, only during the 2nd flood, both confidence intervals fail to overlay. Excluding the averages of the first ebb and the second flood, the averages from TAMI equal those from the acoustic system within a factor of 1.4. Combining all averages, the estimates of dissipation from both instruments are equal within a factor of 1.6.

The estimates of dissipation from the acoustic system were averaged across the channel. The dissipation close to the lateral boundaries should be larger than in the center of the channel and the cross-channel average provided by the acoustic system should be larger than the dissipation in the center of the channel. Our results are the opposite of this expectation. The transmitter and receiver of the acoustic scintillation system were setup on the side slopes near the 17 m isobath (see Figure 4.3) and shoal effect may not be significant.

8.2 Comparison of dissipation against the production of TKE

The estimates of production of TKE at 15 m above the sea bottom using the data taken with the ADCP (Lu and Lueck 1996b), which was mounted on the bottom of Cordova Channel approximately 90 m from TAMI, provide an opportunity to examine the local balance of dissipation and the production of TKE. The estimates of the production were 20-minute averages between 13.6 and 16.5 m above the bottom. The

two instruments (TAMI and ADCP) were not co-located but were sufficiently close that average quantities may be comparable.

The estimate of the production was the sum of two components - $-\overline{uw}\frac{\partial U}{\partial z}$ and $-\overline{vw}\frac{\partial V}{\partial z}$. Although the tidal flow was not steady, the time derivative of the turbulent kinetic energy ($\frac{\partial q^2}{\partial t}$, where q^2 is TKE) as well as its vertical transport ($w\frac{\partial q^2}{\partial z}$) is small compared to the production (Lu, personal communication, 1996).

The statistical fluctuations of the individual estimates are very large making it difficult to compare production against dissipation (Figure 8.42). When the estimates are averaged over intervals of approximately a quarter tidal cycle, the means and their 95% confidence intervals agree quite well, except for the 1st and 4th averages which have larger dissipation than the production. There are only a few estimates during the 2nd flood and the confidence interval is quite large. The confidence intervals fail to overlap only for the 1st and 4th estimated means. A regression of the means indicates that production was balanced by the dissipation within a factor of 2 (ignoring the two estimates from the 2nd flood), with the dissipation exceeding the production slightly.

8.3 Estimating of decay time scales for eddy KE and tidal KE

Assuming that the eddy KE in Cordova Channel was eventually dissipated by turbulence, we can estimate the decay time for the eddy kinetic energy. The comparison of ϵ to production (Figure 8.42 and 8.43) indicates that the TKE was nearly in local balance. A histogram of the ratio of eddy KE to dissipation (Figure 8.44) shows that the distribution is approximately lognormal. Slightly more than 98% of the ratios are between approximately 1 minute and 100 hours and 83.2% between 6 minutes and 10 hours. The most probable value is 55 minutes while the logarithmic average is 75 minutes. However, the linear mean is 9 hours due to a few extreme values and the median is 69 minutes, close to the logarithmic mean of 75 minutes. Thus, the

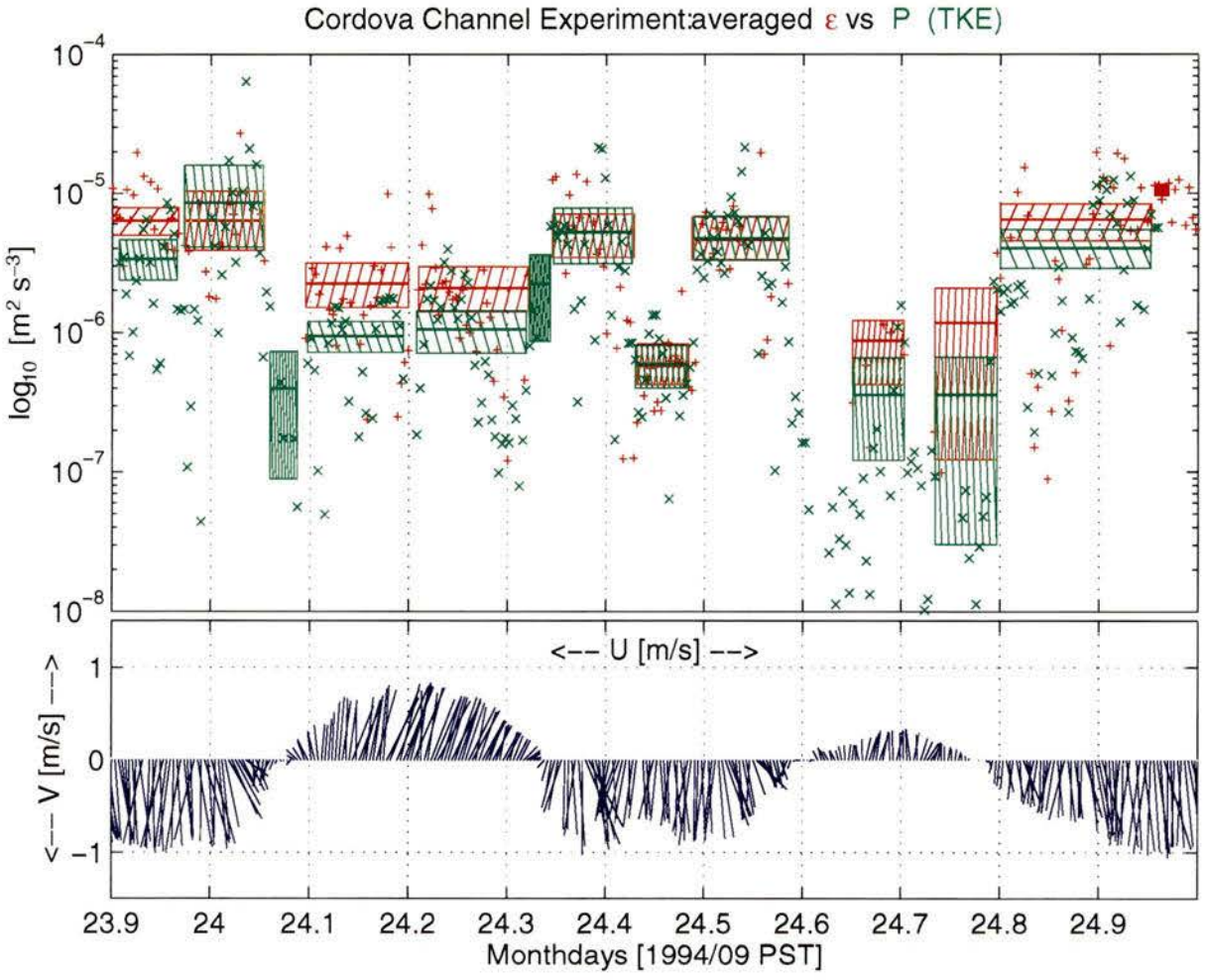

Figure 8.42: Upper panel: Comparison of the rate of dissipation, ϵ, (red +) estimated using TAMI and the productions, $P = -\overline{wu}\frac{\partial U}{\partial z} - \overline{wv}\frac{\partial V}{\partial z}$, (green $\times$) of TKE estimated using the ADCP. The individual estimates of both dissipation and production were averaged over 20 minute intervals. The rectangles represent common averages over about a quarter of a tidal cycle. The length of each box denotes the averaging time interval. The middle line of each box denotes the average, and the bottom and top lines of the denote its 95% confidence interval. Note that the periods with only green box have no dissipation. Lower panel: The current vectors.

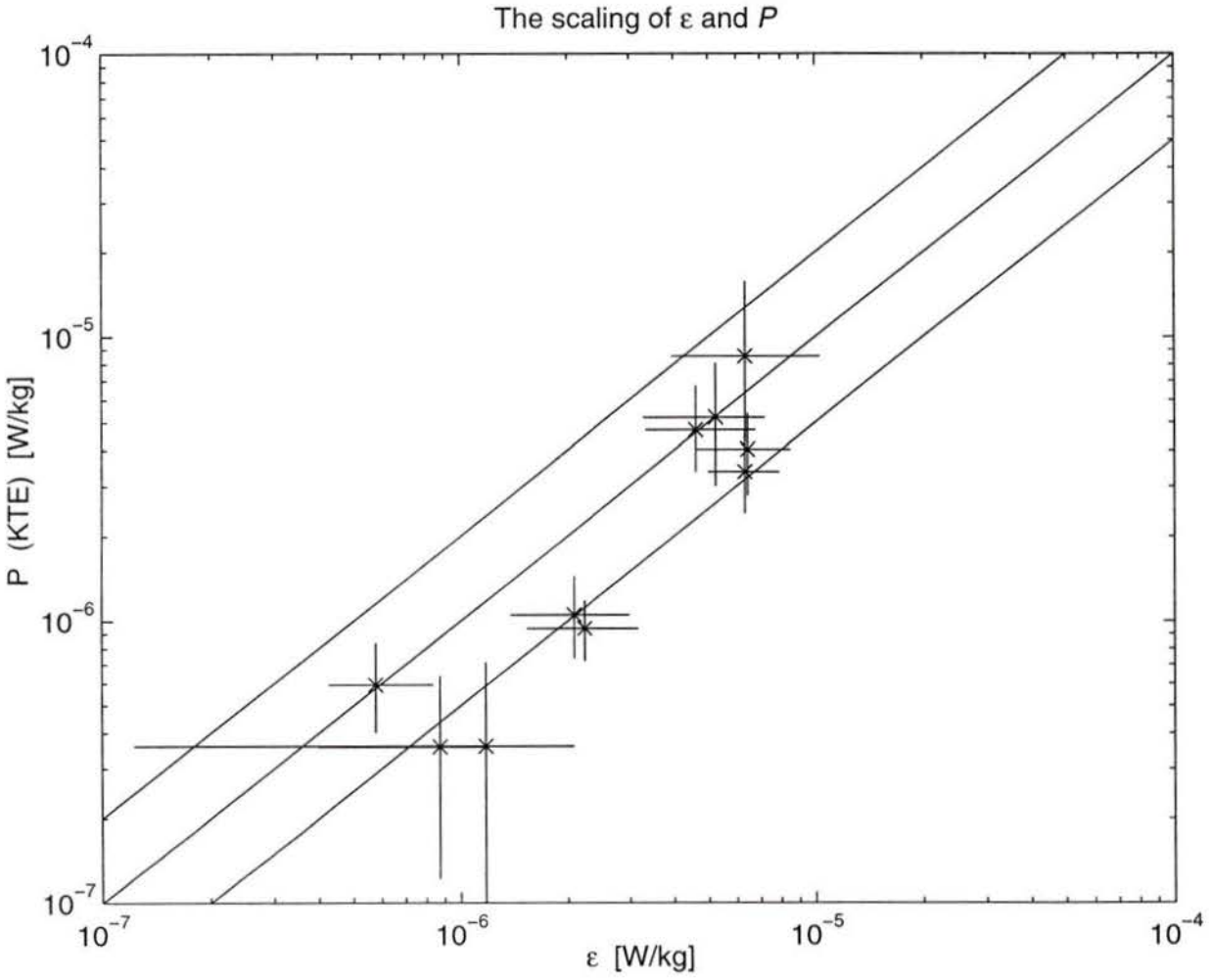

Figure 8.43: Comparison of averages of ϵ and P shown in Figure 8.42. Bars are 95% confidence intervals. Lines represent a factor of 2 from equality.

observed rate of dissipation could decay the eddy within a little longer than one hour.

With a typical current speed of 0.6m s^{-1}, an eddy would travel 3 km during a decay time. The traveling distance is approximately that from TAMI to the north end of James Island.

The bulk of kinetic energy in the channel was tidal and some fraction of it gets dissipated locally. Comparison of dissipation against the tidal KE (Figure 8.45 and 8.46) indicates that, during the ebb, both the tidal KE and the averaged dissipation rate were large while both were weak during the flood, except an event of large dissipation during the second flood of the second deployment. We will examine the percentage of tidal KE dissipated over each ebb (flood) of the tide by comparing the mean KE against the time integrated dissipation. A regression (Figure 8.47) of the time integrated dissipation against the tidal KE indicates that 53% of tidal KE is dissipated locally. This estimate is obtained by using those data falling within the two dotted lines (Figure 8.47). Seventy-seven percents of the tidal KE is dissipated locally if we take all the data for this estimate. Another regression (Figure 8.47) that minimizes the absolute deviation (Press *et al.* 1989) and uses all data indicates 84% of the tidal KE dissipated locally.

8.4 Eddy diffusivity and Richardson number

The eddy diffusivity for density, K_v, is estimated using the upper limit of (2.12) and $\Gamma = 0.2$. A clear tidal signal of eddy diffusivity is not evident in Figure 8.48. However, a large eddy diffusivity usually occurs during periods of strong ebbing because of large dissipations and weak stratification (small buoyancy frequency squared). Variations of the eddy diffusivity are usually larger during the flood than during during the ebb.

If stratification is weak, the density may act as a passive scalar and its diffusivity may be equal to the eddy viscosity. To examine the eddy diffusivity at mid-depth against the prediction of the eddy viscosity of (2.49), we scale eddy diffusivity with

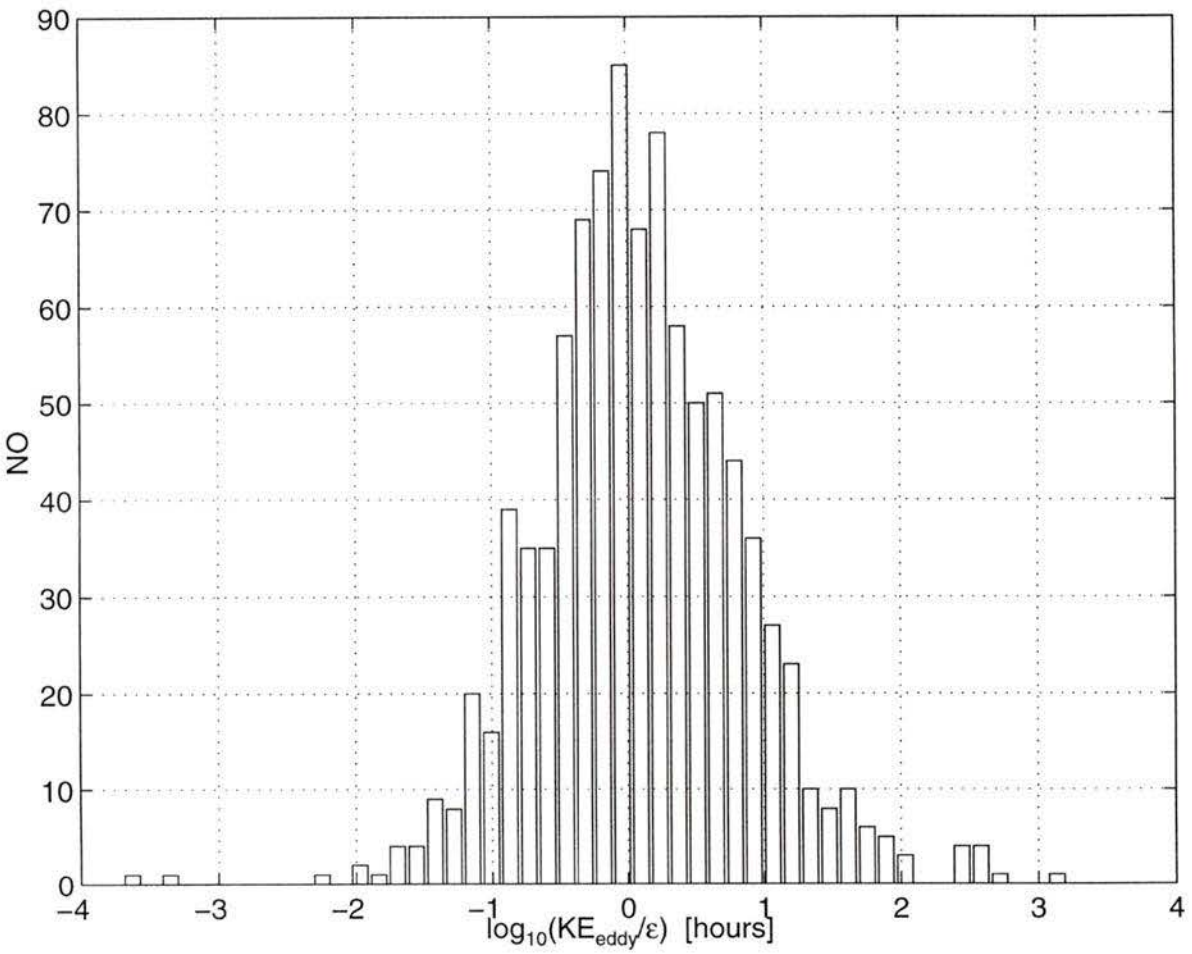

Figure 8.44: Histogram of the ratio of KE of the eddy to the dissipations. The time scale for the turbulence of eddy KE was 75 minutes.

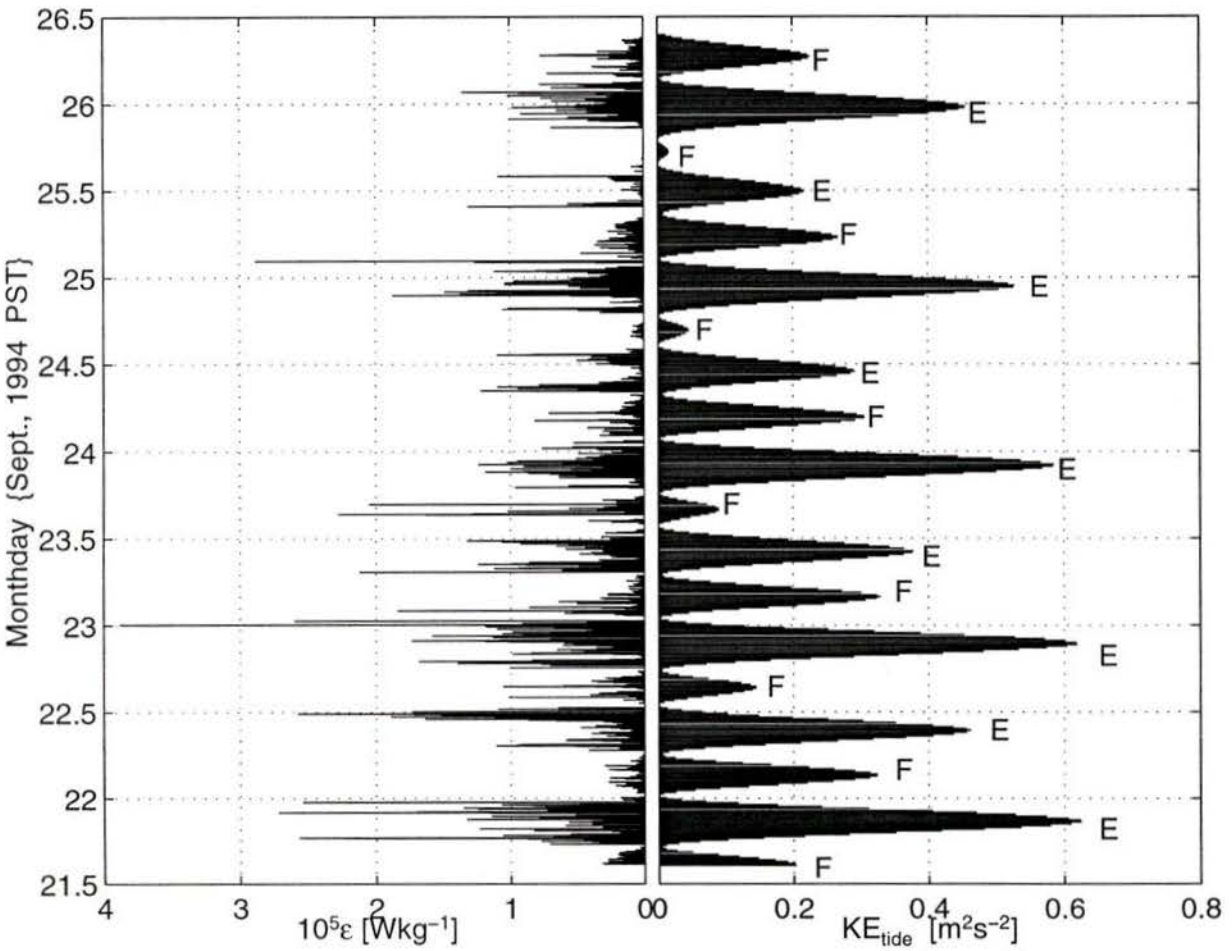

Figure 8.45: Comparison of dissipation (ϵ) and KE of tidal current during the first deployment. Left panel: Dissipation ($\times 10^5$). Right panel: Tidal KE, every third samples is plotted. An "E" denotes an ebb and a "F" denotes a flood.

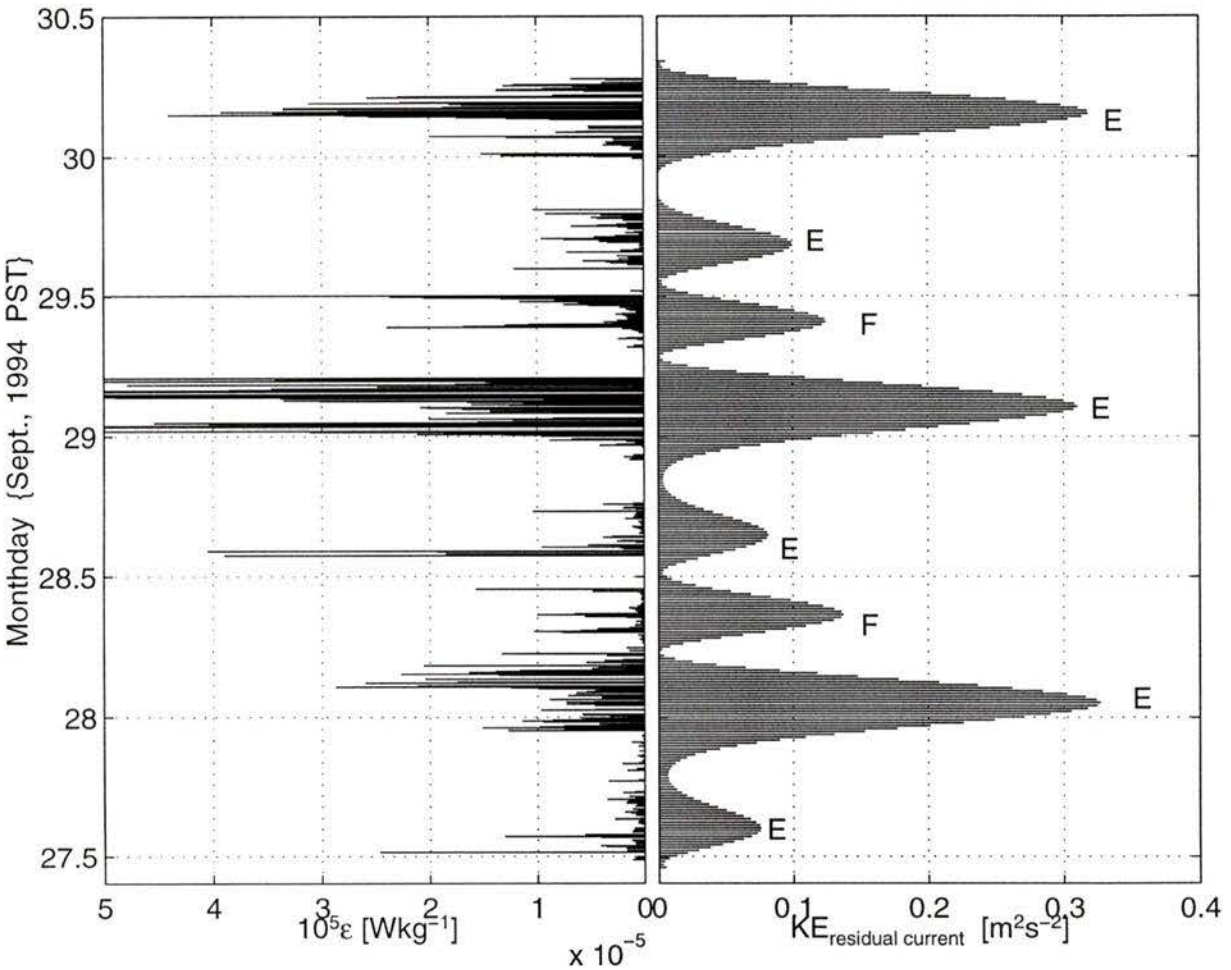

Figure 8.46: Comparison of the dissipations and the tidal KE during the second deployment. Right panel: Tidal KE with every third sample plotted. An "E" denotes an ebb and a "F" denotes a flood.

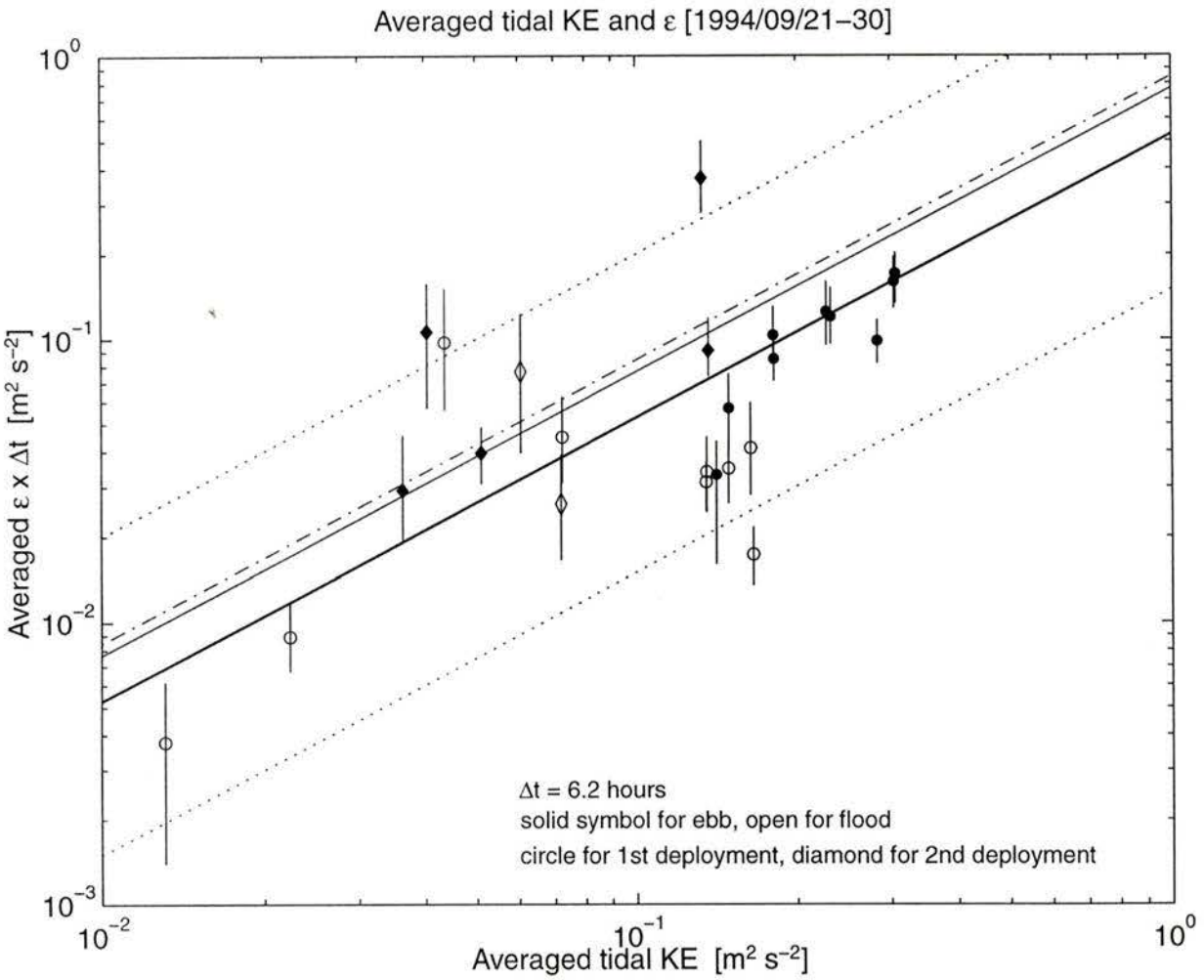

Figure 8.47: Comparison of the energy dissipated (averaged $\epsilon \times \triangle t$,where $\triangle t$ = 6.2 hours) against the averaged tidal KE over successive 1/4 lunar days. The solid (open) symbols represent ebb (flood). The circle (diamond) denotes values for the first (second) deployment. The bar denotes 95% confidence interval estimated with the bootstrap method. The thicker solid line denotes the value (53%) which is the averaged ratio of $\epsilon \times \triangle t$ to tidal KE, estimated using the data within the two dotted lines. The thinner line denotes the slope (77%) obtained by a 1st order least square fit using all data. The dash-dot line denotes the slope (84%) obtained by the method of minimum absolute deviation (Press *et al.* 1989) using all data.

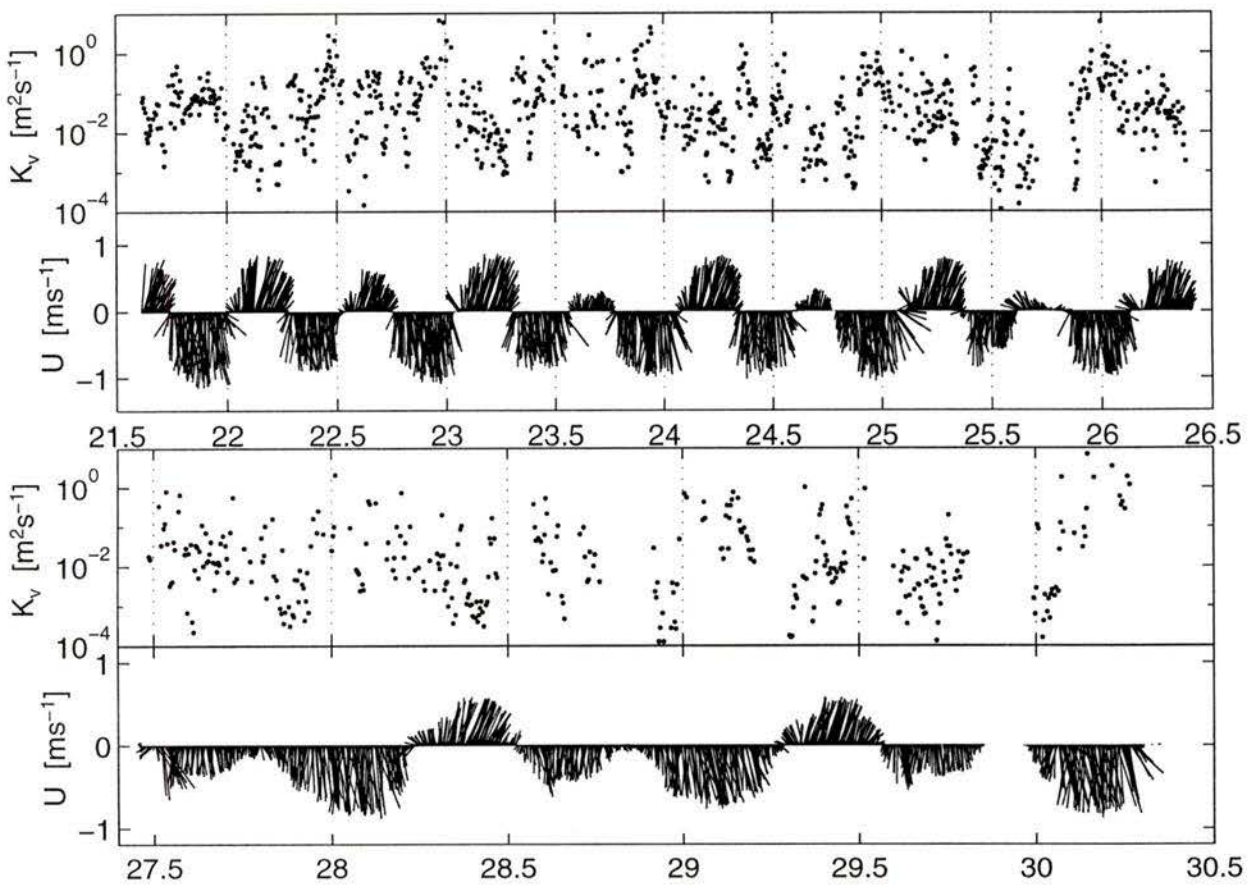

Figure 8.48: The eddy diffusivity, $K_v \leq \Gamma\epsilon/N^2$, during the experiment estimated with the upper limitation of $0.2\epsilon/N^2$. Upper two panels: Eddy diffusivity, K_v, and the current vectors during the first deployment. The dots denote K_v, the sticks denote the current vectors. Lower two panels: Eddy diffusivity, K_v, and the current vectors during the second deployment.

(2.50) because we have no estimates of friction velocity, u_*. The scaled eddy diffusivity is shown in Figure 8.49. Because the observations are usually above the logarithmic layer, we expect the turbulence would be weaker than that in a logarithmic layer. However, the observation shows that the estimate of eddy diffusivity above the logarithmic layer is quite close to the prediction for a logarithmic layer.

To examine the relationship between eddy diffusivity and the possibility of shear instability, we compare the scaled eddy diffusivity with the Richardson number, Ri (Figure 8.50). For the three days when the Richardson number estimates are available, the data are quite scattered, but reveal a trend of decreasing eddy diffusivity with increasing Richardson number. The non-dimensional eddy diffusivity is frequently of order 1. When $Ri < 1/4$, the eddy diffusivity is usually large (most values have order of 1). Thus, intense turbulent mixing usually occurs at time of weak stratification and strong shear. A regression indicates $K_v/\kappa z\sqrt{C_D}U \propto Ri^{-0.7}$ (Figure 8.50).

8.5 Temperature spectral level

The temperature spectral level, ζ, of (2.43) is estimated rather than the rate of dissipation of temperature fluctuation variance for the reasons discussed in Chapter 2. The temperature spectral level in conjunction with viscous dissipation, ϵ, gives a measure of the temperature variance dissipation, χ.

The temperature spectral level is compared against the vertical gradient of mean temperature in Figure 8.51. High spectral levels are usually associated with strong absolute vertical gradients. The average of the ratio of the gradient to the spectral level is 3×10^{-4}[°C m^{-1}s]. Ninety-five percent of all the data fall within a range of $|\frac{\partial T}{\partial z}/20| \leq 3 \times 10^{-4}\zeta \leq |20\frac{\partial T}{\partial z}|$.

Using (2.43) for the estimate of χ and with the concept of an eddy diffusivity ($K_T = 2\chi/\left(\frac{\partial T}{\partial z}\right)^2$) for heat according to Osborn and Cox (1972), we estimate K_T and compare it against the eddy diffusivity for density, K_v (Figure 8.52A, B). As

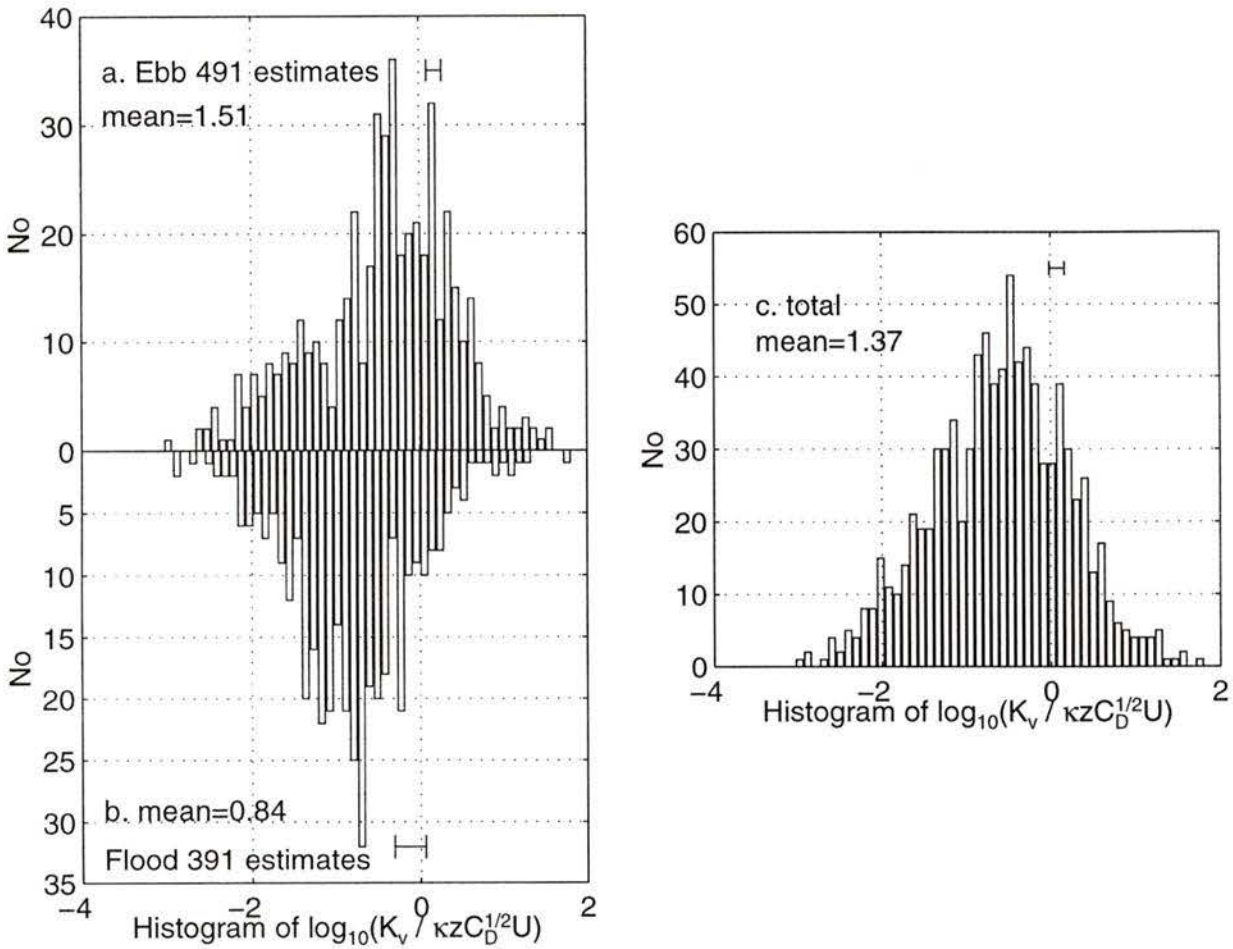

Figure 8.49: The scaled eddy diffusivity, K_v in Figure 8.48, by $\kappa z C_D^{1/2} U$: *a.* scaled K_v during the ebbs, *b.* scaled K_v during the floods, *c.* scaled during the both ebbs and floods. Error bar of the mean on each panel is estimated with the Bootstrap method.

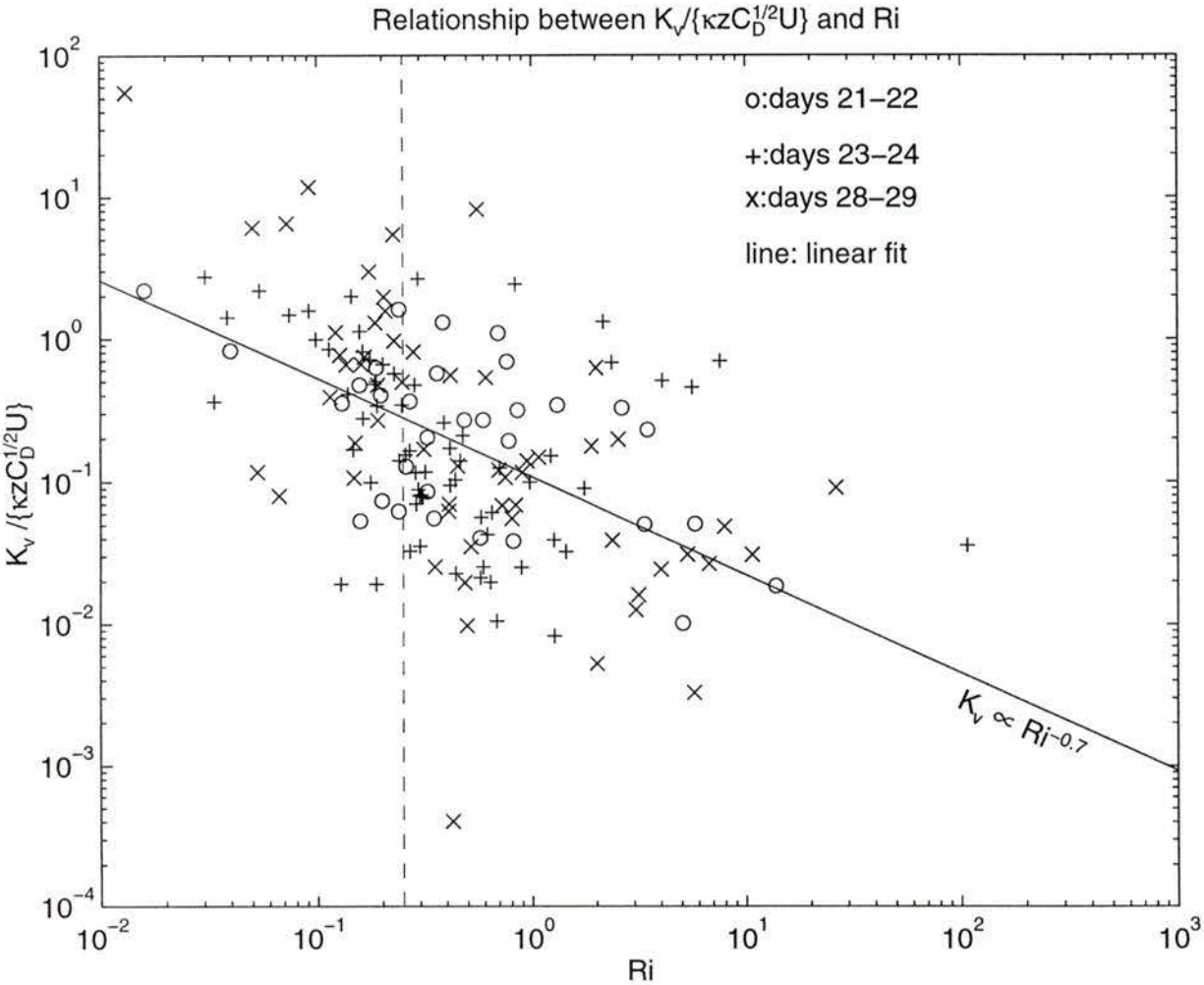

Figure 8.50: The non-dimensional eddy diffusivity and the Richardson numbers for three days of available data. Dashed line is Ri =1/4. The solid line denotes $K_v/\kappa z C_D^{1/2} U \propto Ri^{-0.7}$, obtained by 1st order least square fit.

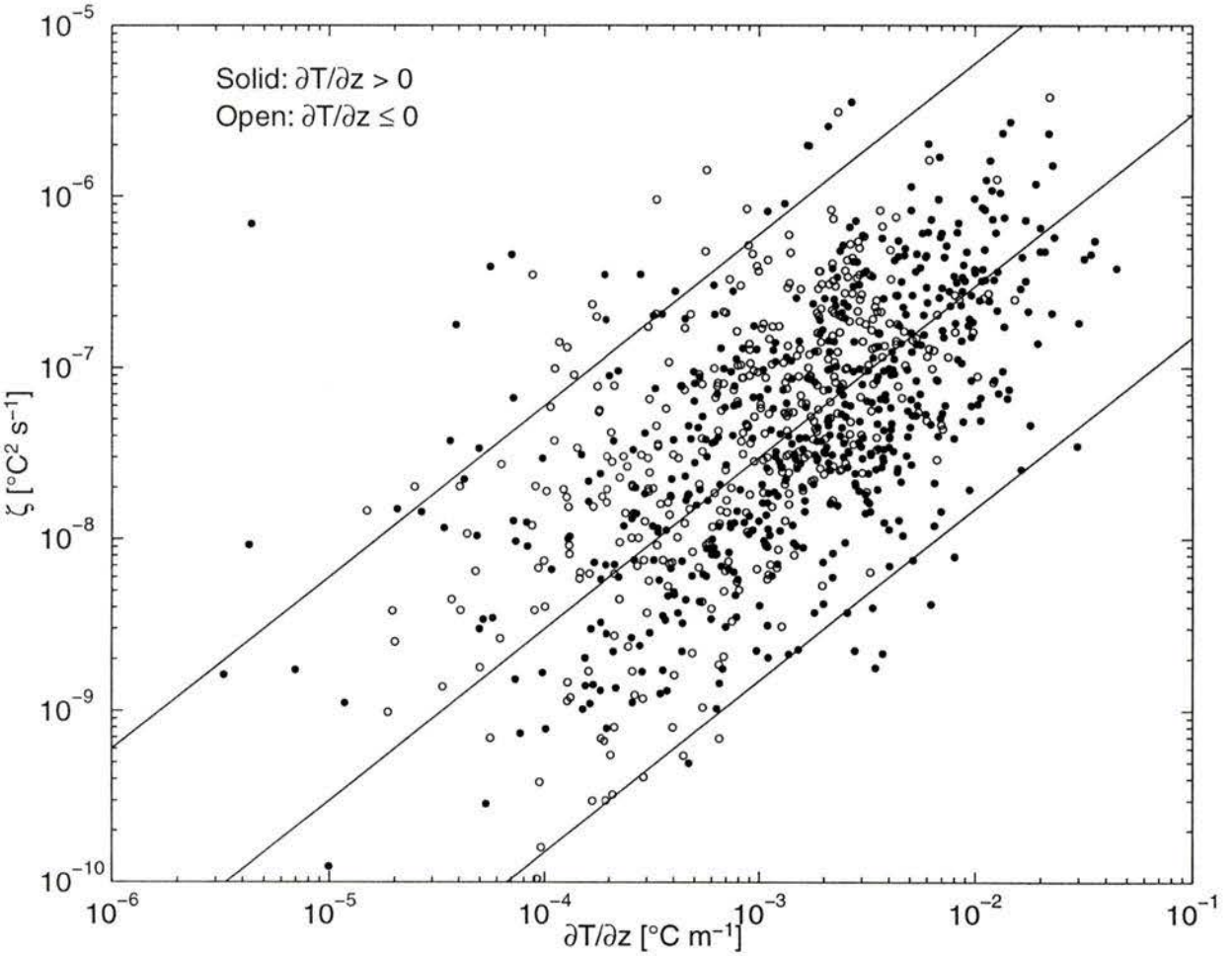

Figure 8.51: Comparison of mean vertical temperature gradient against temperature spectral level, ζ. Solid (open) symbols denote positive (negative) mean gradients. The central line denotes the average of the ratio of mean gradient to temperature spectral level. The upper (lower) line is a factor of 20 times larger (smaller) than the average.

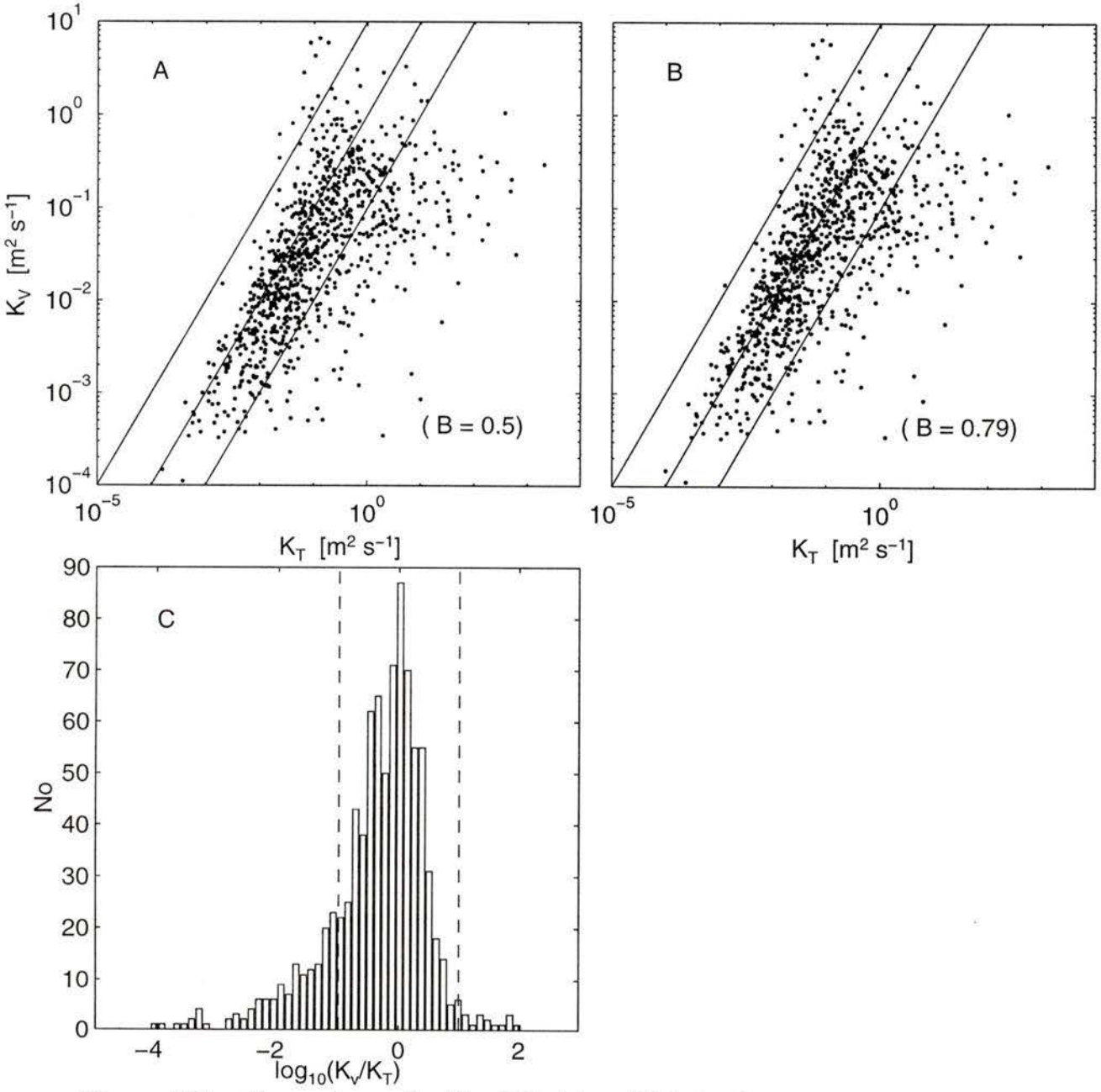

Figure 8.52: Comparison of eddy diffusivity (K_T) for heat against the eddy diffusivity for density (K_v) and the eddy viscosity (A_v). A: K_T against K_v using $K_T = 2\chi\left(\frac{\partial T}{\partial z}\right)^{-2}$, where $\chi = \zeta/B$ and $B = 0.5$, and $K_v = 0.2\epsilon$. The solid line represents equality. B: K_T using $B = 0.79$ against K_v. The solid line represents equality. C: Histogram of the ratio of K_v to K_T of B panel. Dashed lines denote a range of one decade of unity.

mentioned in section 8.4, $\Gamma = 0.2$ is used for estimating K_v and this estimate of K_v is actually its upper limit. We make two choices for the "universal" constants – (*i*) $B = 0.5$ which is the most frequent choice and (*ii*) $B = 0.79$ which was used by Edson *et al.* (1991) for the estimates of fluxes of temperature and humidity in an atmospheric boundary layer over the ocean. For the case of $B = 0.5$, the eddy diffusivity for heat (K_T) frequently exceeds that for density (K_v). However, for the choice of $B = 0.79$, the most probable values of K_T equal K_v and and 81% of the data collapse into a one decade range of equality (Figure 8.52B, C). This approximate equality of K_T and K_v spans 3.5 decades. However, the ensemble of the values of $\log_{10}(K_v/K_T)$, which has a mean of -0.35, fails to pass a significance test for the equality with 0 at 5% significance level (Jenkins and Watts 1968). The Kolmogoroff-Smirnov test (Press *et al.* 1989) also fails to accept that the distribution of K_v/K_T is log-normal. However, the median of K_v/K_T is 0.63 and close to unity while the linear mean of K_v/K_T is 1.75.

The three days of the ADCP shear were used to produce 166 estimates of the eddy viscosity from (2.51) (Figure 8.53). These estimates span 3 decades and compare well against the eddy diffusivity for heat (K_T). Seventy-four percent of the data fall into a one-decade range of $A_v = K_T$ and 96% are within a two-decade range. The statistics also show that the most probable values of K_T is approximately equal to A_v. The logarithmic mean is 1.49 and median is 1.20, however, the linear mean is 120 due to a few extremely large values. Only using data within a two-decade range of unity, the logarithmic mean and the median are 1.16 and 1.14, respectively, and both are close to unity while the linear mean is 5.5.

8.6 Discussion

The eddy viscosity (A_v) is usually assumed to be a constant in numerical models and a constant A_v implies that the eddy diffusivity for density is inversely proportional

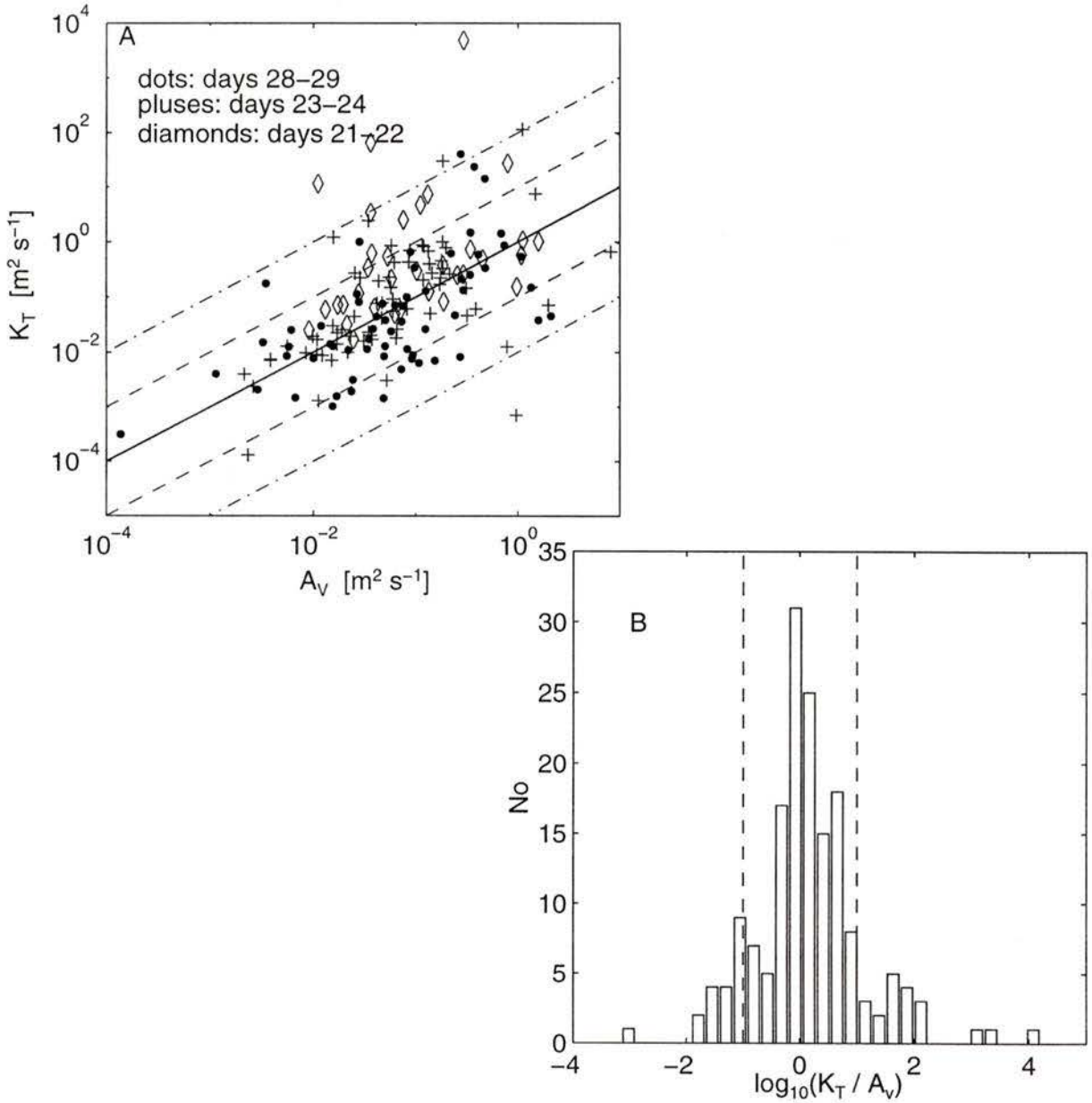

Figure 8.53: A: Comparison of eddy diffusivity (K_T) for heat against the eddy viscosity (A_v). K_T of (2.42) using $B = 0.5$ against A_v of (2.51). The solid line denotes equality. The dashed lines represent a one decade range from equality and the dash-dotted lines represent a two-decade range. B: Histogram of $\log_{10}(K_T/A_v)$. Dashed lines denote a one decade range of unity.

to the Richardson number, i.e. $K_v \propto R_i^{-1}$. We find that the eddy diffusivity for density, K_v, decreases with increasing Richardson number (Figure 8.50) but a little less steeply ($K_v \propto Ri^{-2/3}$). However, the eddy viscosity, A_v, varies over a 3 decade span (Figure 8.53) and is far from a constant. Thus, numerical models must contain an eddy viscosity that varies over a wide range.

From Figure 8.52B, C and Figure 8.53, we can argue that $K_v = K_T$ and $A_v = K_T$ and these two relationship makes $K_v = A_v$, which indicates that eddy motions contribute approximately equally to the vertical fluxes of momentum and density. From (2.12) and the definitions of the eddy viscosity, we can obtain,

$$\frac{0.2\epsilon}{N^2} \geq K_v = A_v = \frac{\epsilon}{\left(\frac{\partial U}{\partial z}\right)^2} \tag{8.54}$$

and, hence,

$$Ri \leq \frac{1}{5}. \tag{8.55}$$

Thus, the turbulence tends to maintain the Richardson number near and below its critical value.

Chapter 9

Conclusion

A microstructure instrument (TAMI) was moored in Cordova Channel for 10 days joining a collaborative experiment, and had successfully measured the microstructure of temperature and velocity. TAMI and other instruments involved also measured non-turbulence data, including the ambient current, mean temperature, mean salinity, CTD profiles and wind speed. Here I will summarize the results which I presented in this thesis.

In Chapter 6:

1. The individual velocity and temperature spectra had -5/3 slopes in the inertial-subrange regardless of whether the effect of stratification was strong or weak. The range of the buoyancy Reynolds number was from 200 to 10^7. The slope of the averaged spectra for the velocity and temperature is not significantly different from -5/3$\pm$0.01 in the inertial-subrange and this uncertainty of 0.01 is due to the accuracy of the calibration of the gain of the differentiators.

2. The range of the inertial-subrange for these spectra is nearly two decades, extending from 3×10^{-4} to $0.02k_1/k_s$.

3. The universal functions (F_{22} and F_{33}) for the spectra of the two cross-stream velocity fluctuations (v, w) are found to be statistically identical.

In Chapter 7:

1. The dissipation in the channel at 15m above the bottom ranged from 10^{-8} to 10^{-4} W kg^{-1}.

2. The pattern of the rate of dissipation and the current repeated every lunar day. The pattern during the first deployment consisted of two ebbs and two floods while the pattern during the second deployment consisted of two ebbs and a single flood.

3. The dissipation within each flood and ebb was not proportional to the current speed cubed (U^3) or U^3_{max} - the maximum speed for each ebb/flood. The turbulence, in the center of Cordova Channel and at 15 m above the bottom, was not generated by the local bottom stress presumably because the sensors were usually out of the log layer.

4. Events of large dissipation coincide with events of intense 2-D horizontal eddy KE. This indicates that the turbulence may have been generated by the 2-D horizontal eddies, which very likely emanated from Cordova Spit and the north end of James Island.

In Chapter 8:

1. The dissipation estimated with TAMI is equal to the estimates obtained with the acoustic scintillation system of IOS within better than a factor of 1.6.

2. The production of turbulent kinetic energy ($P = -\overline{uw}\frac{\partial U}{\partial z} - \overline{vw}\frac{\partial V}{\partial z}$) estimated from the ADCP data taken between 13.6 and 16.6m above the bottom and 90 m south of TAMI was balanced within a factor of 2 by the rate of dissipation obtained with TAMI.

3. The decay time for the 2-D eddy KE is estimated to be a little longer than one hour, a time in which an eddy travels 3 km with a typical current speed of 0.6 ms^{-1}.

4. Three different methods of estimating the average of the ratio of the mean tidal KE to the time integrated rate of dissipation give 53, 77 and 84% of the tidal

KE dissipated locally.

5. The data for three days shows that $K_v \propto Ri^{-2/3}$, where $K_v = 0.2\epsilon N^{-2}$. The eddy diffusivity does not have a clear tidal signal.

6. The temperature spectral level, ζ, is related to the magnitude of the mean temperature vertical gradient, with $|\frac{\partial T}{\partial z}/20| \leq 3 \times 10^{-4}\zeta \leq 20|\frac{\partial T}{\partial z}|$.

7. Eighty-one percent of eddy diffusivity for density, K_v, and eddy diffusivity for heat, K_T, estimated with (2.42) and using $B = 0.79$, are within a range of one decade of $K_v = K_T$ and they span 3.5 decades.

8. The eddy diffusivity for heat (K_T) are approximately equal to the eddy viscosity, A_v, estimated with shear measured by the ADCP. Individual 20 minute estimates fluctuate but seventy-four percent of the estimates are within one decade of equality, over a span of more than 4 decades.

Appendix A

Corrections for current speed and salinity

A.1 Current speed

There were at least three instruments measuring current during the experiment. The measurements from TAMI are compared against the data from the other instruments (CMI and ADCP) to examine their consistency. Only the record from the rotor on the lower mast of TAMI is used because the rotor on the top mast got jammed by jellyfish.

The measured current direction agrees well among the three instruments (Figure A.54). However, the speed reported by the rotor on TAMI is consistently less than measured with the CMI and the ADCP. The ADCP record shown is the average of the reading at 14.5 and 15.6m above the bottom while the CMI data were taken at 20 m above the bottom. The ADCP was closer to TAMI than CMI (90m south verses 300m west). Although the CMI and the ADCP were ~400m apart, the speeds measured by the two instruments agree closely. The ratio of the speed from the ADCP to the speed from TAMI was approximately 1.2. Minute amounts of gelatinous material found in the rotor bearings after recovery may have been responsible for slowing the rotor. To correct this difference, we have multiplied the current speed reported by TAMI by 1.2. The corrected speed agrees with those from the ADCP and the CMI (Figure A.55).

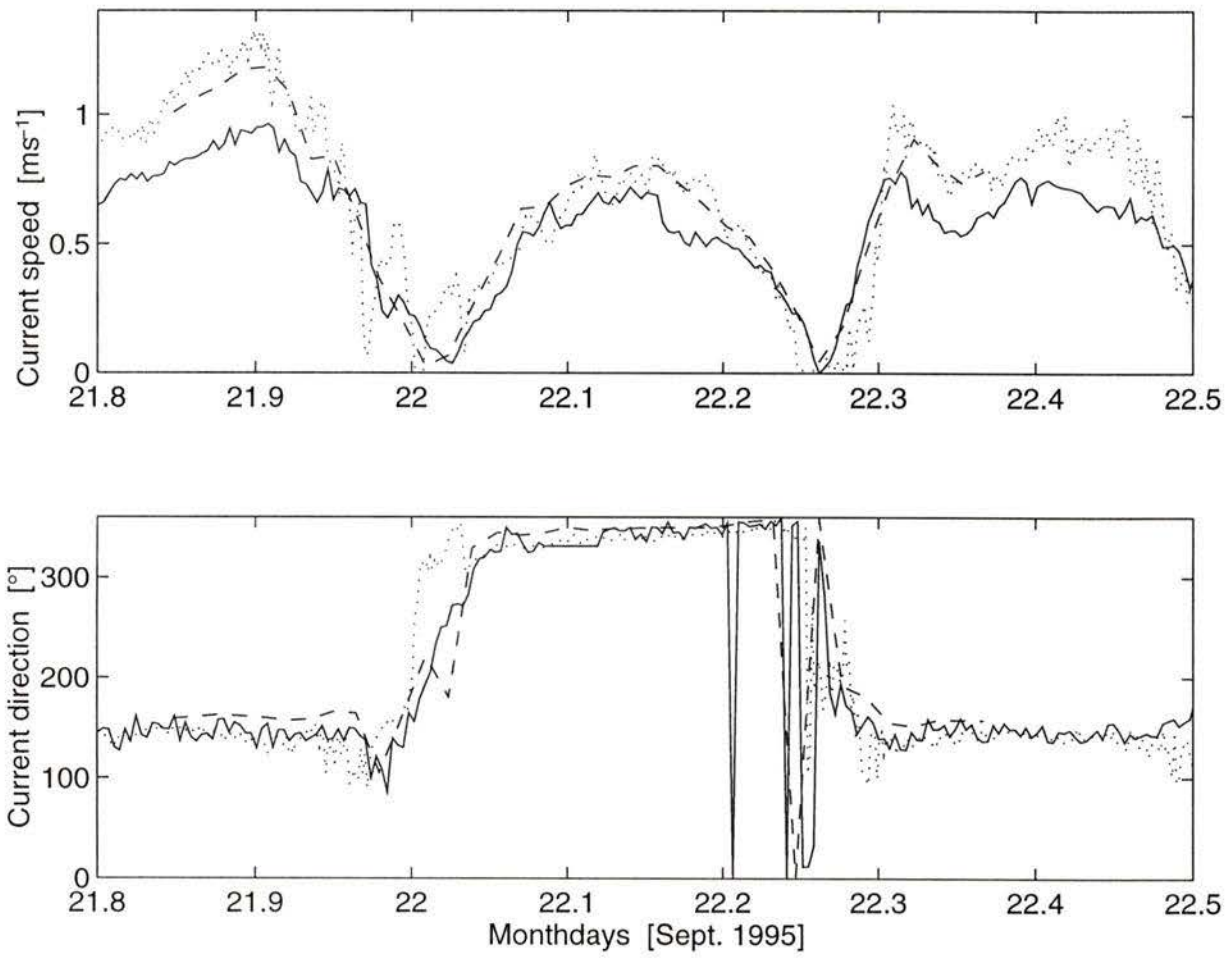

Figure A.54: Comparison of the currents reported from TAMI (solid line), the CMI (dots) and the ADCP (dashed line) on a typical day. Upper panel: The current speed records taken by the three instruments. Lower panel: The current direction records taken by the three instruments.

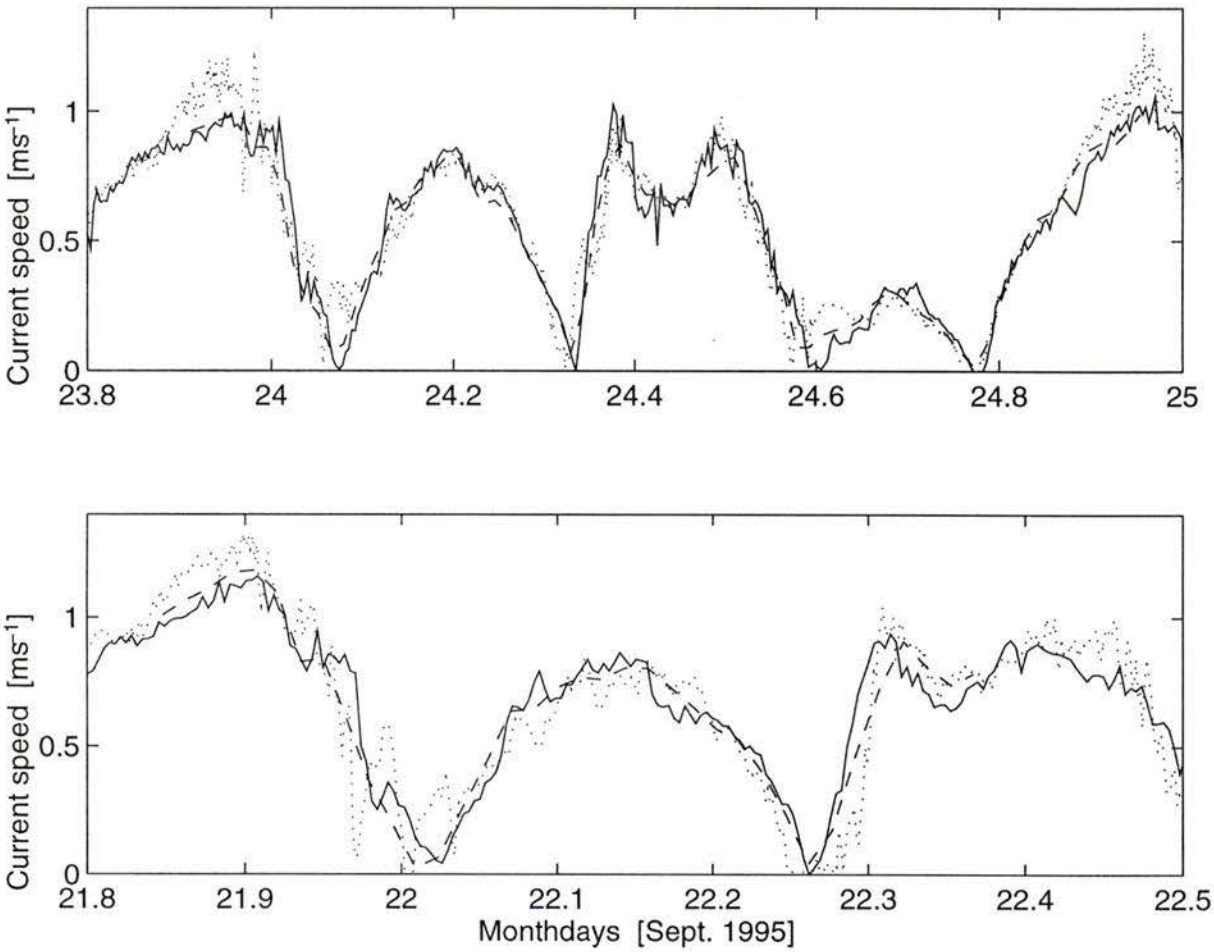

Figure A.55: Comparison of the current speed record (solid line) taken by TAMI after multiplication by 1.2 against the records taken by the CMI (dots) and the ADCP (dashed line) on two typical days.

A.2 Salinity

Using the records from the top and bottom Sea-Bird sensors which are 3m apart, the Brunt-Väisälä frequency was estimated by

$$N^2 = -g\left(-\alpha\frac{\partial T}{\partial z} + \beta\frac{\partial S}{\partial z}\right) \tag{A.56}$$

where $\alpha = -\frac{1}{\rho}\frac{\partial \rho}{\partial T}$, $\beta = \frac{1}{\rho}\frac{\partial \rho}{\partial S}$, T is temperature and S is salinity.

The pre- and post-cruise calibrations indicated that the accuracy of the thermometers is better than 0.002°C. Plankton can not affect the measured mean temperature. Thus, the effect of the accuracy of the thermometers on the accuracy of the estimate of N^2 is unimportant.

The most important point concerning the estimation of N^2 is the contamination of the conductivity cells by plankton. The contamination was caused by particles entering the cell, jellyfish blocking the cell and the membrane of plankton covering the wall of the cell. The effects reduce measured conductivity and hence they reduce the estimated salinity. The assumption for correcting the salinity is that the long-term average of stratification was vertically uniform between the upper and lower cells. Before correcting the salinity, the averages of the gradients of $\partial S_{t-b}/\partial z$, $\partial S_{t-m}/\partial z$ and $\partial S_{m-b}/\partial z$ (where "t" denotes the top cells, "m" denotes the middle cell and "b" denotes the bottom cell) were 0.0017, -0.0006 and 0.0040 psu/m, respectively, during the most of the first deployment. The mean of $\partial S_{t-m}/\partial z$ ($\partial S_{m-b}/\partial z$) was -0.0006 psu/m (0.0040psu/m) and consistently smaller (larger) than $\partial S_{t-b}/\partial z$ (0.0017 pus/m). Adding 0.0035 psu to the reading of the middle cell made all average gradients equal to 0.0017psu/m. This amount of 0.0035 psu is about the same as the magnitude of the difference between the pre- and post-cruise calibrations of the cells. In addition, the records of T and S from TAMI is consistent with the measurements of T and S from CTD profiler.

Appendix B

Shear spectrum correction

B.1 Shear probe resolution

Because of the finite size of the shear probe it is not always possible to resolve a shear variance, contributing to the dissipation of kinetic energy. The wavenumber contributing to the variance generally ranges from 1 to 100cpm (Gregg 1987). The spectrum at large wavenumbers is attenuated by the limited wavenumber response of the shear probe. To correct the spectrum of the measured shear, Ninnis (1984) developed the transfer function

$$H^2(k) = 1 - 0.164\frac{k}{k_o} - 4.537\left(\frac{k}{k_o}\right)^2 + 5.503\left(\frac{k}{k_o}\right)^3 - 1.804\left(\frac{k}{k_o}\right)^4 \qquad \text{(B.57)}$$

where $k_o = 122.4$cpm is first zero response wavenumber of our probes..

B.2 Sensitivity of shear probes

The shear probes used in Cordova Channel were calibrated before and after the experiment. The calibration temperature was higher than 20°C (Table B.9). Over 3 and a half months or longer, the sensitivities drifted only a few percentage points and the maximum drift is only 10 percent for L13 (Table B.9). However, the sensitivities of

S/N	Signal	date	T °C	S	date	T °C	S
L11	$\frac{\partial w_1}{\partial x}$	27/07/94	20.4	0.191	07/10/94	20.6	0.194
L14	$\frac{\partial w_2}{\partial x}$	25/07/94	21.1	0.175	07/10/94	21.5	0.169
L13	$\frac{\partial v_1}{\partial x}$	21/07/94	28.1	0.254	07/10/94	21.5	0.227
1-dot	$\frac{\partial v_2}{\partial x}$	28/07/95	22.8	0.136	07/10/94	20.4	0.130

Table B.9: Sensitivities of the shear probes calibrated at 20°C

S/N	Signal	date	T °C	S	date	T °C	S	T °C	S
L11	$\frac{\partial w_1}{\partial x}$	07/10/94	20.6	0.194	22/12/94	9.4	0.178	11.5	0.155
L14	$\frac{\partial w_2}{\partial x}$	07/10/94	21.5	0.169	20/12/94	9.4	0.129	11.5	0.136
L13	$\frac{\partial v_1}{\partial x}$	07/10/94	21.5	0.227	20/12/94	9.4	0.205	11.5	0.209
1-dot	$\frac{\partial v_2}{\partial x}$	07/10/94	20.4	0.130	28/12/94	10.0	0.125	11.5	0.126

Table B.10: Sensitivities of the shear probe calibration and interpolation. [Note that L11's sensitivity is deduced by matching to L14's]

the shear probe is known to be dependent on temperature. The sensitivity decreases with decreasing temperature and is 5% to 25% smaller at 9°C (Table B.10), compared to 20°C.

The temperature of the water during the experiment was around 11.5°C (Figure 4.14, 4.15). The sensitivities used for the computation of dissipation are the values interpolated to 11.5° using the warm calibration of October and the cold calibration of December. The dissipations obtained with L14, L13 and "1-dot" are statistically identical (Figure B.56 B, E and F). However, the dissipation obtained with L11 is 15 - 43% larger than the other estimates. Therefore, the sensitivity of L11 was decreased by 13% from its interpolated value to make the dissipation estimate with this probe consistent with the other estimates (Figure B.56 A, C and D).

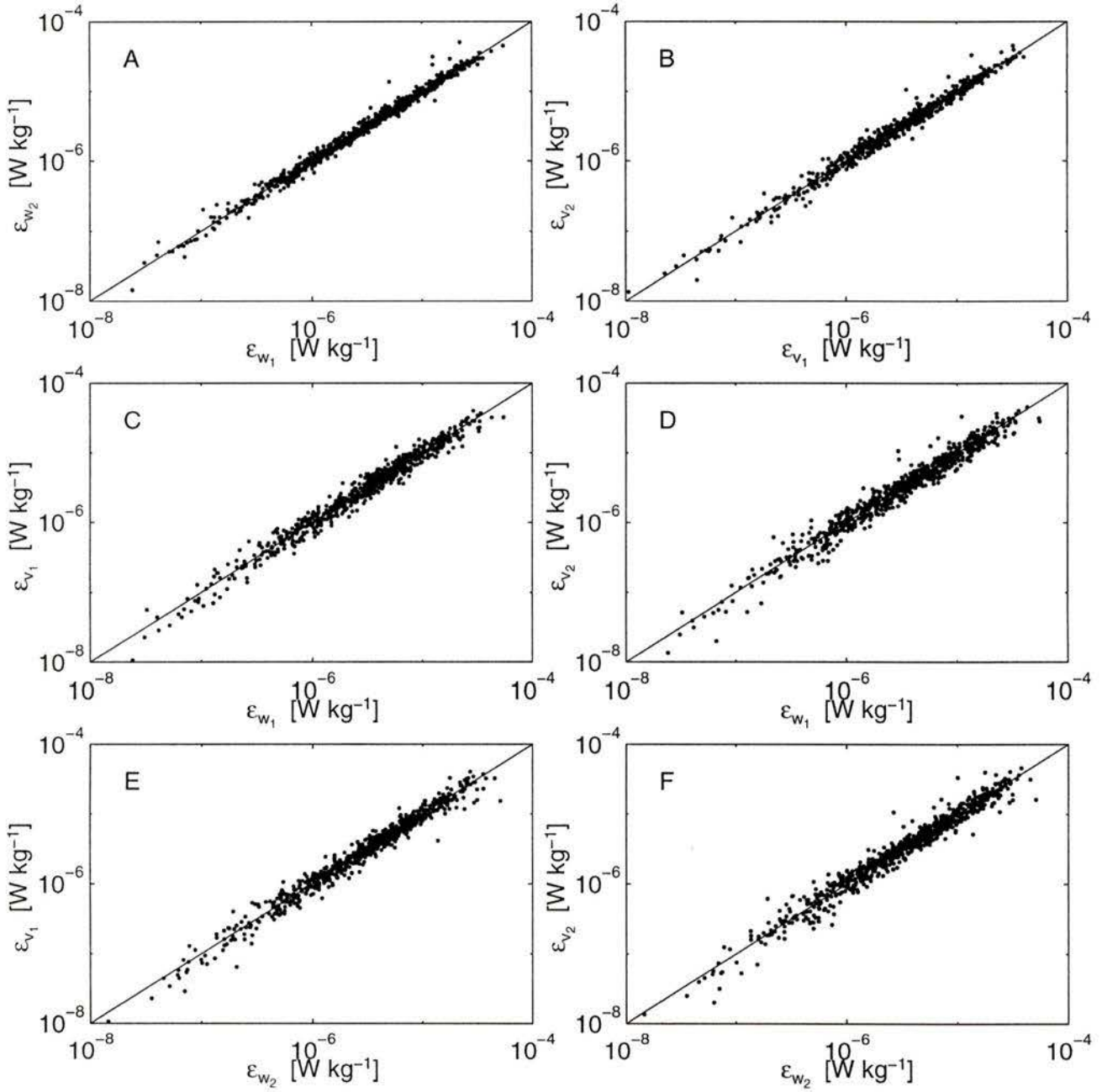

Figure B.56: Comparison of dissipation obtained with various probe pairs after the interpolation of sensitivities to 11.5°C. A: ϵ_{w_1} against ϵ_{w_2}. B: ϵ_{v_1} against ϵ_{v_2}. C: ϵ_{w_1} against ϵ_{v_1}. D: ϵ_{w_1} against ϵ_{v_2}. E: ϵ_{w_2} against ϵ_{v_1}. F: ϵ_{w_2} against ϵ_{v_2}.

Appendix C

Estimates of dissipation

The rate of the dissipation of turbulent kinetic energy is usually estimated with the shear variance using equation (2.18) in oceanic measurements (Oakey 1982; Gregg 1987). The inertial-subrange technique is another method used to estimate dissipations (Fairwey 1990; Gross and Nowell 1985; Grant *et al.* 1984; McPhee 1994). Within the inertial-subrange, a velocity spectrum has a well-defined -5/3 slope according to (2.33).

The velocity spectrum used for estimating dissipation is derived from the measured shear spectrum. The dissipation is estimated by, (*i*) calculating dissipation at each spectral point within a range not contaminated by body motion using

$$\epsilon = \left(\frac{3\phi_{jj}(k_1) k_1^{5/3}}{4K} \right)^{3/2}, \tag{C.58}$$

where $j = 2, 3$ and no summation implied, and (*ii*) averaging all such dissipation estimate to obtain a single estimate of the rate of dissipation from each velocity spectrum.

Bibliography

[1] Antonia, R.A., and R.E. Luxtion, 1971: Energy balance in a turbulent boundary layer on a rough wall. *Phys. Fluids*, **14**, 1027-1029.

[2] Bowden, K.F. and S. R. Ferguson, 1980: Variations with height of the turbulence in a tidally-induced bottom boundary layer. *Marine Turbulence*, Ed. by Jacques C.J. Nihoul, pp 259-286.

[3] Crawford, W. R., and R. K. Dewey, 1990: Confident limits for friction velocity determined from turbulence profiles in coastal waters. *J. Phys. Oceanogr.*, **7**, 50-57.

[4] Corrsin, S, 1951: On the spectrum of isotropic temperature fluctuations in isotropic turbulence. *J. Appl. Phys.*, **34**, 515-530.

[5] Di Iorio, Daniela, 1994: Measurements of turbulence parameters and observations of multipath arrivals in two contrasting coastal environment using acoustic scintillation analysis. Ph. D. thesis, Dept. of Phys. & Astron, University of Victoria, pp 176

[6] Di Iorio, Daniela, 1995: Separation of velocity and sound speed variability in the effective index fluctuation using reciprocal acoustic transmission – A summary report for the Cordova Channel 1994 acoustic experiment. Institute of Ocean Sciences, Sidney, B.C., V8L 4B2, Canada.

[7] Dewey, K. R. and W. R. Crawford, 1988: Bottom stress estimates from vertical dissipation rate profiles on the continental shelf. *J. Phys. Oceanogr.*, **18**, 1167-1177.

[8] Dewey, K. R., A.E. Gargett and N.S. Oakey, 1987: A microstructure instrument for profiling oceanic turbulence in coastal bottom boundary layres. *J. Atmo. Oceanic Technol.*, **4**, 288-297.

[9] Dillon, T. M., and Caldwell, D.R., 1980: The Batchelor spectrum and dissipation in the upper ocean. *J. Geophys. Res.*, **85**, 1910-1916.

[10] Edson, J.B., C.W. Fairall, P.G. Mestayer, and S.E. Larsen, 1991: A study of the inertial-dissipation method for computing air-sea fluxes. *J. Geophys. Res.*, **96**, 10,689-10,711.

[11] Efron, B., and G. Gong, 1983: A leisurely look at bootstrap, the Jackknife, and cross-validation. *American Stats.*, **37**, 36-48.

[12] Fairall, C.W., J.B. Edson, S.E. Larsen, and P.G. Mestayer, 1990: Inertial-dissipation air-sea flux measurements: A protoype system using real time spectral computation. *J. Atmo. Oceanic. Techn.*, **7**, 425-453.

[13] Farmer, D., S. F. Clifford, and J. A. Verrall, 1987: Scintillation structure of a turbulence tidal flow. *J. Geophy. Res.*, **92**, 5369-5382.

[14] Fluery, M., and R. G. Lueck, 1994: Direct heat flux estimates using a towed vehicle, *J. Phys. Oceanogr.*, **24**, 801-818.

[15] Foreman, M. G. G., 1978: Manual for tidal currents analysis and prediction. *Pacific Marine Science Report*, **78-6**, Institute of Ocean Science, Sidney, B.C., pp 70.

[16] Foreman, M. G. G., R. A. Walters, R. F. Keller, and A. G. Dolling, 1994: A tidal model for eastern Juan de Fuca Strait and the southern Strait of Georgia. *J. Geophy. Res.* **100**, 721-740.

[17] Gargett, A. E., T. R. Osborn, and P.W. Nasmyth, 1984: Local isotropy and decay of turbulence in a stratified fluid. *J. Fluid Mech.*, **44**, 231-80.

[18] Gargett, A. E., 1985: Evolution of scalar spectra with the decay of turbulence in a stratified fluid. *J. Fluid Mech.*, **159**, 379-407.

[19] Gargett, A. E., and G. Holloway, 1984: Dissipation and diffusivity by internal wave breaking. *J. Mar. Res.*, **42**, 15-27.

[20] Gibson, C.H., and W.H. Schwaz, 1963: The universal equilibrium spectra of turbulent velocity and scalar fields. *J. Fluid Mech.*, **16**, 365-384.

[21] Gibson, C.H., G.R. Stegen, and R.B. Williams, 1970: Statistics of the fine structure of turbulent velocity and temperature-fields measured at high Reynold number. *J. Fluid Mech.*, **41**, 153-167.

[22] Gogin, G., 1972: *The Analysis of Tides.* University of Toronto Press, Toronto, Ontario, pp 264.

[23] Grant, H. L., R. W. Stewart, and A. Moilliet, 1962: Turbulence spectra from a tidal channel. *J. Fluid Mech.*, **12**, 241-263

[24] Grant, H. L., B. A. Hughes, W.M. Vogel, and A. Moilliet, 1968: The spectrum of temperature fluctuation in turbulent flow. *J. Fluid Mech.*, **34**, 423-442.

[25] Gregg, M. C., 1987: Diapycnal mixing in the thermocline: A review. *J. Geophy. Res.*, **92**, 5249-5286.

[26] Gregg, M. C., T.B. Sanford, 1988: The dependence of turbulent dissipation on stratification in a diffusively stable thermocline. *J. Geophy Res.*, **15**, 12,381-12,3392.

[27] Gross, T. F., A. R. M. Nowell, 1985: Spectral scaling in a tidal boundary layer. *J. Phys. Oceanogr.*, **15**, 496-508.

[28] Hinze, O.J., 1975: *Turbulence: An Introduction to its Mechanism and Theory.* McGraw-Hill, New York, 2nd Ed. pp 790.

[29] Itsweire, E.C., K.N. Heilland, and C.W. van Atta, 1986: The evolution of grid-generated turbulence in a stably stratified fluid. *J. Fluid Mech.*, **162**, 299-338.

[30] Jenkins, G. M., D. G. Watts, 1968: *Spectral Analysis and its Application.* Holden-Day. pp 525.

[31] Johnson, G.C., T.B. Sanford, and M.O. Baringer, 1994: Stress in the Mediterranean outflow plume: Part I. Velocity and water property measurements. *J. Phys. Oceanogr.*, **24**, 2072-2083.

[32] Kolomogoroff, A.N., 1941: The local structure of turbulence in an incompressible viscous fluid for very large Reynolds number. *C. R. Acad. Sci. USSR*, **30**, 301-305.

[33] Kundu, P. K. 1990: *Fluid Mechanics.* Academic Press, Inc., San Diego, California, pp 638.

[34] Kunze, E., and T.B. Sanford, 1984: Observations of near-inertial waves in a front. *J. Phys. Oceanogr.*, **14**, 566-581.

[35] Lu, Y., and R. G. Lueck, 1996a: Flow measurement in a tidal channel using an acoustic Doppler current profile. Submitted to *Continental Shelf Research.*

[36] Lu, Y., and R. G. Lueck, 1996b: Measurement of Reynold stress and turbulent production in a tidal channel. In preparation.

[37] Lueck, R.G., and Y. Lu, 1996: The logarithmic layer in a tidal channel. Submitted to *Continental Shelf Research.*

[38] Lueck, R.G., 1987: Microstructure measurements in a thermohaline staircase. *Deep Sea Res.*, **34**, 1677-1688.

[39] Lueck, R.G., D. Huang, D. Newman and J. Box, 1996: Turbulence measurement with a moored instrument. *J. Atmo. Oceanic Techn.*, **14**, 143-161.

[40] McPhee, M.G., 1992: Turbulence heat flux in the upper ocean sea ice. *J. Geophys. Res.*, **97**, 5365-5379.

[41] McPhee, 1994: On the turbulent mixing length in the oceanic boundary layer. *J. Phys. Oceanogr.*, **24**, 2014-2031.

[42] Maddock, L. and R.D. Pingree, 1978: Numerical simulation of the Portland tidal eddies. *Estuarine Coastal Mar. Sci.*, **6**, 353-363.

[43] Miles, J.W., 1961: On the stability of heterogeneous shear flow. *J. Fluid Mech.*, **10**, 495-508.

[44] Miles, J.W., 1986: Richardson's criterion for the stability of the stratified flow. *J. Fluid Mech.*, **29**, 3470-3471.

[45] Monin, A.S., and A. M. Yaglom, 1971: *Statistical Fluid Mechanics I.* The MIT Press, Boston, Massachusetts, pp 769.

[46] Monin, A.S., and A. M. Yaglom, 1975: *Statistical Fluid Mechanics II.* The MIT Press, Boston, Massachusetts, pp 874.

[47] Moum J.N., and R.G. Lueck, 1985: Causes and implications of noise in oceanic dissipation measurements. *Deep-Sea Res.*, **32**, 379-390.

[48] Nasmyth, P.W., 1970: Oceanic turbulence. Ph.D. thesis. Institute of Oceanography, University of British Columbia. Vancouver, B.C. pp 69.

[49] Ninnis R., 1984: The spatial transfer function of the airfoil shear probe. Ph.D. thesis. Department of Oceanography, University of British Columbia, Vancouver, B.C. pp 109.

[50] Oakey, N. S., 1982: Determination of the rate of dissipation of turbulent energy from simultaneous temperature and velocity shear microstructure measurements. *J. Phys. Oceanogr.*, **12**, 256-271.

[51] Oboukov, A. M., 1949: Structure of the temperature field in a turbulent flow. *Izv. Akad. Nauk. SSSR Ser. Geogr. i Geofiz.*, **13**, 58-69.

[52] Osborn, T. R., 1980: Estimates of the local rate of vertical diffusion from dissipation measurements. *J. Phys. Oceanogr.*, **10**, 83-89.

[53] Osborn, T. R., C.S. Cox, 1972: Oceanic fine structure. *Geophys. Fluid Dyn.*, **3**, 321-345.

[54] Osborn, T. R., and W. R. Crawford, 1980: An foil probe for measuring turbulent velocity fluctuations in water. In *Air-Sea Interaction: Instrumentation and Methods*, Ed. F. Dobson, L. Hasse, and R. Davis, 369-386.

[55] Osborn, T. and R. G. Lueck, 1985a: Turbulence measurements from a towed body. *J. Amto. Oceanic. Techn.*, **2**, 517-527.

[56] Osborn, T. and R. G. Lueck, 1985b: Turbulence measurements from a submarine. *J. Phys. Oceanogr.*, **15**, 1502-1520.

[57] Peters, H., 1995: Observation of stratified turbulent mixing in an estuary. Neap-to-spring variations during high river run-off. Submitted to *Estuarine, Coastal and Shelf Science.*

[58] Peters, H., M.C. Gregg, and T.B. Sanford, 1995: Detail and scaling of turbulent overturning in the Pacific Equatorial Undercurrent, *J. Geophy. Res.*, **100**, 18,333-18,348.

[59] Pingree, R.D., 1978: The formation the shambles and other banks by tidal stirring of the seas. *J. Mar. Bio. Assoc. UK*, **58**, 211-226.

[60] Pond, S. and G. L. Pickard, 1990: *Introductory Dynamical Oceanography.* Pergamon Press, New York, pp 329.

[61] Press, W.H., B. P. Flannery, S. A. Teukolsky, and W. T. Vettering, 1989: *Numerical recipes – The art of scientific computing (Fortran version).* Cambridge University Press, Cambridge, UK, pp 702.

[62] Robinson, I.S, 1983: Tidal induced residual flows. *Physical Oceanography of Coastal and Shelf Seas*, Ed. B. Johns, **Chapter 7.**

[63] Schlichting, H., 1955: *Boundary layer theory.* Translated by J. Kestin. Pregamon Press, London, UK. pp 535.

[64] Smith, S.D., 1988: Coefficients for sea surface wind stress, heat flux, and wind profiles as a function of wind speed and temperature. *J. Geophys. Res.*, **93**, 15,467 - 15,472.

[65] Stewart, R.W., 1959: The problem of diffusion in a stratified fluid. *Advances in Geophysics*, **6**, Academic Press, 303-311.

[66] Tennekes, H., and J. L. Lumley, 1972: *A First Course in Turbulence.* The MIT Press, Boston, Massachusetts, pp 300.

[67] Tennekes, H., 1975: The logarithmic wind profile. *J. Atmos. Sci.*. **34**, 234-238.

[68] Thomson, R.E., 1981: *Oceanography of British Columbia Coast.* Department of Fisheries and Oceans, Ottowa, pp 291.

[69] van Atta, C.W., 1971: Influence of fluctuation in local dissipation rates on turbulent scalar characteristics in the inertial subrange. *Phys. Fluids*, **14**, 1803-1804.

[70] van Atta, C.W., 1971: Erratum: Influence of fluctuation in local dissipation rates on turbulent scalar characteristics in the inertial subrange. *Phys. Fluids*, **16**, 574.

VITA

Surname: Huang Given Name: Dai Yan

Educational Institutes Attended:

Shandong College of Oceanography	1982 - 1986
Ocean University of Qingdao	1986 - 1989
University of Victoria	1993 - 1996

Degrees Awarded:

B.Sc.	Shandong College of Oceanography	1986
M.Sc.	Ocean University of Qingdao	1989

Honours and Awards:

Graduate Teaching Fellowship, University of Victoria	1993 - 1996

Publications:

R. Lueck, D. Huang, D. Neman and J. Box, 1997: Turbulence Measurement with a Moored Instrument. *Journal of Atmospheric and Oceanic Technology*, **Vol. 14**, 143-161.

PARTIAL COPYRIGHT LICENSE

I hereby grant the right to lend my thesis to users of the University of Victoria Library, and to make single copies only for such users in response to a request from the Library of any other university, or similar institution, on its behalf or for one of its users. I further agree that permission for extensive copying of this thesis for scholarly purposes may be granted by me or a member of the University designated by me. It is understood that copying or publication of this thesis for financial gain shall not be allowed without my permission.

Title of Thesis: TURBULENT MIXING IN A TIDAL CHANNEL.

Auth[redacted]

Daiyan Huang

December 20, 1996